7-10-2012

Pattern Formation in Certain Classical and Quantum Systems

Patrick Greenleaf Hart Johnson
Washington University in St. Louis

WASHINGTON UNIVERSITY IN ST LOUIS

Department of Physics

Dissertation Examination Committee:
Zohar Nussinov, Chair
Joshua Maurer
Michael Ogilvie
Jacob Schaefer
Alexander Seidel
Yan Mei Wang

Pattern Formation in Certain Classical and Quantum Systems

by

Patrick Greenleaf Hart Johnson

A dissertation presented to the
Graduate School of Arts and Sciences
of Washington University in
partial fulfillment of the
requirements for the degree
of Doctor of Philosophy

August 2012

Saint Louis, Missouri

Abstract

My research predominantly focuses on micromagnetic simulations of cobalt nanoparticles. These simulations are carried out by using the Object-Oriented MicroMagnetic Framework (OOMMF) distributed by the National Institute of Standards and Technology (NIST). In performing these simulations, observations of skyrmionic states were observed for large enough nanoparticles. Skyrmions are magnetic vortex states which have a core that is antiparallel with the outermost local magnetic moments. These states are being explored as an exciting branch of research that are applicable in many applications including, but not limited to, magnetic storage devices. Most simulations were carried out using a hemispherical geometry because collaborators at the University of Tennessee, Knoxville use laser-induced dewetting to create arrays of hemispheres on the nanometer scale. In conjunction with these simulations, we have performed analytical and numerical calculations of the demagnetizing factor of a hemispherical particle. The demagnetizing factor of a system is a parameter that characterizes shape anisotropy and is useful in calculating the energy of a uniformly magnetized body. Demagnetizing factors have been calculated for different geometries, but never for a hemisphere.

Other projects that my research includes research into rogue waves and a mapping between classical and quantum systems. The rogue wave work deals with analysis of the Nonlinear Schrödinger Equation and developing new forms of rogue wave solutions. This process includes focussing on the time-reversal invariance of the Nonlinear Shrödinger Equation and also generalizes a wave form known as compactons to generate approximate, traveling wave solutions that are like a rogue wave in nature. These can be applied to oceanic, optical, and even economical situations. The mapping that we have generalized here indicates that classical and quantum correlation functions can be calculated from one another simply by allowing time to go to imaginary time, and taking the real part of the expression. This is partially based on previous work in a more specific version of this mapping, but generalizes it to any operator rather than specifically the density operator.

Acknowledgements

I would like to acknowledge all of the people who made this possible. First and foremost, I must thank Zohar Nussinov for being a spectacular advisor. Without his guidance, none of this would be possible. Secondly, I would like to acknowledge Alexander Seidel, Michael Ogilvie, Yan Mei Wang, Jacob Shaefer, and Joshua Maurer for their assistance in my graduate school career. I would like to thank my family, Eric Johnson, Patricia Hart, Ben Johnson, and Dawn Johnson for their love and support. I would also like to thank my friends and colleagues who have helped me along my way.

Contents

List of Figures

List of Tables

111

Chapter 1

Synopsis

This thesis studies and predicts many non-trivial patterns in classical, oceanic, optical, magnetic, and glassy systems. These non-trivial patterns apply to skyrmions in magnetic systems, spatio-temporal correlation functions, rogue waves in various systems. Below, we detail the specific patterns that we analyze in the chapters.

In Chapter 2, background theory is discussed for all other chapters. This background in this chapter starts with the history and derivation of the equations of motion for oceanic and optical rogue waves (Content of Chapter 3). This is followed by the theory behind the micromagnetic framework used to model cobalt hemispheres. This route to skyrmionic textures is the simplest to date. This is coupled with a description of the history of skyrmions in nuclear physics and their appearance in experiments and theory (Chapter 5). Finally, the theory behind "dynamical heterogeneities" (that embody non-trivial spatial and temporal patterns in super-cooled liquids) and jamming is discussed in classical and quantum systems (Content of Chapter 6).

In Chapter 3, by employing a mapping to classical anharmonic oscillators, we explore a class of solutions to the Nonlinear Schrodinger Equation (NLSE) in 1+1 dimensions and, by extension, asymptotically in general dimensions. We discuss a possible way for creating approximate rogue wave-like solutions to the NLSE by truncating exact solutions at their nodes and stitching them with other solutions to the NLSE. The resulting waves are similar to compactons with the notable difference that they are not localized, but extend over all of space. This is a unique approach that differs substantially from most for work to date. Compactons are a soliton on a constant background, but a soliton on periodic background is a much better model to an ocean state. We discuss rogue waves in a ϕ^4 field theory in the context of a discretized Lagrangian and rogue wave behavior is shown to evolve into a steady state. Due to time-reversal invariance of this theory, the steady state found could alternatively evolve into a rogue wave (i.e. to a large wave that seems to appear out of a smooth periodic background).

In Chapter 4, an analytic expression for the spatially dependent demagnetizing factor is calculated. Also presented is a discussion of a method for numerically calculating the spatially averaged demagnetizing factor of a general geometry, which is then applied to the case of a hemisphere. The method that we introduce in this thesis is a more direct method for numerically calculating the spatially averaged demagnetizing factor than existing methods.

In Chapter 5, new methods for magnetic skyrmion generation and customization are suggested. Skyrmionic behavior was numerically observed in minimally cus-

tomized simulations of cobalt spheres, hemispheres, ellipsoids, and hemi-ellipsoids. These skyrmions are observed in a range of diameters from approximately 40 nm to 120 nm simply by applying a field.

In Chapter 6, we report dynamical heterogeneities in quantum systems. To this end, we use a correspondence between viscous classical and quantum many-body systems. We illustrate that, even in the absence of imposed disorder, many continuum systems (and possible lattice counterparts) may exhibit such "quantum dynamical heterogeneities" at zero temperature. These non-trivial spatio-temporal correlations capture these spatially non-uniform dynamics, at a given instant. While the static length scales accompanying this phenomenon do not seem to exhibit a clear divergence in standard correlation functions, the length scale of the dynamical heterogeneities can increase dramatically. We furthermore suggest how a hard core bosonic system can undergo a zero temperature quantum critical metal-to-insulator-type transition with an extremely large effective dynamical exponent $z > 4$ that is consistent with length scales that increase far more slowly than the relaxation time as a putative critical transition is approached. We suggest ways to analyze experimental data in order to adduce such phenomena.

In Chapter 7, a brief summary of the results is presented.

Chapter 2

Background

2.1 Rogue Waves

2.1.1 History of Oceanic Rogue Waves

Rogue waves, also known as freak waves or extreme waves, are large waves that seemingly appear out of nowhere. Roughly speaking, the literature describes a rogue wave to be somewhere at least two and four times the size of surrounding waves and being short temporally. Sailors have told stories of tall "walls of water" that seem to appear out of nowhere, but like most stories from sailors, were mostly assumed to be hyperbole. Similar stories to "holes in the ocean" have also been told, but were equally dismissed for the most part. There are a few stories, though that could not be denied, and led to the scientific community taking rogue waves more seriously. The earliest of these stories was the story of the MS München.

Figure 2.1: Image of the MS München taken in 1978. The location of the lifeboat is indicated with the arrow (15).

The Wreck of the MS München

The MS München was a German freight ship active in the 1970s (29). Around the middle of December in 1978, the MS München vanished without a trace. It was sailing through a large storm in the North Atlantic when it vanished into the sea. Search efforts never found the entire ship, but a lifeboat, complete with some steel pins that held the lifeboat in place were found. The steel pins were clearly bent from their natural position. The lifeboats typically hung approximately 20 meters above the water level, so for the pins to be bent in such a way, a very large force would need to be exerted upon them 20 meters above the water level.

At the time of the sinking of the MS München, the science behind rogue waves was not understood, and for the most part were believed to be tall tales of sailors. As the science was explored more thoroughly, the cause of the force evinced by the bent steel pins was believed to be a rogue wave. However, this is far from conclusive

proof of the existence of oceanic rogue waves.

The Draupner Wave

The first actual measurement of an oceanic rogue wave came on New Year's Day of 1995 off the coast of Norway. An instrument used to measure the surface elevation of the ocean surrounding the Draupner gas platform recorded a large wave that was between two and three times the size of the background waves. This wave has come to be known as the Draupner wave or New Year's wave. The waveform for this wave is shown in Fig (2.2). With the measurement of this wave, the tall tales from the sailors started to be taken more seriously and the search for nonlinear models for the ocean began in earnest.

Derivation of the Nonlinear Model for the Ocean Surface

The evolution of an ocean wave can be modeled using the Nonlinear Schrödinger Equation which is derived from Laplace's Equation with specific boundary conditions and assumption of infinite depth. This was first done by Zakharov (66). Starting with the hydrodynamic potential, $\Phi(\vec{r}, z, t)$, and the shape of the surface of the fluid, $\eta(\vec{r}, t)$, with $r = \sqrt{x^2 + y^2}$, the system of equations takes the form,

$$\vec{\nabla}^2\Phi + \frac{\partial^2\Phi}{\partial z^2} = 0, \tag{2.1}$$

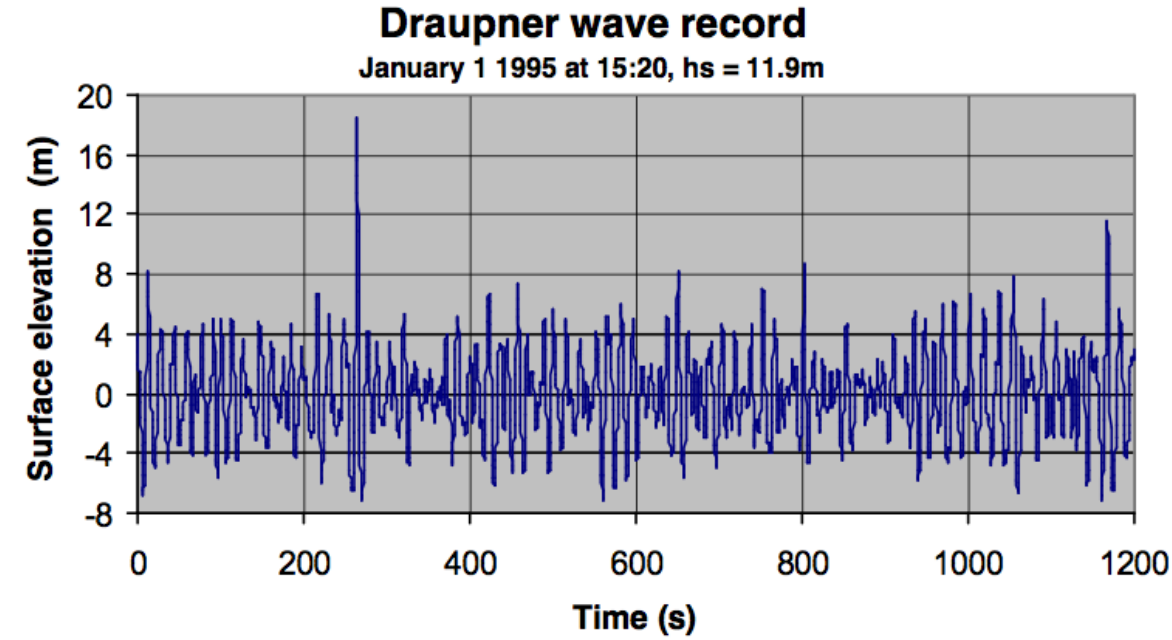

(a)

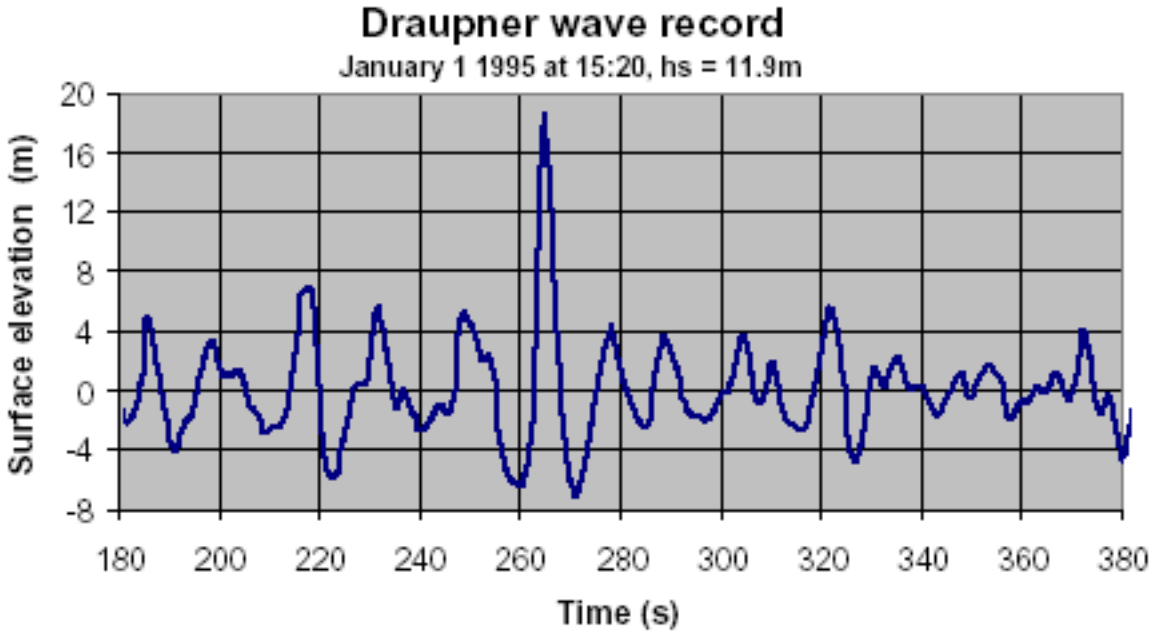

(b)

Figure 2.2: Plot of the elevation of the surface of the ocean near the Draupner platform off the coast of Norway in the North Sea. The typical wave height in this wave train is less than ten meters, as shown in (a). The Draupner wave, though is nearly 20 meters in height (b). This is known as the first recording of an oceanic rogue wave. Image taken from (60).

with boundary conditions,

$$\frac{\partial \eta}{\partial t} = \sqrt{1 + (\vec{\nabla}\eta)^2}\frac{\partial \Phi}{\partial \eta}\bigg|_{z=\eta} = \frac{\partial \Phi}{\partial z} - \vec{\nabla} \cdot \eta \vec{\nabla}\Phi|_{z=\eta}, \tag{2.2}$$

$$\frac{\partial \Phi}{\partial t} + g\eta = -\frac{1}{2}(\vec{\nabla}\Phi)^2|_{z=\eta} - \frac{1}{2}(\frac{\partial \Phi}{\partial z})^2\bigg|_{z=\eta} + \alpha\vec{\nabla} \cdot \frac{\vec{\nabla}\eta}{\sqrt{1 + (\vec{\nabla}\eta)^2}}, \tag{2.3}$$

and condition at infinity (the assumption of an infinitely deep ocean),

$$\Phi \to 0 \qquad \text{as} \qquad z \to -\infty. \tag{2.4}$$

It can be shown that these equations can be written in the form of Hamilton's equations with η being a generalized momenta and $\Psi(\vec{r}, t) = \Phi(\vec{r}, z, t)|_{z=\eta}$ being a generalized coordinates. Specifically,

$$\frac{\partial \eta}{\partial t} = \frac{\delta E}{\delta \Psi}, \tag{2.5}$$

$$\frac{\partial \Psi}{\partial t} = -\frac{\delta E}{\delta \eta}, \tag{2.6}$$

where E is the energy of the system and the δ represents the variational derivative.

After some transformations, one obtains the equation for an envelope of the wave packet, $b(x, y, t)$ of the form (66),

$$\frac{\partial b}{\partial t} + c\frac{\partial b}{\partial x} - \frac{i}{2}\left(\lambda_{||}\frac{\partial^2 b}{\partial x^2} + \lambda_{\perp}\frac{\partial^2 b}{\partial y^2}\right) = -iw|b|^2 b. \tag{2.7}$$

Here, w is a nonlinearity constant, $\lambda_{||}$ and $\lambda_{\perp}$ are eigenvalues of the tensor $D_{\alpha\beta} = \partial^2\omega/\partial k_\alpha \partial k_\beta$ and ω and k are the wave frequency and wavevector respectively.

To simplify this equation, we introduce the variables,

$$\xi = x - ct, \tag{2.8}$$

$$R = \xi\cos\alpha + y\sin\alpha, \tag{2.9}$$

$$\lambda = \lambda_{||}\cos^2\alpha + \lambda_{\perp}\sin^2\alpha, \tag{2.10}$$

where c is the velocity of the wave, ξ is the comoving coordinate, and R is a combined position coordinate. This gives the final result of the Zakharov paper,

$$\frac{\partial\Psi}{\partial t} - \frac{i\lambda}{2}\frac{\partial^2\Psi}{\partial R^2} = -w|\Psi|^2\Psi. \tag{2.11}$$

2.1.2 Optical Rogue Waves

Ocean waves are not the only context in which rogue waves have been observed. Optical rogue waves are phenomena that have been observed in experiments (58;

57; 20; 31; 13; 11; 4). One primary distinction between optical rogue waves and oceanic rogue waves is that the Nonlinear Schrödinger Equation describes the envelope function of optical waves whereas in the oceanic context, it describes the wave itself. Generation of optical rogue waves requires generating supercontinua in the modulation instability regime (58).

Modulation Instability

Modulation instability in optical waves is a phenomenon where the steady state of a system becomes unstable which gives rise to soliton fission and breakdown of waves into wave trains. Several different effects need to be present in order to support modulation instability, including anomalous group velocity dispersion and the Kerr effect. Anomalous dispersion is characterized by an inverse relation between wavelength and group velocity or, in other words, a direct relation between group velocity and wavevector. The Kerr effect exists in media where the index of refraction depends directly on the intensity of the light traveling through it. This implies a critical amplitude below which no effect is seen.

To see how this works, one can start with the Nonlinear Schrödinger Equation as given in (2),

$$i\frac{\partial\psi}{\partial z} = \frac{1}{2}\beta_2\frac{\partial^2\psi}{\partial t^2} - \gamma|\psi|^2\psi, \tag{2.12}$$

where ψ is the envelope function of the optical wave, z is the direction of propagation along a fiber, β_2 is the group velocity dispersion parameter, and γ is the nonlinearity parameter responsible for self-phase modulation. For a time independent steady state, the solution is simply given by,

$$\psi = \sqrt{P_0} e^{i\gamma P_0 z}, \tag{2.13}$$

where P_0 is the incident power.

In order to test stability, a small perturbation of the form of $a(z,t)$ is added to the steady state solution of Eq. (2.13). Linearizing in the small perturbation gives a differential equation for a,

$$i\frac{\partial a}{\partial z} = \frac{1}{2}\beta_2 \frac{\partial^2 a}{\partial t^2} - \gamma P_0 (a + a^*). \tag{2.14}$$

Assuming the general solution is oscillatory,

$$a(z,t) = a_1 \cos(Kz - \Omega t) + i a_2 \sin(Kz - \Omega t), \tag{2.15}$$

where K and Ω are the wave number and frequency of the perturbation, respectively. Putting Eq. (2.15) into Eq. (2.14) has a nontrivial solution only when the dispersion

relation,

$$K = \pm\frac{1}{2}|\beta_2|\Omega[\Omega^2 + \mathrm{sgn}(\beta_2)\Omega_c^2] \tag{2.16}$$

is satisfied and $\Omega_c = 4\gamma P_0/|\beta_2| = 4/|\beta_2|L_{NL}$. L_{NL} is the length scale over which nonlinear effects are important.

Where the instability arises is in the case where $\beta_2 < 0$ (which corresponds to anomalous dispersion) and $\Omega < \Omega_c$. This leads to it becoming imaginary and the small perturbation grows exponentially with z. The power-dependent phase shift from the nonlinearity is from the Kerr effect.

Supercontinua

Supercontinua are pulses that are broadened in their spectra when exiting a nonlinear fiber compared to when it enters the fiber. Observation of supercontinua first came in the late 1960s (3) and since has been observed in solids, liquids (28), and gases (17; 32). The primary effects that give rise to supercontinua generation include, but are not limited to self-phase-modulation (3; 28; 17), self-focusing (17; 56), and nonlinear effects. In the literature, there is a wide range of widths that are claimed to be a supercontinuum and there is no definite threshold that separates broadening of the spectrum from a supercontinuum. An example of a supercontinuum is shown in Fig. (2.3) and is taken from (33).

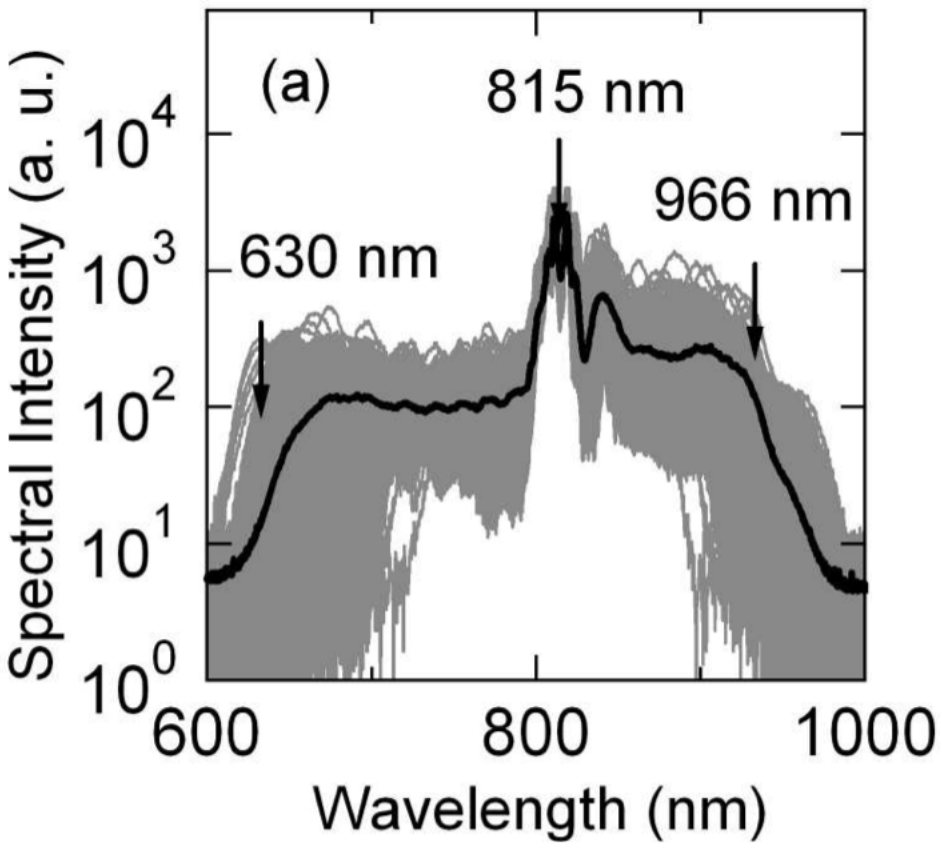

Figure 2.3: Example of a supercontinuum taken from (33). The initial pulses sent through the fiber were peaked about 815 nm and remnants of that are still evident in the supercontinuum. Intensity is still significant between 630 nm and 966 nm, however.

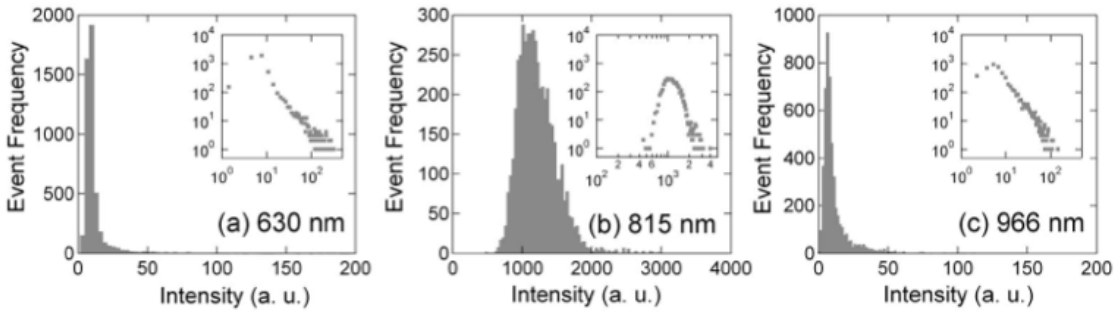

Figure 2.4: Near the peak wavelength of the supercontinuum, the behavior is basically Gaussian. Closer to the extreme values of the wavelength, the statistics exhibit L-shaped statistics. Figure taken from (33)

Statistics

Rogue waves are very rare, but very extreme events. The understanding of how frequently rogue waves occur is important to being able to predict them and potentially to control them in a laboratory situation. According to a study by Kasparian et al. (33), it is found that the relation between the size of rogue wave events and the frequency at which they occur follow L-shaped statistics. This is the same type of behavior as popularity of books and music, size and frequency of power outages, magnitudes and frequency of earthquakes, size of craters on the moon, and solar flares. The distributions from (33) are shown in Fig. (2.4).

2.2 Micromagnetic Simulation Background

And we now discuss magnetic patterns in nanoparticles. Arrays of metallic nanoparticles have been suggested to be useful in many contexts including, but not limited to high-density magnetic storage devices (64; 10), surface plasmon waveguides (47; 38),

and high-efficiency flat-panel displays (22). To accomplish these goals, many parameters need to be controlled to ensure proper functionality. These variables include size, shape, composition, crystal structure, and spacing between particles. Many methods have been suggested to accomplish this, but one promising avenue of research is through laser-induced dewetting (25; 27; 23; 26; 24; 30; 62; 37; 36) which we discuss next.

2.2.1 Self-Assembled Nanoparticle Arrays

In the field of nanotechnology, ability to achieve ordered arrays of nanoparticles in a fast, cost-effective manner is a coveted achievement. The process of laser-induced dewetting takes advantage of instabilities in a thin film, for example spinodal dewetting which occurs when attractive intermolecular forces exceed the stabilizing effect of interfacial tension (52; 51; 53; 63).

The progression from thin film to the final result of an array of nanoparticles can be seen in Fig. (2.5). As the pictures go from left to right, there is an increase in the number of laser pulses. This progression for the uniform laser case starts with the nanohole state which consists of the thin film with holes in it, resembling the surface of a sponge. Following the nanoholes, comes cells which are large defined gaps with no sign of the initial film. The polygon state is characterized by smaller shapes with some of their edges breaking into nanoparticles. Finally, the resulting state is an array of nanoparticles.

This progression for the two-beam interference case starts with the nanostripe

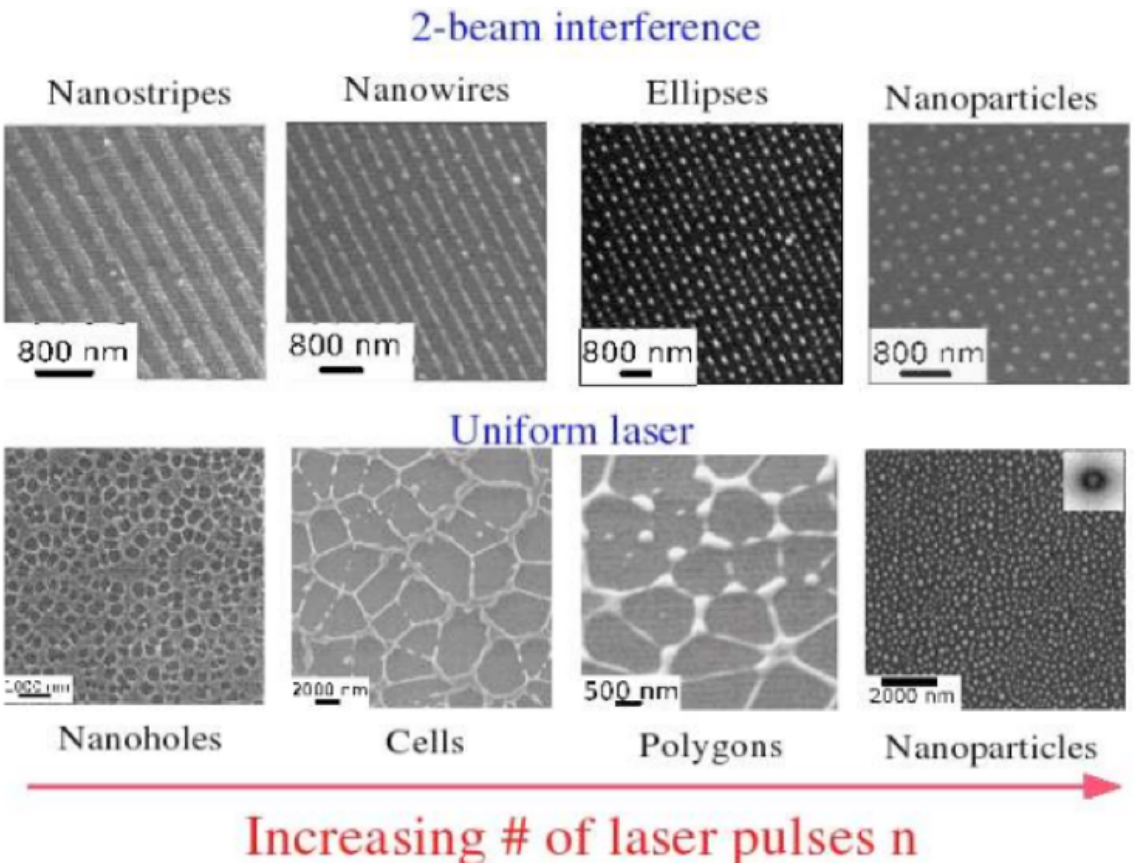

Figure 2.5: As the pictures go from left to right, there is an increase in the number of laser pulses. This shows the progression from thin film to nanoparticle array for the uniform laser and two-beam interference cases. Image courtesy of Ramki Kalyanaraman.

state which consists of the thin stripes in a regular pattern. Following the nanostripes comes nanowires which are shorter and thinner versions of the nanostripes. The ellipses configuration is characterized by nanoparticles which have a more irregular shape. Finally, the resulting state is an array of nanoparticles. It is clear from the image that the two-beam interference case has a more regular arrangement of particles.

2.2.2 OOMMF Theory

For the purposes of this research, the Object Oriented Micromagnetic Framework (OOMMF) 1.2a distribution as provided from NIST was utilized (19). The OOMMF code numerically solves the Landau-Lifshitz Ordinary Differential Equation given by,

$$\frac{d\vec{M}}{dt} = -|\bar{\gamma}|\vec{M} \times \vec{H}_{eff} - \frac{|\bar{\gamma}|\tilde{\alpha}}{M_s}\vec{M} \times \left(\vec{M} \times \vec{H}_{eff}\right), \tag{2.17}$$

where $\vec{M}$ is the magnetization, $\bar{\gamma}$ is the Landau-Lifshitz gyromagnetic ratio, M_s is the saturation magnetization, $\tilde{\alpha}$ is the damping coefficient, and H_{eff} is the effective field given by derivatives of the Gibbs free energy.

On a conceptual level, the first term on the right hand side of the Landau-Lifshitz Equation is a torque term. The second term is a damping term. This damping term has not been derived from first principles, but is added in as an empirical observation.

The Gibbs free energy, in this case, is given by (14),

$$G = \int \left(\frac{1}{2}C\left[\left(\vec{\nabla}\alpha\right)^2 + \left(\vec{\nabla}\beta\right)^2 + \left(\vec{\nabla}\gamma\right)^2\right] + w_a - \frac{1}{2}\vec{M} \cdot \vec{H}' - \vec{M} \cdot \vec{H}_0\right) dV \tag{2.18}$$

where α, β, and γ are the directional cosines, C is proportional to the exchange stiffness constant and depends on the crystal structure, w_a is the crystalline anisotropy term, $\vec{H}'$ is the demagnetization field, and $\vec{H}_0$ is the external magnetic field.

Directional cosines represent the cosine of the angle between a given vector with the three important unit vectors for a given crystal structure. The easiest way to compute these is to calculate the normalized dot product between the given vector and each unit vector. In the simple case of a cubic lattice, these unit vectors correspond to the vectors, $\hat{x}, \hat{y}$, and $\hat{z}$. For a generic vector, $\vec{A} = A_x\hat{x} + A_y\hat{y} + A_z\hat{z}$, the directional cosines take on the form of

$$\alpha = \frac{A_x}{\sqrt{A_x^2 + A_y^2 + A_z^2}} \tag{2.19}$$

$$\beta = \frac{A_y}{\sqrt{A_x^2 + A_y^2 + A_z^2}} \tag{2.20}$$

$$\gamma = \frac{A_z}{\sqrt{A_x^2 + A_y^2 + A_z^2}}. \tag{2.21}$$

The crystalline anisotropy term can be expressed in terms of anisotropy constants, K_1 and K_2, and directional cosines as,

$$w_a = K_1\left(\alpha^2\beta^2 + \beta^2\gamma^2 + \gamma^2\alpha^2\right) + K_2\alpha^2\beta^2\gamma^2. \tag{2.22}$$

Crystalline anisotropy describes the preferred directions of magnetization, known as easy axes, that arise from the crystal structure of the metal. These easy axes can arise in the form of a single axis that is a preferred direction or in the form of an easy plane where all directions are equally favored in the plane.

In the simulations, a metastable state was determined to have been reached when the maximum torque experienced by any one magnetic moment dropped below 0.2 deg/ns. Once this level of torque was reached, the magnetic state data were saved to a file along with the other properties of the system, including but not limited to, the energies associated with each contribution, overall magnetization, and number of iterations. The magnetic field was then changed to the next value and the iterations continued until saturation of the magnetization was obtained. The magnetic field steps were chosen such that half the steps (typically, a few hundred) were during the increasing field portion and the other half in the decreasing field portion. The data stored in the file were used later to generate the hysteresis plots, track the energy changes associated with the field variations, and the spatial orientations of the magnetic moments. Unless specified otherwise, the parameters chosen in the simulations correspond to those for cobalt, as shown in Table (5.1).

The parameters are sent to the code in the form of a ".mif2" file. This is a file form that is developed for the purposes of the OOMMF code. It is a cross between a list of parameters with a source code for the simulation itself. It can contain routines, variables, and calculations, but it also contains values for constants to be used in the simulation. An example of a ".mif2" file in the MIF2.1 format is shown in Appendix A.

In modeling the magnetic nanoparticles, we observed a non-trivial patterned magnetic state known as a skyrmion.

2.2.3 History of Skyrmions

Skyrmions were first introduced by Tony Skyrme in 1962 as a solution to a Lagrangian which approximates QCD at low energies (46; 55). They were introduced in an attempt to describe baryons and their interactions. Although skyrmions were not recognized immediately as a state that could appear in many contexts, in the past few decades much work has gone into showing that they can appear in a number of diverse fields. These fields include liquid crystals (65), Bose-Einstein condensates (34; 41; 67), thin magnetic films (35), quantum Hall systems (59; 12; 50; 5), and potentially vortex lattices in type II superconductors (1; 6).

This dissertation deals with the magnetic skyrmionic state which is a vortex state where the outermost spins are antiparallel to the vortex core. This can be visualized in imagining water flowing down the drain in a bath tub. Imagining the vectors pointing in the direction of flow of the water, the flow is directly downwards in the center. As the distance from the drain increases, the flow moves more in plane and goes around either clockwise or counterclockwise. This analogy breaks down, however, as the distance from the drain continues to increase, the flow of the water would have to begin moving upwards, which clearly does not happen in the context of the water in the drain. In this analogy, the local magnetic moments are being translated into the local velocity vectors. A visual representation of this from the literature can be seen in Fig. (2.6).

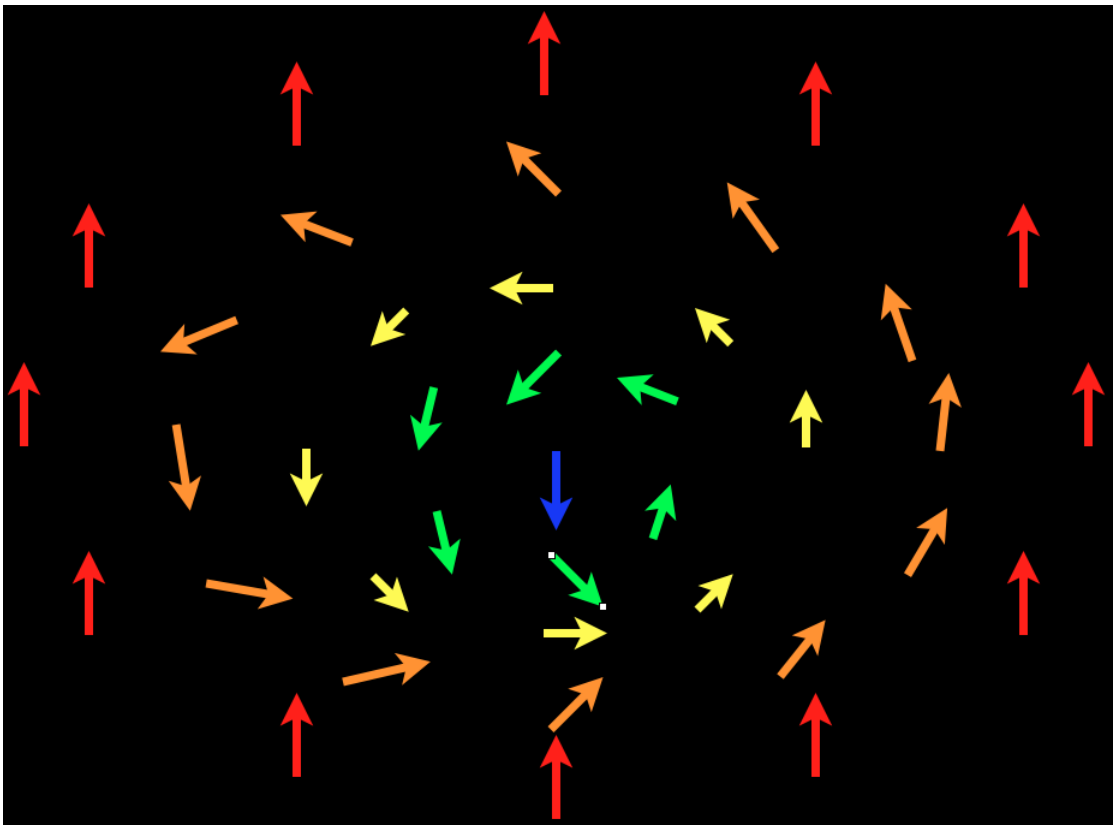

Figure 2.6: Image of a magnetic skyrmion. Color corresponds to z-component of local magnetic moment.

2.3 Correlations, Patterns, and Transitions in Low Temperature Quantum Systems

Classical amorphous systems have received much attention in recent years, specifically those that exhibit so-called jamming transition. This transition reflects the system's ability to support yield stress. We discuss a very general relation between low temperature quantum systems and classical viscous systems. This comes in the form of patterns associated with spatio-temporal correlations functions. These patterns include the jamming transition and dynamical heterogeneities.

2.3.1 Jamming Transition

To picture the jamming transition, one simply needs to picture a number of coins on a tabletop. As the number of coins increase, the chance of any coin to move without colliding with another coin decreases. At a certain density of coins, for any coin to move across the table, all the coins would need to change their position in order to accommodate that.

The jamming transition arises in a number of different systems including, but not limited to, traffic, granular materials, glasses, and close-packed spheres (39; 45; 44; 42; 43; 40). It has been proposed that this transition is a new type of phase transition to a solid state(8; 61). Coupled with this transition are diverging length scales (54; 9) and diverging time scales (21; 9).

The phase diagram of the jamming transition can be visualized in a three dimen-

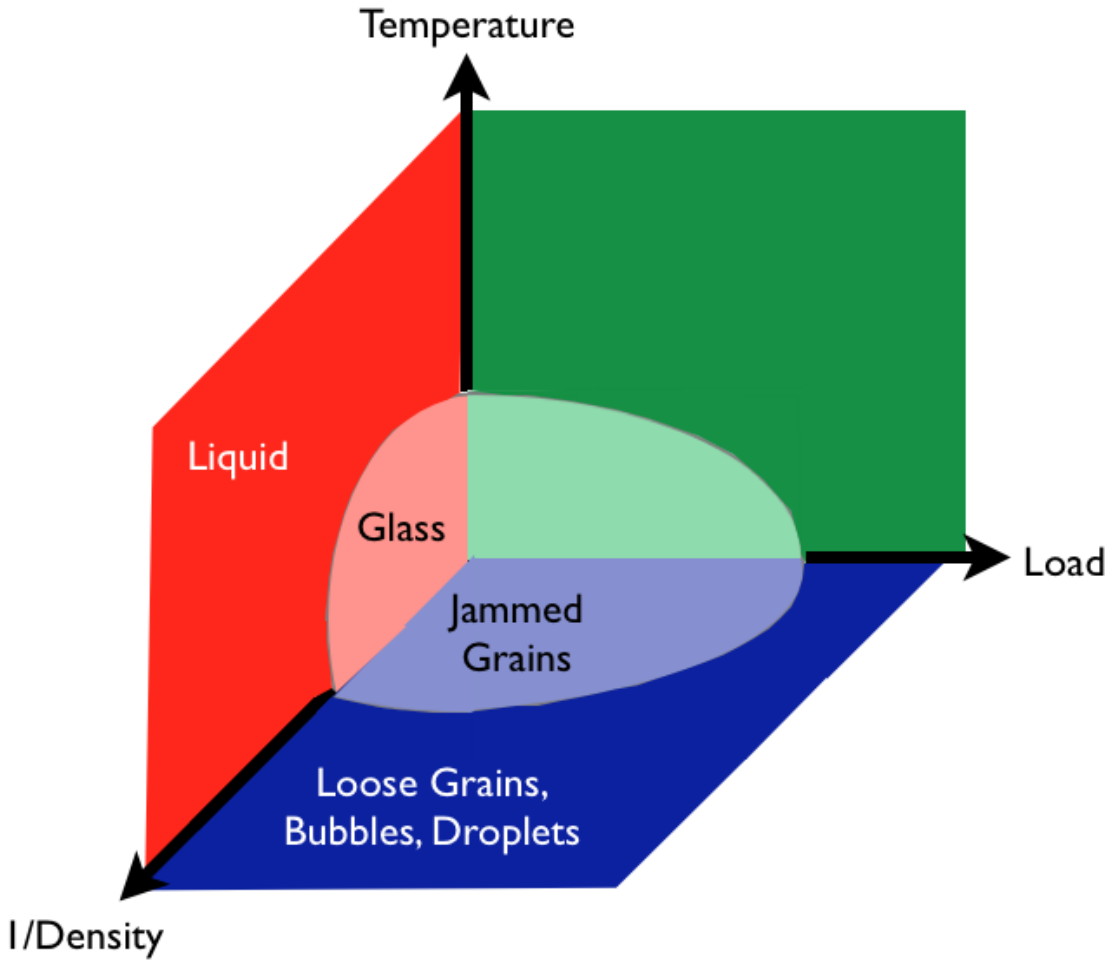

Figure 2.7: Phase diagram for the jamming transition.

sional plot of temperature, load (stress), and inverse density. This can be seen in Fig. (2.7).

2.3.2 Dynamical Heterogeneities

Dynamical heterogeneity is a concept describing non-uniform dynamcs in amorphous systems, including but not limited to, glassy systems (16; 18; 49; 48). When in a liquid phase, a system will have a broad distribution of relaxation times and behav-

iors across the whole system. As the system approaches an amorphous solid state, however, particles cease to move. and are constantly on the move which prevents any one location from staying constant for too long. This is what gives rise to the transient nature of dynamical heterogeneities. This variation can be visualized in a vector plot of velocities in a system as shown in Fig. (2.8).

Dynamical heterogeneity is typically measured via a four-point correlation function. This effectively quantifies the time and length scales associated with the density fluctuations. This can be written as

$$C_4(\vec{r},t) = \langle \frac{1}{V}\int d\vec{R}\delta\rho(\vec{R},0)\delta\rho(\vec{R},t)\delta\rho(\vec{R}+\vec{r},0)\delta\rho(\vec{R}+\vec{r},t)\rangle$$
$$-\langle \frac{1}{V}\int d\vec{R}\delta\rho(\vec{R},0)\delta\rho(\vec{R},t)\rangle\langle \frac{1}{V}\int \delta\rho(\vec{R}+\vec{r},0)\delta\rho(\vec{R}+\vec{r},t)\rangle \tag{2.23}$$

where $\delta\rho$ is a density fluctuation.

To characterize the strength of the correlation, integration over the spatial coordinate is needed which allows one to define a four-point susceptibility. This susceptibility has a maximum at the typical relaxation time for glassy systems. This can be expressed as

$$\chi_4(t) = \int d\vec{r} C_4(\vec{r},t) \tag{2.24}$$

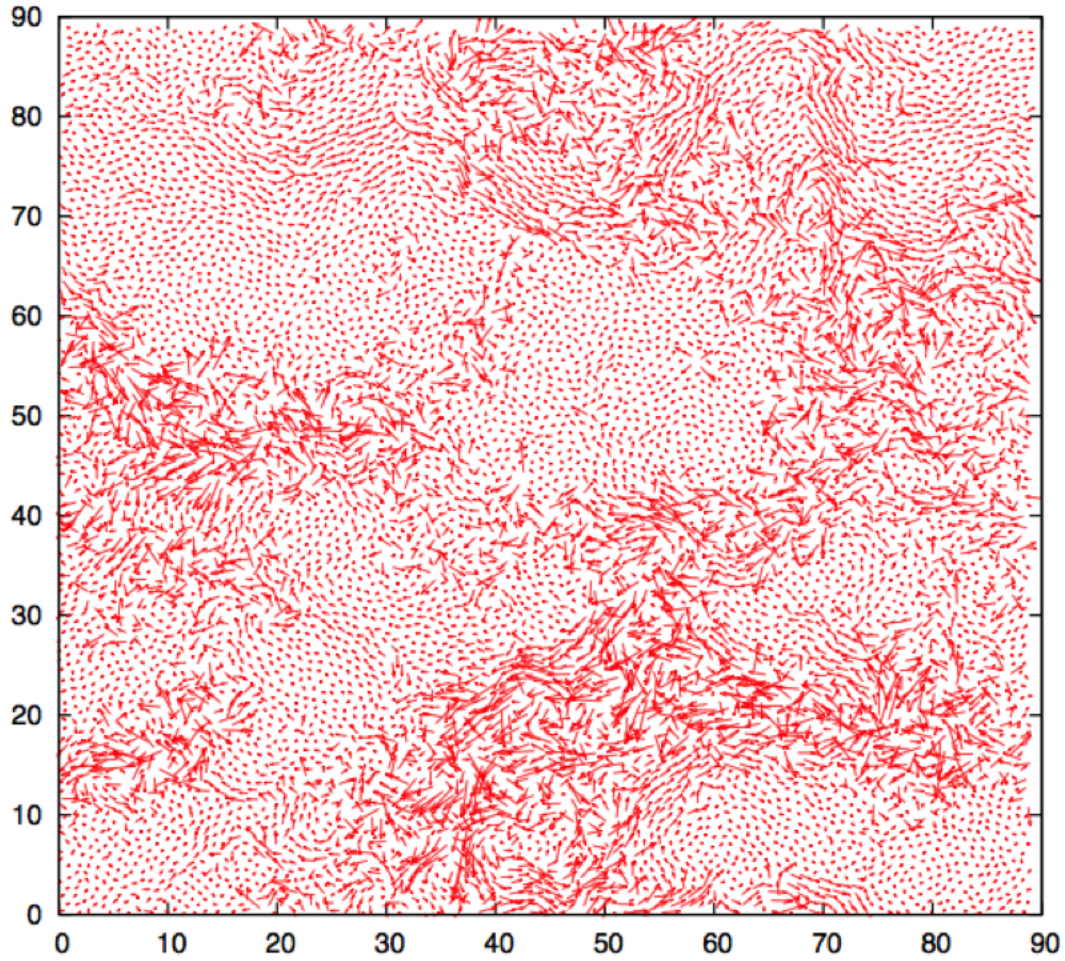

Figure 2.8: Spatial map of single particle displacements in the simulation of a Lennard-Jones model of a supercooled liquid in two spartial dimensions. Arrows represent the displacement of each individual particle in a trajectory of duration comparable to the typical structural relaxation time. This map reveals that particles with different mobilities are spatially correlated. Image used with permission of (7)

which is sometimes expressed in terms of the non-averaged correlation function,

$$C(t) = \frac{1}{V} \int d\vec{r} \delta\rho(\vec{r}, 0) \delta\rho(\vec{r}, t) \tag{2.25}$$

$$\chi_4(t) = N \left(\langle C^2(t) \rangle - \langle C(t) \rangle^2 \right). \tag{2.26}$$

Bibliography

[1] Abrikosov, A. A.: 2004, *Rev. Mod. Phys.* **76**, 975

[2] Agrawal, G.: 1995, *Nonlinear fiber optics*, Optics and photonics, Academic Press

[3] Alfano, R. R. and Shapiro, S. L.: 1970, *Phys. Rev. Lett.* **24**, 584

[4] Ankiewicz, A., Devine, N., and Akhmediev, N.: 2009, *Physics Letters A* **373(43)**, 3997

[5] Barrett, S. E., Dabbagh, G., Pfeiffer, L. N., West, K. W., and Tycko, R.: 1995, *Phys. Rev. Lett.* **74**, 5112

[6] Baskaran, G.: 2011, *arXiv:1108.3562v1*

[7] Berthier, L.: 2011, *Physics* **4**, 42

[8] Biroli, G.: 2007, *Nature Physics* **3**, 222

[9] Biroli, G. and Bouchaud, J.-P.: 2004, *EPL (Europhysics Letters)* **67(1)**, 21

[10] Black, C. T., Murray, C. B., Sandstrom, R. L., and Sun, S.: 2000, *Science* **290(5494)**, 1131

[11] Bludov, Y., Konotop, V., and Akhmediev, N.: 2009, *Physical Review A* **80(3)**, 1

[12] Brey, L., Fertig, H. A., Côté, R., and MacDonald, A. H.: 1995, *Phys. Rev. Lett.* **75**, 2562

[13] Broderick, N.: 2010, *Physics* **3**, 101

[14] Brown Jr, W. F.: 1978, *Micromagnetics*, Krieger, New York

[15] Busch, H.: 2012, *Der Untergang der Mnchen*

[16] Bhmer, R., Hinze, G., Diezemann, G., Geil, B., and Sillescu, H.: 1996, *EPL (Europhysics Letters)* **36(1)**, 55

[17] Corkum, P. B., Rolland, C., and Srinivasan-Rao, T.: 1986, *Phys. Rev. Lett.* **57**, 2268

[18] Dauchot, O., Marty, G., and Biroli, G.: 2005, *Phys. Rev. Lett.* **95**, 265701

[19] Donahue, M. and Porter, D.: 1999, *OOMMF User's Guide, Version 1.2a*, Interagency Report NISTIR 6376

[20] Dudley, J. M., Genty, G., and Eggleton, B. J.: 2008, *Opt. Express* **16(6)**, 3644

[21] Ellenbroek, W. G., Somfai, E., van Hecke, M., and van Saarloos, W.: 2006, *Phys. Rev. Lett.* **97**, 258001

[22] Fan, S., Chapline, M. G., Franklin, N. R., Tombler, T. W., Cassell, A. M., and Dai, H.: 1999, *Science* **283(5401)**, 512

[23] Favazza, C., Kalyanaraman, R., and Sureshkumar, R.: 2006a, *Nanotechnology* **17(16)**, 4229

[24] Favazza, C., Kalyanaraman, R., and Sureshkumar, R.: 2007a, *Journal of Applied Physics* **102(10)**, 104308

[25] Favazza, C., Trice, J., Gangopadhyay, a. K., Garcia, H., Sureshkumar, R., and Kalyanaraman, R.: 2006b, *Journal of Electronic Materials* **35(8)**, 1618

[26] Favazza, C., Trice, J., Kalyanaraman, R., and Sureshkumar, R.: 2007b, *Applied Physics Letters* **91(4)**, 043105

[27] Favazza, C., Trice, J., Krishna, H., Kalyanaraman, R., and Sureshkumar, R.: 2006c, *Applied Physics Letters* **88(15)**, 153118

[28] Fork, R. L., Shank, C. V., Hirlimann, C., Yen, R., and Tomlinson, W. J.: 1983, *Opt. Lett.* **8(1)**, 1

[29] "Freak Waves": 2002, *Horizon*, BBC Two

[30] Gangopadhyay, a. K., Krishna, H., Favazza, C., Miller, C., and Kalyanaraman, R.: 2007, *Nanotechnology* **18(48)**, 485606

[31] Genty, G., de Sterke, C., Bang, O., Dias, F., Akhmediev, N., and Dudley, J.: 2010, *Phys. Lett. A* **374(7)**, 989

[32] Ilkov, F. A., Ilkova, L. S., and Chin, S. L.: 1993, *Opt. Lett.* **18(9)**, 681

[33] Kasparian, J., Béjot, P., Wolf, J., and Dudley, J.: 2009, *Opt. Express* **17(14)**, 12070

[34] Khawaja, U. A. and Stoof, H.: 2001, *Nature* **411**, 918

[35] Kiselev, N. S., Bogdanov, A. N., Schafer, R., and Rosler, U. K.: 2011, *Journal of Physics D: Applied Physics* **44(39)**, 392001

[36] Krishna, H., Gangopadhyay, A., Strader, J., and Kalyanaraman, R.: 2011, *Journal of Magnetism and Magnetic Materials* **323(34)**, 356

[37] Krishna, H., Miller, C., Longstreth-Spoor, L., Nussinov, Z., Gangopadhyay, A. K., and Kalyanaraman, R.: 2008, *Journal of Applied Physics* **103(7)**, 073902

[38] Maier, S. A., Kik, P. G., Atwater, H. A., Meltzer, S., Harel, E., Koel, B. E., and Requicha, A. A.: 2003, *Nature Materials* **2**, 229

[39] Majmudar, T. S., Sperl, M., Luding, S., and Behringer, R. P.: 2007a, *Phys. Rev. Lett.* **98**, 058001

[40] Majmudar, T. S., Sperl, M., Luding, S., and Behringer, R. P.: 2007b, *Nature Physics* **3**, 260

[41] Marzlin, K.-P., Zhang, W., and Sanders, B. C.: 2000, *Phys. Rev. A* **62**, 013602

[42] Muramatsu, M., Irie, T., and Nagatani, T.: 1999, *Physica A: Statistical Mechanics and its Applications* **267(34)**, 487

[43] Nagatani, T.: 1993, *Phys. Rev. E* **48**, 3290

[44] O'Loan, O. J., Evans, M. R., and Cates, M. E.: 1998, *Phys. Rev. E* **58**, 1404

[45] Olsson, P. and Teitel, S.: 2007, *Phys. Rev. Lett.* **99**, 178001

[46] Perring, J. and Skyrme, T.: 1962, *Nuclear Physics* **31(0)**, 550

[47] Quinten, M., Leitner, A., Krenn, J. R., and Aussenegg, F. R.: 1998, *Opt. Lett.* **23(17)**, 1331

[48] Richert, R.: 1997, *The Journal of Physical Chemistry B* **101(33)**, 6323

[49] Roland, C. M. and Ngai, K. L.: 1991, *Macromolecules* **24(9)**, 2261

[50] Schmeller, A., Eisenstein, J. P., Pfeiffer, L. N., and West, K. W.: 1995, *Phys. Rev. Lett.* **75**, 4290

[51] Seemann, R., Herminghaus, S., and Jacobs, K.: 2001, *Phys. Rev. Lett.* **86**, 5534

[52] Sharma, A.: 1993, *Langmuir* **9(3)**, 861

[53] Sharma, A. and Ruckenstein, E.: 1986, *Langmuir* **2(4)**, 480

[54] Silbert, L. E., Liu, A. J., and Nagel, S. R.: 2005, *Phys. Rev. Lett.* **95**, 098301

[55] Skyrme, T.: 1962, *Nuclear Physics* **31(0)**, 556

[56] Smith, W. L., Liu, P., and Bloembergen, N.: 1977, *Phys. Rev. A* **15**, 2396

[57] Solli, D. R., Ropers, C., and Jalali, B.: 2008, *Phys. Rev. Lett.* **101(23)**, 233902

[58] Solli, D. R., Ropers, C., Koonath, P., and Jalali, B.: 2007, *Nature* **450(7172)**, 1054

[59] Sondhi, S. L., Karlhede, A., Kivelson, S. A., and Rezayi, E. H.: 1993, *Phys. Rev. B* **47**, 16419

[60] Taylor, P.: 2012, *THE SHAPE OF THE DRAUPNER WAVE OF 1ST JANUARY 1995*

[61] Trappe, V., Prasad, V., Cipelletti, L., Segre, P. N., and Weitz, D. A.: 2001, *Nature* **411**, 772

[62] Trice, J., Favazza, C., Thomas, D., Garcia, H., Kalyanaraman, R., and Sureshkumar, R.: 2008, *Phys. Rev. Lett.* **101(1)**, 017802

[63] Vrij, A.: 1966, *Discuss. Faraday Soc.* **42**, 23

[64] White, R. L.: 2000, *Journal of Magnetism and Magnetic Materials* **209(13)**, 1

[65] Wright, D. C. and Mermin, N. D.: 1989, *Rev. Mod. Phys.* **61**, 385

[66] Zakharov, V. E.: 1968, *Journal of Applied Mechanics and Technical Physics* **9**, 190

[67] Zhai, H., Chen, W. Q., Xu, Z., and Chang, L.: 2003, *Phys. Rev. A* **68**, 043602

Chapter 3

Periodic Solutions and Rogue Wave Type Extended Compactons in the Nonlinear Schrodinger Equation and ϕ^4 Theories

3.1 Introduction

The Nonlinear Schrodinger Equation (NLSE) is a very versatile equation used in many branches of physics, dictating the behavior of wave packets in weakly nonlinear media. It represents the evolution of optical waves in a nonlinear fiber (26; 16; 3; 13; 18; 27; 8), the envelope of wave packets in ocean waves in an infinitely deep ocean (5; 4; 2; 21; 24), various biological systems, and the price of options in economics

(17; 30). One common way of solving the NLSE is through the Inverse Scattering Transform which uses the idea of Lax pairs. (29; 22)

A very open problem associated with the NLSE is the development of rogue waves appearing in different media (20; 15; 25; 14). Rogue waves are large waves that seem to appear from nowhere and are, at least, 2-4 times larger in amplitude than surrounding waves. They are often preceded by a large depression referred to as a "hole in the sea" in oceanic terms. This is likely a nonlinear effect in most cases.

3.2 Nonlinear Schrodinger Equation in 1+1 Dimensions

We consider the NLSE with a drift velocity and general nonlinearity in the presence of an external potential U and an additional source term g. In general dimensions,

$$i\frac{\partial}{\partial t}\Psi = [-ic\frac{\partial \Psi}{\partial x} - \epsilon\nabla^2\Psi - \lambda F(|\Psi|^2)\Psi \\ +U(\vec{r},t)\Psi + g(\vec{r},t)], \tag{3.1}$$

where ϵ and λ are tunable real parameters, F is a general function of the squared modulus, and c is the velocity along the drift axis (chosen to be the x-axis). The general "source" term g does not make an appearance in usual NLSE. However, it can be treated following the transformation of the NLSE to a mechanical problem which underlies a central part of this work. We will ignore g and consider its effect

only in a separate later discussion. In 1+1 dimensions, we choose the ansatz

$$\Psi(x,t) = e^{-i\omega t}u(x-ct)e^{i\delta} \tag{3.2}$$

with real $u(x) \geq 0$ and $e^{i\delta}$ an arbitrary phase. This gives rise to an ordinary differential equation in u,

$$\omega u = -\epsilon\frac{d^2u}{dx^2} - \lambda F(u^2)u + U(x,t)u. \tag{3.3}$$

Following a Galilean boost to the moving frame, $x \to (x-ct)$, and a subsequent interchange of space with time, Eq. (3.3) is the equation of motion for a nonlinear oscillator of spring stiffness ω subjected to an external linear force of strength U. Under this interchange, the term $\epsilon\frac{d^2u}{dx^2}$ corresponds to the inertial term of the mass times the acceleration, and $[\omega u + \lambda F(u^2)u]$ is an effective internal forcing term. In this form, the strength of the nonlinearity is proportional to λ. In what follows, we first consider the case of $U = 0$ and then comment on non-zero U. Eq. (3.3) is that of a classical particle in an effective potential given by

$$V_{eff}(u) = \frac{\omega}{2}u^2 + \lambda\int^u dv[F(v^2)v]. \tag{3.4}$$

The energy of a classical oscillator is a constant of motion. In this case, the corresponding "energy" is given by

$$E = V_{eff}(u) + \frac{\epsilon}{2}(\frac{du}{dx})^2. \tag{3.5}$$

A particular case is that of solitons for which $u \to 0$ at large $|x - ct|$ (or large times in the corresponding mechanical problem) and consequently $E = 0$. General periodic solutions appear for general non-zero E.

Rewriting Eq. (3.3), we have

$$\int dx = \pm \int^{u} \frac{dv}{\sqrt{\frac{2E}{\epsilon} - \frac{\omega}{\epsilon}v^2 - \frac{\lambda}{\epsilon}\int^{w} \frac{d(v'^2)}{dx} F(v'^2)dv'}}. \tag{3.6}$$

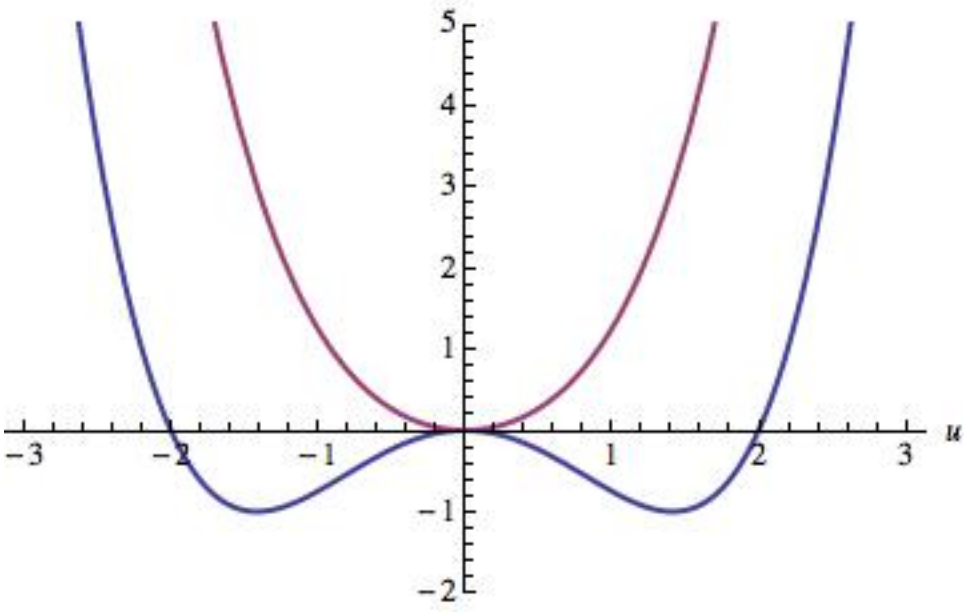

Figure 3.1: Plot of the effective potential shown in Eq. (3.4) for a cubic non-linearity ($F = u^2$) for $\omega = 2$ (single minimum) and $\omega = -2$ (double minimum) with $\lambda = 1$.

For definitiveness, we consider the cubic nonlinearity $F(u^2) = u^2$ in our Eq.(3.6). The effective potential is then $V_{eff} = \omega u^2/2 + \lambda u^4/4$. This effective potential is plotted in Fig. (3.1) for $\omega = \pm 2$ and $\lambda = 1$. In general, when $\omega < 0$, we have a double minimum of $V_{eff}(u)$. In such cases, when $E < 0$, u is restricted to be positive definite. When $\omega > 0$, we have a single miniumum at the origin ($u = 0$). In all cases, as we increase the value of E, more values of u become possible ($E \geq V_{eff}(u)$). A transition in the form of the effective potential (from a double well form to a single minimum) occurs at $\omega = 0$. In passing, we note that this is similar to what occurs in Ginzburg-Landau theories when the coefficient of the quadratic term (in this case ω) switches sign at the transition. We find that in the case of $F(u^2) = u^2$,

$$u = -\sqrt{-\frac{\omega}{\lambda} + \frac{\sqrt{4E\lambda + \omega^2}}{\lambda}} \times$$
$$cn(\sqrt{\frac{\sqrt{4E\lambda + \omega^2}}{\epsilon}}(x - ct), \frac{1}{2} - \frac{\omega}{2\sqrt{4E\lambda + \omega^2}}) \tag{3.7}$$

where cn is a Jacobi Elliptic Function. This is consistent with companion works (9; 10). The Jacobi Elliptic Functions are doubly periodic in $(x - ct)$. In this case, the periodicity of the Jacobi Elliptic integral allows a harmonic (Fourier series) expansion of u (1).

3.3 NLSE in d+1 dimensions

We consider the NLSE of Eq.(3.1) in d+1 space-time dimensions. With $r = |\vec{r}|$, $\vec{r} = r\hat{n}$, and angular momentum operator, $\vec{L}$, in d spatial dimensions, the Laplacian becomes $\nabla^2 = \frac{\partial^2}{\partial r^2} + \frac{d-1}{r}\frac{\partial}{\partial r} - \frac{\vec{L}^2}{r^2}$. If $\vec{L}^2\Psi$ is bounded in the co-moving frame at speed c, for asymptotically large r along any direction $\hat{n}$ on the unit sphere, Eq.(3.1) reads

$$i\frac{\partial}{\partial t}\Psi(r,\hat{n}) = [-\epsilon\frac{\partial^2}{\partial r^2}\Psi(r,\hat{n}) \\ -\lambda F(|\Psi|^2)\Psi(r,\hat{n}) + U(\vec{r},t)\Psi(r,\hat{n})]. \tag{3.8}$$

Along any direction $\hat{n}$, self-consistent solutions are enabled by the solution of the 1+1 dimensional NLSE with the corresponding potential U. Here, "self-consistency" is meant to imply the resulting wavefunction Ψ has dependence on $\hat{n}$ such that $L^2\Psi(r,\hat{n})$ is bounded. If we consider the substitution of $\phi = r\psi$ in the specific case of d=3 dimensions, we see that Eq.(3.8) is equal to

$$r\partial_t\phi = -\partial_r^2\phi + \frac{L^2}{r^2}\phi + U\phi + \frac{\lambda}{r^2}|\phi|^2\phi. \tag{3.9}$$

Since $\int |\psi|^2 r^2 dr$ is equal to a constant, this implies that $\int |\phi|^2 dr$ is a constant, or in other words, ϕ goes as $1/r^\alpha$ for large r where $\alpha > 1/2$. This implies that for large r, the nonlinear term goes as $1/r^{2+3\alpha}$ and can be treated as a perturbation to the LSE.

This also has implications for the small r limit as well. This limit needs to be broken down into cases where $l = 0$ and $l > 0$. For the case of $l = 0$, this simply is the case of the normal NLSE in 1+1 dimensions and have the same results as in Eq. (3.7) where $x - ct$ is replaced by r. In the case where $l \neq 0$, though, ϕ must go to zero as $r \to 0$ in order to prevent the divergence caused by L/r^2. If this is the case, the nonlinear term goes to 0 faster than the other terms and thus can, again, be considered as a perturbation to the LSE. With an ansatz of the form of Eq.(3.2), i.e., $\Psi(x,t) = e^{-i\omega t}(\sum_m u_m(r)e^{im\phi})e^{i\delta}$ with the cylindrical coordinates (r, ϕ) taken in the moving frame at velocity c along the drift (x-) axis, a series of nonlinear equations is obtained. [1]

3.4 Noise

For a non-zero U in Eq.(3.1) that depends only on the coordinates in the drifting frame at speed c, the mechanical analogue problem of Eq.(3.3) along the radial direction (or, in general, in 1+1 or 2+1 dimensions) is that of an anharmonic oscillator subjected to a linear force $uU(t)$. When $U \neq 0$, the NLSE is sometimes referred to as the Gross-Pitaevskii equation. Anderson localization (6; 11; 12; 19; 28) will occur for random $U(t)$. This means that an instanton-like solution of the mechnical problem is non-zero only in a finite interval of time. This corresponds to a spatial localization of the wavefunction Ψ over the finite interval of $|\vec{r} - ct\hat{e}_x|$ with $\hat{e}_x$ a unit vector along

[1] In the case of 2+1 dimensions, this takes the form: $\omega n_m(r) = [(-\frac{d^2}{dr^2} + \frac{1}{r}\frac{d}{dr})u_m + \lambda \sum_{m_1,m_2} u_{m_1}u_{m_2}u_{m-m_1+m_2}]$

the drift direction.

Next, we briefly consider the case of a periodic potential U of period a for $\lambda = 0$. The invariance of the second order differential equation of motion of Eq.(3.3) under translations by a implies that independent linear solutions scale as $\mu^{x/a}\Pi(x)$ with general complex μ which may be of unit modulus or real. The case with complex $|\mu| = 1$ constitutes a mechanical analogue of Bloch's theorem. Normalization demands that for an ideal periodic potential, $|\mu| = 1$. For real μ with $|\mu| > 1$, there is an instability (parametric resonance) wherein u exhibits unbounded increase. Such a case indeed occurs for a linear oscillator when the potential is $U = h\cos\gamma x$ with $|\gamma - 2\sqrt{\omega/\epsilon}| < h\sqrt{\omega/4\epsilon}$ wherein when coupled to the unperturbed u, the noise term uU acts as a periodic external force with a Fourier component having a period that is close to that of the natural resonant period of the unperturbed oscillator. This leads to large oscillations. A similar resonant Fourier component is generated by a cubic term in u. It is conceivable that such a situation is emulated for nearly periodic U over some spatial range also in the presence of non-linearities. We speculate that noise and effects from the ocean floor along with collisions with other waves may act as effective boundary conditions on the waves similar to those discussed in (7) which may trigger wave amplification in some cases.

3.5 Source terms

Following the outlined prescription of converting the NLSE with the ansatz of Eq.(3.2) into a classical mechanical problem where the spatial coordinate of the NLSE in the moving frame is replaced by a time coordinate, f becomes an external force. In particular, if in the 1+1 dimensional rendition of Eq.(3.1) we have $g = e^{i\omega t} f(x - ct)$, then instead of Eq.(3.3) we will have, in the moving frame at speed c, $\omega u = -\epsilon \frac{d^2u}{dx^2} - \lambda F(u^2)u + Uu + f(x)$. Under the interchange of space with time, this corresponds to a classical non-linear oscillator subjected to external forces ($Uu + f$). The results of the classical analysis are then replicated. For instance, in the case of $U = \lambda = 0$ and an oscillatory external "force" $f = f_0 \cos \Omega t$, a resonance appears when $\Omega = \sqrt{\omega/\epsilon}$ wherein $u \sim t \sin(\Omega t + \phi)$. The solution of the homogeneous equation (with a vanishing $U = f = 0$) is that of Eq.(3.6). Whenever the "force" f is of the form of the homogeneous solution, a resonance appears. In the case of a cubic non-linearity ($\lambda \neq 0$), a resonance occurs when f is of the form of Eq.(3.7).

3.6 Rogue Wave Type Solutions

We consider emulating rogue waves by spatially stitching solutions together at common nodes. Following the formalism associated with compactons (23), we consider wavefunctions which are piecewise continuous with cutoffs at the nodes. We can truncate the function, u, at the nodes and append on another function of our choosing with minimal error as long as the value of the function and its derivative

at these points is close to zero. This process differs from the process used to create compactons in that the wavefunction extends over all space and is not confined to a localized region. The process that we briefly describe produces an approximate solution to the NLSE (including, as a particular case, the linear Schrodinger equation) with deviations from a solution of the form of Eq.(3.3) only in the vicinity of the nodes. The initial form of these solutions can be expressed as

$$\Psi(x,0) = \begin{cases} u_1(x) & x < x_1 \\ u_2(x) & x_1 < x < x_2 \\ u_3(x) & x_2 < x \end{cases} \tag{3.10}$$

where the common nodes of the function u_2 and u_1 and u_3 are, respectively, denoted by x_1 and x_2. In higher dimensions, $\{x_i\}$ denote the coordinates of planes (either Euclidean, spherical or other) along which these solutions are stitched. Here, $\{u_i\}$ correspond to our solutions of the form of Eqs.(3.6, 3.7). We note that perfect nodes where the function and its derivative are exactly zero cannot exist, because for u of the form given in Eq.(3.7), the derivative is non-zero at all zeros of the function. Below, we once again set $\epsilon = \lambda = 1$ and consider the cubic NLSE in the absence of an external potential.

As ω becomes increasingly negative, the oscillations become narrower and taller as in Fig. (3.2(a)). For negative ω, negative E is allowed so long as $E > \frac{\omega}{\lambda}$. A form for negative E is shown in Fig. (3.2(b)). Although wavefunctions Ψ formed by piecewise

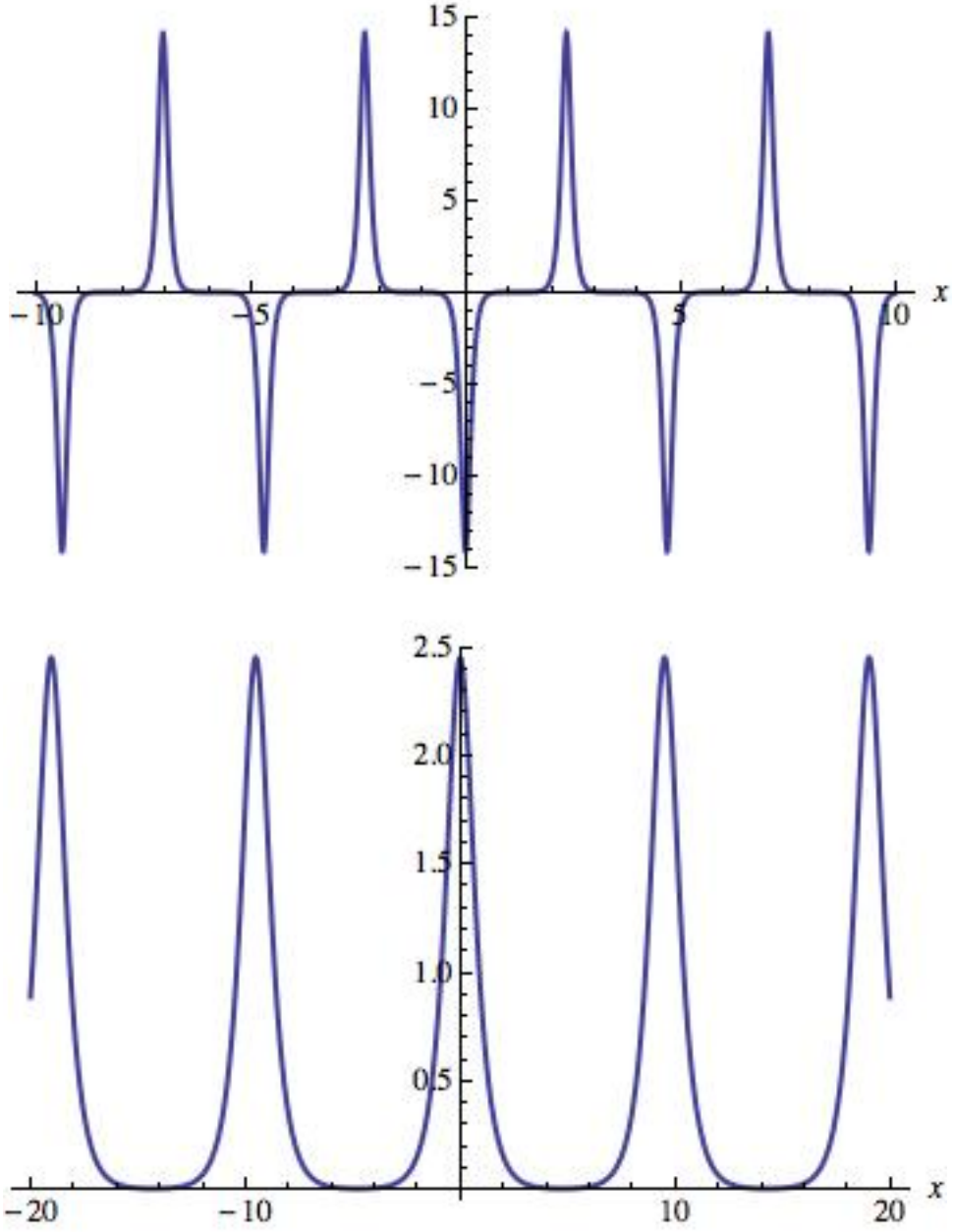

Figure 3.2: Plots of the function u at $t = 0$ for $\lambda = 1$, $\epsilon = 1$, and (a) $E = 10^{-6}$, $\omega = -10^2$ and(b) $E = -10^{-5}$, $\omega = -3$.

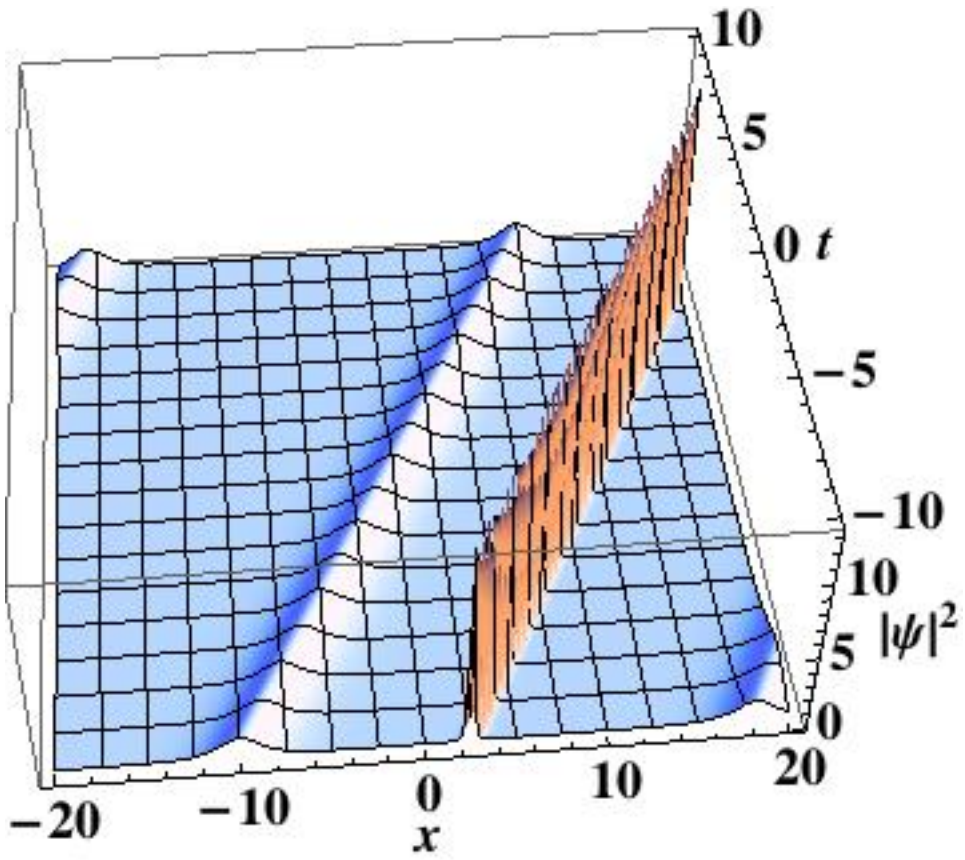

Figure 3.3: Plot of $|\Psi|$ of Eq. (3.10) with $c = 1$, $\omega_2 = -10$, $\omega_1 = \omega_3 = -1$, $E = 10^{-12}$, and $x_1 = 5.5$ and $x_2 = 20$. In this plot, we shift $(x - ct - x_0) \to x$ with $x_0 = 15$.

stitching such solutions are special, it is clear that in order to have transient rogue wave type phenomena, the current $\vec{j}$ cannot be spatially uniform (with a velocity c) in the rogue wave region. Far away where the current is of uniform speed c, it is of the form given by Eqs.(3.6, 3.7).

A wave u_2 of large amplitude by comparison to u_1 and u_3 emulates a rogue wave. A plot of $\Psi(x, t = 0)$ is provided in Fig. (3.3). The continuity equation $\frac{\partial \rho}{\partial t} + \vec{\nabla} \cdot \vec{j} = 0$ with the density given by $\rho = |\Psi|^2$ and the current $\vec{j} = i\epsilon(\Psi\vec{\nabla}\Psi^* - \Psi^*\vec{\nabla}\Psi)$ applies to the NLSE. For wavefunctions of the form of Eq.(3.10) with real u_i, the current $\vec{j} = 0$ at all points apart from the nodes. If an interpolating form is chosen near the nodes, the current j assumes non-zero values only in the regions close to the nodes. If we consider the co-moving frame and define $P = \int_{x_1}^{x_2} \rho \, \mathrm{d}x$ where $\rho = |\psi|^2$, then integrating the continuity equation gives

$$\frac{\mathrm{d}P}{\mathrm{d}t} = j_1 - j_2 \tag{3.11}$$

where j_1 andj_2 are the currents at x_1 and x_2, respectively. If we consider a rogue wave centered about $x = 0$ extending from $x = -a$ to $x = a$ and define $P_o = \int_{X-a}^{X+a} \rho \, \mathrm{d}x$ with $X \gg 0$, then with P the integral over the region of extension of the rogue wave, we can define the lifetime τ of the rogue wave as the time for P in the region of the wave to arrive at P_o. We then find that

$$\tau = \int_{P_o}^{P} \frac{\mathrm{d}P}{j_2 - j_1} \tag{3.12}$$

Alternatively, to avoid the possible problem of slow convergence to P_o, we can consider the half life of the rogue wave:

$$\tau_{1/2} = \int_{(P+P_o)/2}^{P} \frac{\mathrm{d}P}{j_2 - j_1} \tag{3.13}$$

We can concretely see the behavior of a rogue wave type solution by evolving rogue wave initial conditions according to the linear, free-particle Schrodinger equation (LSE). The behavior of wavefunctions under the LSE should give us qualitative understanding of the time evolution of rogue waves. One aspect of the LSE that is worth noting at this point is it's time-reversal symmetry.

In the co-moving frame, we can write down rather general initial conditions for a rogue wave as $\psi(x,0) = \cos x + \alpha e^{-x^2}$, with $(1+\alpha)^2$ the amplitude of the rogue wave relative to the background, typically between 2 and 4. Evolving $\psi(x,0)$ according to the LSE, we find that

$$\psi(x,t) = e^{-\frac{i}{2}t}\cos x + \alpha \frac{e^{\frac{-x^2}{1+2it}}}{\sqrt{1+2it}} \tag{3.14}$$

The amplitude of the rogue wave at the origin is

$$|\psi(0,t)|^2 = 1 + \frac{\alpha^2}{\sqrt{1+4t^2}} + \alpha\frac{\sqrt{1-2it}}{\sqrt{1+4t^2}}e^{\frac{i}{2}t} + c.c. \tag{3.15}$$

After an initial drop in amplitude, the amplitude of the oscillations at $x = 0$ decays to zero as $\frac{1}{\sqrt{t}}$.

For this case, we can also calculate the current discussed above which can be found analytically to have the magnitude.

$$j(x,t) = -\frac{i\epsilon}{(1+4t^2)^{3/2}} e^{-\frac{it}{2}-\frac{2x^2}{1+4t^2}} \alpha \Bigg(8ie^{\frac{it}{2}} tx\alpha + 2\left(e^{\frac{x^2}{1+2it}} \sqrt{1-2it}(1+2it) + ie^{it+\frac{x^2}{1-2it}} \sqrt{1+2it}(i+2t) \right) x\cos(x) - \left(e^{\frac{x^2}{1+2it}} \sqrt{1-2it} - e^{it+\frac{x^2}{1-2it}} \sqrt{1+2it} \right) \left(1+4t^2\right) \sin(x) \Bigg). \tag{3.16}$$

This can then be used to calculate the halflife of the rogue wave solutions as discussed in Eq. (3.13).

3.7 The NLSE and Rogue Waves in a ϕ^4 Model

We next consider the ϕ^4 theory given by the Lagrangian density

$$\mathcal{L} = \frac{1}{2}\partial^\mu \phi^* \partial_\mu \phi - \frac{m^2}{2}|\phi|^2 - \frac{\lambda}{4!}|\phi|^4, \tag{3.17}$$

with ϕ a complex scalar field and implicit summation over space-time coordinates μ. The Euler-Lagrange equation, in the non-relativistic limit, is a NLSE with a potential shift, m:

$$i\phi_t = -\frac{\nabla^2}{2m}\phi + \frac{\lambda}{12m}|\phi|^2\phi + m\phi \tag{3.18}$$

Solutions are given by those of Eq. (3.1) with $F = |\Psi|^2$ multiplied by e^{-imt}. If we discretize the ϕ^4 Lagrangian density and consider a 2-dimensional lattice of points with spacing Δ, the imaginary time ($t = i\tau$) Lagrangian becomes

$$L = \sum_{i,j} \left[\frac{1}{2} |\dot{\phi}_{ij}|^2 + \frac{16 + m^2\Delta^2}{2\Delta^2} |\phi_{ij}|^2 + \frac{\lambda}{4!} |\phi_{ij}|^4 \right] - \frac{1}{\Delta^2} \sum_{\alpha} \delta_\alpha \phi_{ij} \phi_{kl} \tag{3.19}$$

where the indices i, j denote the two Cartesian coordinates of points in the plane, α denotes each pair $(i, j), (k, l)$, and δ_α is zero for non-adjacent and one for adjacent oscillator pairs.

In the linear ($\lambda = 0$) case, the system is quadratic and solvable by diagonalization. We analyzed the time evolution for different parameters by a perturbative scheme in λ. In order to underscore the ubiquitous nature of rogue waves (including, as noted in some of our earlier discussions (e.g., Eq.(3.10), their presence already at the linear level), we plot below the evolution of an initial rogue wave state for the coupled linear oscillator Lagrangian of Eq. (3.19) with the parameters $m = 2$ and $\Delta = 1$. The even appearance and low amplitude of the surface at large times illustrates that, already at a linear level (i.e., that with $\lambda = 0$), the dispersion of the normal modes of the unperturbed sysetm ($\lambda = 0$) enables an evolution of steady states into rogue wave configurations. As the theory is *time-reversal* invariant, we can conclude that a steady state given by Fig. (3.4(b)) could evolve into the rogue wave in Fig. (3.4(a)).

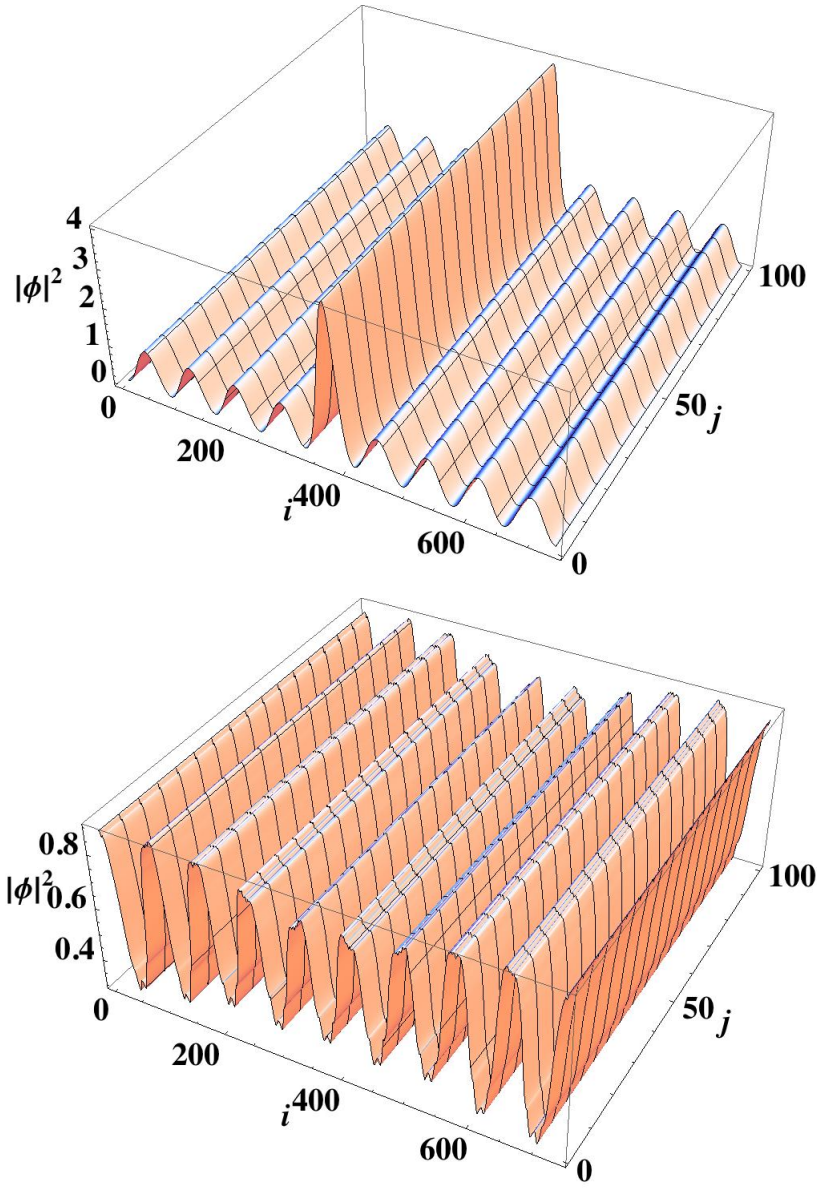

Figure 3.4: (a) shows a region of the cell surrounding an initial Gaussian rogue wave on a cosine background where $(i,\ j)$ denote Cartesian coordinates and $|\phi|^2$ denotes the modulus of the squared amplitude. (b) shows the same system at large times ($t = 60,000$ iteration steps).

3.8 Conclusions

We investigated the NLSE by considering a corresponding classical mechanics problem of non-linear oscillators. The focus was on determining oscillatory waves with a general drift velocity c. By invoking this analogy,

(1) We determined solutions to general NLSE with a general drift velocity c in 1+1 dimensions for an arbitrary non-linearity F in Eq.(3.1) . The general result is that of Eq.(3.6).

(2) We discussed solutions in general dimensions for large radial coordinates.

(3) We discussed the effects of noise and external sources.

(4) We demonstrated that solutions could potentially be truncated and attached to each other (as in Eq. (3.10) in order to create approximate solutions that behave very much like a rogue wave. We thus introduced the notion of *"generalized compactons"* which unlike usual compactons (and solitons) have a *non-zero (periodic) background*. The lifetime of such solutions scales as the reciprocal of difference in currents in the vicinity of the stitching points as given by Eq.(3.12). We qualitatively saw the behavior of the amplitude of a rogue wave over time by solving the linear Schrodinger equation for rogue wave-like initial conditions.

(5) We, specifically, employed considerations of the *continuity equation* to discuss lifetimes of rogue wave type states. (6) We reported on the appearance of rogue waves in ϕ^4 theories. Specifically, we modeled rogue waves in a system of coupled oscillators. We showed that this approach allows initial rogue wave-like conditions to evolve into

what appears to be a steady state. By *time-reversal invariance* of the equations of motion, we can conclude that rogue waves can evolve out of a steady state of that form.

Bibliography

[1] Abramowitz, M. and Stegun, I. A. (eds.): 1972, *Handbook of Mathematical Functions*, Dover Publications, See, in particular, section 16.23

[2] Akhmediev, N., Ankiewicz, A., and Soto-Crespo, J. M.: 2009a, *Phys. Rev. E* **80(2)**, 026601

[3] Akhmediev, N. and Mitzkevich, N.: 1991, *IEEE J. Quantum Electron.* **27(3)**, 849

[4] Akhmediev, N., Soto-Crespo, J., and Ankiewicz, A.: 2009b, *Phys. Lett. A* **373(25)**, 2137

[5] Akhmediev, N., Soto-Crespo, J. M., and Ankiewicz, A.: 2009c, *Phys. Rev. A* **80(4)**, 043818

[6] Anderson, P.: 1958, *Phys. Rev.* **109(5)**, 1492

[7] Berry, M.: 2007, *Proc. R. Soc. A* **463(2087)**, 3055

[8] Bludov, Y. V., Konotop, V. V., and Akhmediev, N.: 2009, *Opt. Lett.* **34(19)**, 3015

[9] Carr, L. D., Clark, C. W., and Reinhardt, W. P.: 2000a, *Phys. Rev. A* **62(6)**, 063610

[10] Carr, L. D., Clark, C. W., and Reinhardt, W. P.: 2000b, *Phys. Rev. A* **62(6)**, 063611

[11] Chabanov, A., Stoytchev, M., and Genack, A.: 2000, *Nature* **404(6780)**, 850

[12] Cheng, Y. and Adhikari, S. K.: 2010, *Phys. Rev. A* **82(1)**, 013631

[13] Dudley, J. M., Genty, G., and Eggleton, B. J.: 2008, *Opt. express* **16(6)**, 3644

[14] Dyachenko, A. I. and Zakharov, V. E.: 2005, *JETP Lett.* **81(6)**, 255

[15] Efimov, V. B., Ganshin, A. N., Kolmakov, G. V., McClintock, P. V. E., and Mezhov-Deglin, L. P.: 2008, *AIP Conference Proceedings* **1076(1)**, 53

[16] Genty, G., de Sterke, C., Bang, O., Dias, F., Akhmediev, N., and Dudley, J.: 2010, *Phys. Lett. A* **374(7)**, 989

[17] Ivancevic, V.: 2010

[18] Kasparian, J., Béjot, P., Wolf, J., and Dudley, J.: 2009, *Opt. Express* **17(14)**, 12070

[19] Lagendijk, A., van Tiggelen, B., and Wiersma, D. S.: 2009, *Phys. Today* **62(8)**, 24

[20] Marklund, M. and Stenflo, L.: 2009, *Physics* **2**, 86

[21] Milovic, D. and Biswas, A.: 2009, *International Journal of Nonlinear Science* **7(4)**, 420

[22] Osborne, A. R.: 2010, *Nonlinear Ocean Waves and the Inverse Scattering Transform*, Academic Press

[23] Rosenau, P. and Hyman, J. M.: 1993, *Phys. Rev. Lett.* **70(5)**, 564

[24] Ruban, V. P.: 2006, *Phys. Rev. E* **74**, 036305

[25] Ruban, V. P.: 2007, *Phys. Rev. Lett.* **99(4)**, 044502

[26] Solli, D. R., Ropers, C., and Jalali, B.: 2008, *Phys. Rev. Lett.* **101(23)**, 233902

[27] Solli, D. R., Ropers, C., Koonath, P., and Jalali, B.: 2007, *Nature* **450(7172)**, 1054

[28] Störzer, M., Gross, P., Aegerter, C. M., and Maret, G.: 2006, *Phys. Rev. Lett.* **96(6)**, 063904

[29] Tracy, E. R. and Chen, H. H.: 1988, *Phys. Rev. A* **37(3)**, 815

[30] Zhen-Ya, Y.: 2010, *Commun. in Theor. Phys.* **54(5)**, 947

Chapter 4

The Demagnetizing Factor of a Hemisphere

4.1 Introduction

Demagnetizing factors have been an area of study for more than a century. Earliest theoretical work dates back to Thompson (21) and Maxwell (14) whereas experiments date back to Rowland (17) with ballistic galvanometers. Determining demagnetizing factors can be very complicated, and thus only a select number of geometries have ever been calculated. The results for a general ellipsoid can be found in work from Osborne (15). The results for a circular cylinder can be found in work from Chen et al. (7). The case of a transversely magnetized, infinite prism is found in work from Brown (5) and the case of a square-faced prism can be found in work from Joseph (11). The general rectangular prism is calculated by Aharoni in (1). Analytical expressions

for the demagnetization factor for objects devoid of symmetry (irregular shaped) are impossible to derive.

As shown in experiments (13; 12), self-organized nanoparticles on low energy substrates form hemispherical shapes, the most natural shape for particles to form due to surface tension effects. Understanding the magnetic behavior of a hemisphere is very important in the field of micromagnetics.

4.2 Origin of Demagnetization Energy

The origin of the demagnetization energy can be derived from the interaction of a lattice of dipoles at T=0 (6). The potential energy of such a system is given by

$$U = -\frac{1}{2}\sum_i \vec{m}_i \cdot \vec{h}'_i, \tag{4.1}$$

where $\vec{h}'_i$ is the field at position i from all other dipoles. This field can be written as

$$\vec{h}'_i = \vec{H}' + \frac{4}{3}\pi\vec{M} + \vec{h}''_i, \tag{4.2}$$

where $\vec{H}'$ is the megascopic field from the poles due to $\vec{M}$, and $\vec{h}''_i$ is the field of the dipoles local to site i. In general, $\vec{h}''_i$ depends on the crystal lattice structure. In the continuum limit, the sum becomes an integral of the form

$$U = -\frac{1}{2}\int \vec{M} \cdot (\vec{H}' + \frac{4}{3}\pi\vec{M} + \vec{h}_i'')dV. \tag{4.3}$$

The second term in this expression is a constant proportional to M_s^2 and can be ignored. The third term depends only on the crystal structure and local magnetization and is usually grouped with the crystalline anisotropy energy, leaving

$$U = -\frac{1}{2}\int \vec{M} \cdot \vec{H}' dV. \tag{4.4}$$

The calculation detailed below follows the series of steps outlined in Stoner's paper on calculating the demagnetizing factor of the general ellipsoid (18), which draws an analogy between magnetic and gravitational potentials and relating the demagnetizing field to the second derivative of the magnetic potential. In general, the demagnetizing field can be related to the demagnetization factor via $H_i = -N_i M_i$, where H_i is the i-th component of the demagnetizing field, N_i is the demagnetizing factor in the i-th direction, and M_i is the i-th component of the magnetization. When using cgs units, the demagnetizing factors in each direction sum to 4π. Some literature chooses to use mks units such that the demagnetizing factors sum to 1, and those are typically denoted by D_i rather than N_i. For the remainder of this paper, the 4π normalization will be maintained.

4.3 Results

Starting with the expression for the gravitational potential of a hemisphere as given by (16),

$$U(R,r,z) = -\frac{1}{3}\pi G\rho(-r^2+2z^2+3R^2+\frac{2R^3}{\sqrt{r^2+z^3}}) + \frac{1}{3}G\rho\frac{1}{z\sqrt{(R+r)^2+z^2}}\Bigg(-z^2(3r^2+3z^2+R^2)K + 3z^2(r^2+z^2+2rR+R^2)E - (r^2-2z^2-3R^2+\frac{2R^3}{\sqrt{r^2+z^2}})(r^2+z^2+rR-(r+R)\sqrt{r^2+z^2})\Pi_1 + (-r^2+2z^2+3R^2+\frac{2R^3}{\sqrt{r^2+z^2}})(r^2+z^2+rR+(r+R)\sqrt{r^2+z^2})\Pi_2\Bigg) \quad (4.5)$$

where $r = \sqrt{x^2+y^2}$, R is the radius of the hemisphere, $r < R$, and $z < 0$, K is the complete elliptic integral of the first kind, E is the complete elliptic integral of the second kind, and Π is the complete elliptic integral of the third kind, and

$$K = K\left(\frac{4Rr}{(R+r)^2+z^2}\right) \quad (4.6)$$

$$E = E\left(\frac{4Rr}{(R+r)^2+z^2}\right) \quad (4.7)$$

$$\Pi_1 = \Pi\left(\frac{2r}{r+\sqrt{r^2+z^2}}, \frac{4Rr}{(R+r)^2+z^2}\right) \quad (4.8)$$

$$\Pi_2 = \Pi\left(\frac{2r}{r-\sqrt{r^2+z^2}}, \frac{4Rr}{(R+r)^2+z^2}\right) \quad (4.9)$$

The demagnetizing factor of any cartesian direction can be calculated by taking the second spacial derivative of the magnetic potential relative to that coordinate.

The magnetic potential is the gravitational potential in the case where $G = \rho = 1$. The final derivative expressions are too lengthy to present here, but checks can be made to ensure that these are indeed the correct expressions, such as evaluating the demagnetization factor in the x-direction at the origin and at the apex of the hemisphere, $(0, 0, -R)$. These will have values of $\frac{2\pi}{3}$ and $\frac{5\pi\sqrt{2}}{6}$, respectively as described in (9).

In order to take the limit approaching the origin, one can simplify the expression for the demagnetizing factor when all coordinates are equal ($x = y = z$), do a series expansion around $z = 0$, and keep the leading order terms, obtaining $\frac{2\pi}{3}$. Similarly, for the case of the apex of the hemisphere, one can set $z = -R$ and $x = y$ and again take the limit as y goes to zero. A series expansion about $y = 0$ can be written and keeping the leading order terms, the value of $\frac{5\pi\sqrt{2}}{6}$ is obtained.

It is most useful to report an expression for the demagnetizing factor averaged over the sample volume rather than a spatially dependent expression, so that a purely geometrical quantity can be defined. In the case of a hemisphere, the geometry is uniquely specified by one parameter, R. Because the demagnetizing factor is a dimensionless quantity, the spatially averaged demagnetizing factor is independent of the radius of the hemisphere in question. Therefore, calculating the spatially averaged demagnetizing factor of one hemisphere, is true for all hemispheres. Integrating the demagnetizing factor over the volume of the hemisphere analytically proves to be cumbersome, so numerical integration found the spatially averaged demagnetizing factor of a hemisphere for the x-direction to be $\langle N_x \rangle \approx 3.898$.

4.4 General Method for Calculating Demagnetizing Factors

Another way to calculate a spatially averaged demagnetizing factor in a system of arbitrary geometry is to calculate the demagnetization energy of a saturated system numerically. For a system with a uniform magnetization, the field and exchange energies are zero and thus all energy lies in the demagnetization energy. By systematically adjusting the spatial parameters that determine the geometry of the system, one can map how each parameter modifies the demagnetization energy of the system overall.

The demagnetizing energy density of a system that is uniformly magnetized is given by the expression

$$\epsilon_D = \frac{1}{2}\mu_0 M_s^2 N_i, \tag{4.10}$$

where N_i is the demagnetizing factor in the direction of the uniform magnetization. In general, the demagnetizing factor can be spatially dependent, but in simple cases it is a constant. Without knowing the demagnetizing factor when integrating over the volume, one obtains,

$$E_D = \frac{1}{2}\mu_0 M_s^2 \langle N_i \rangle. \tag{4.11}$$

One possible way to do this, and the way used in this work, is to use the Object Oriented Micro-Magnetic Framework (OOMMF) simulation code (8). OOMMF numerically solves the Ginzburg-Landau-Lifshitz equation by minimizing energy terms including, but not limited to, field energy, demagnetization energy, and exchange energy. One can apply arbitrarily large fields to a system of any geometry, and the code will provide a numerical value for the demagnetization energy.

Because OOMMF calculates E_D numerically, one can solve for the spatially averaged demagnetizing factor as it changes with the parameters determining the shape of the system. In other work done by these authors, simulations of Cobalt hemispheres were done, from which, spatially averaged demagnetizing factors were obtained (10). To ensure that the energy density of the perfectly saturated state was obtained, fits to the data were done of the form of arctangents and the limit as the field approached infinity was used as shown in Fig. (4.1).

Through simulations of hemispheres of various radii, the demagnetization energy of a single domain state is known within the saturation regions of the hysteresis curves. As expected the plot of the demagnetization energy versus the radius cubed gives a linear relationship and from the slope, the demagnetization factor of a hemisphere can be calculated. Applying the field along the x-, y-, and z-directions gives the demagnetizing factors in each of these directions. The validity of this method can be checked to ensure they are normalized to 4π and can be calculated directly through numerics and the analytic method discussed above.

This can be seen in Fig. (4.2) where the demagnetization energy is plotted versus

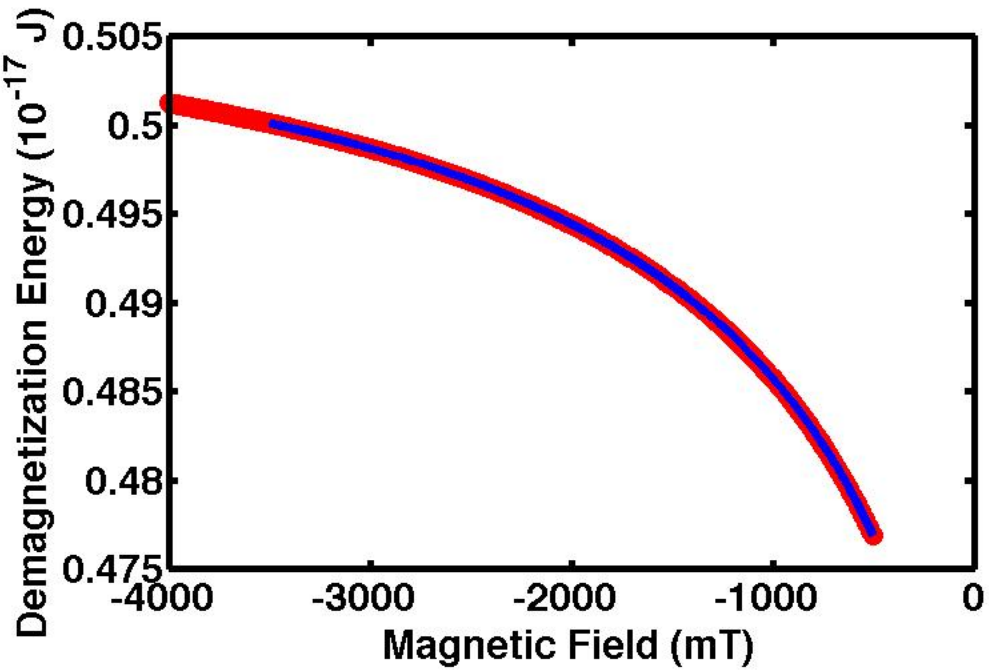

Figure 4.1: Plot of demagnetization energy density in J/m^3 versus magnetic field strength. Data points shown in red and the fit is shown in blue. To obtain the demagnetization energy density of the saturated state, the limit as the field went to infinity was taken.

the radius of the hemisphere cubed. This is for the case of the field applied in the z-direction, which corresponds to the axis perpendicular to the face of the hemisphere, thus giving the demagnetizing factor in that direction. The slope of this line is $1.1948 \times 10^{-21} J/nm^3$. From this slope, A, and the relationship

$$\langle N_z \rangle = \frac{A}{1/(8\pi)\mu_0 M_s^2 \times (2/3)\pi} = 6.32453. \tag{4.12}$$

Because the demagnetizing factors normalize to 4π and the x- and y-directions are symmetric with each other, it can be determined that $N_x = N_y \approx 3.121$, approximately 20% different from the analytic calculation of $N_x \approx 3.898$.

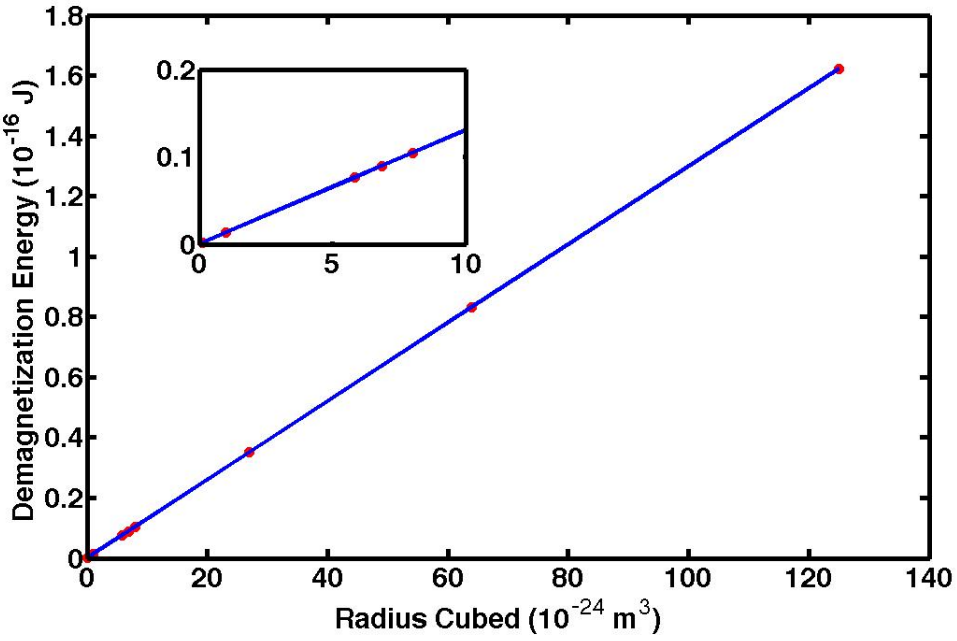

Figure 4.2: Plot of demagnetization energy versus radius (of hemisphere) cubed. The field is applied perpendicular to the plane of the face of the hemisphere.

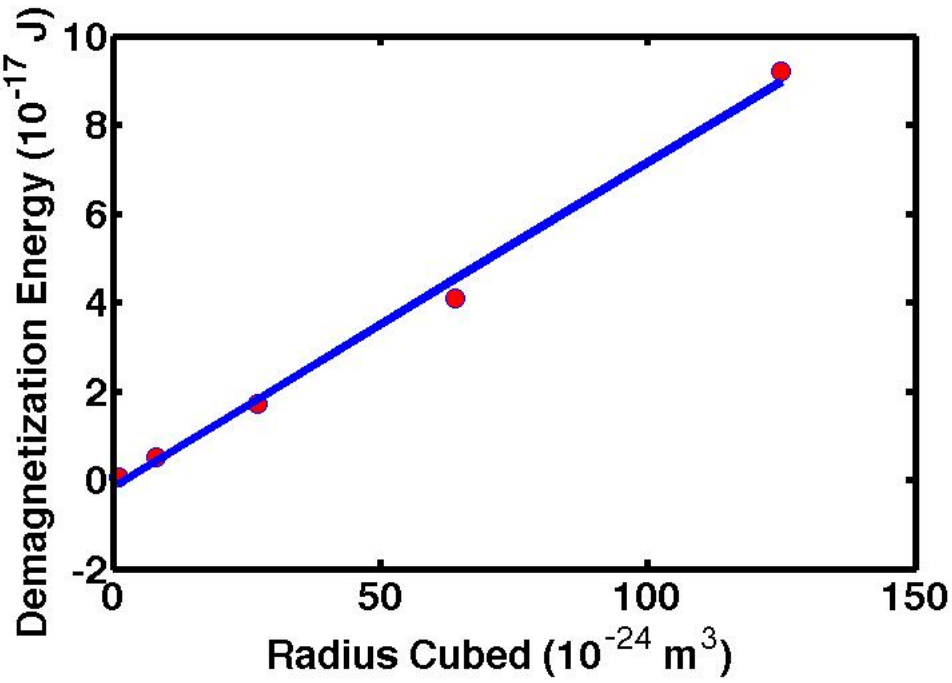

Figure 4.3: Plot of demagnetization energy versus radius (of hemisphere) cubed. The field is applied in the plane of the face of the hemisphere.

Similarly, this method can be recreated for the set of data where the field is applied in the plane of the face of the hemisphere. When doing this analysis, the slope of the plot is $7.322 \times 10^{-22} J/nm^3$. Using Eq. (4.12) and the slope from Fig. (4.3), the demagnetizing factor in the x-direction, thus equivalently in the y-direction, is 3.568, which corresponds to a demagnetizing factor in the z-direction of 5.430. This is approximately 8% different from the analytical calculation of $N_x \approx 3.898$. The gap between these values and the true value as calculated from the analytic expression can be closed by simulating more radii and with finer grid spacing as to better approximate the continuum limit.

4.5 Using Shape Function Formalism

An extensive body of work has been created by Beleggia et al. in (2; 19; 20; 3; 4) where a formalism is introduced to calculate the demagnetization factor of general geometries. This is done by introducing a shape function $D(\vec{r})$ which is equal to unity inside of the shape and zero outside.

Beleggia et. al. calculated demagnetizing factors using the formalism of shape functions in real space and shape amplitudes in Fourier space. Using this formalism to calculate the demagnetizing factor for a hemisphere is as follows. The shape amplitude for a hemisphere is given by a limiting case of Eq (30) in reference (19),

$$D(k) = 2\pi \sum_{l=0}^{\infty} (-i)^l [P_{l-1}(0) - P_{l+1}(0)] P_l(\cos\theta) \kappa_l(k, R), \tag{4.13}$$

where P_i are the Legendre Polynomials and $\kappa_l(r, R) = \int_0^R d\rho \rho^2 j_l(k\rho)$ and j_l are the spherical Bessel functions.

This implies that the demagnetizing factor can be calculated as a function of the radius, r. The spatially dependent demagnetizing factor in the x-direction can be calculated from

$$N(r) = \frac{1}{2\pi} \int d^3\vec{k} \frac{D(k)}{k^2} k_x^2 e^{i\vec{k}\cdot\vec{r}}. \tag{4.14}$$

Expressing the exponential as plane waves,

$$e^{i\vec{k}\cdot\vec{r}} = 4\pi \sum_{l=0}^{\infty} i^l j_l(kr) \sum_{m=-l}^{+l} Y_{lm}^*(\theta', \phi') Y_{lm}(\theta, \phi), \tag{4.15}$$

gives a product of infinite sums. Although this method will give the correct expression for the demagnetizing factor in the x-direction, it is significantly more laborious than our direct method discussed above.

4.6 Using Shape Anisotropy to Control Jumps in Hysteresis

Shape anisotropy can offer favored directions which can be aligned at different angles to each other. Having an array of nanoparticles with a variance in the level of anisotropy, a customized hysteresis loop could be created. When applying a field along the easy axis of a shape, the hysteresis behavior of that shape will be of the square loop type. When applying a field perpendicular to the easy axis, it will feature an intermediate region between flipping where the magnetization switches to be perpendicular to the field. Combining these behaviors together gives rise to a hysteresis loop with jumps which can be customized in several ways. The level of anisotropy will control the field at which the jumps will occur and the number of particles with a given level of anisotropy will control the size of the jump.

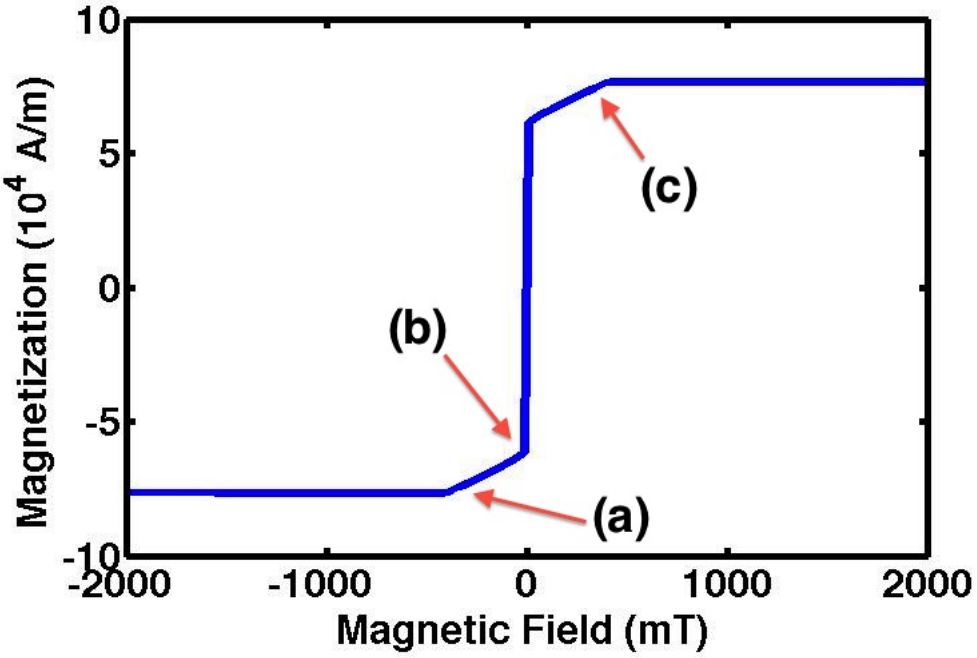

Figure 4.4: Hysteresis loop for two hemiellipsoids, one oblate and one prolate. As can be seen at the points labeled, there is slow divergence from the saturation as the prolate hemiellipsoid saturates perpendicular to the field (a), the oblate hemiellipsoid has uniform flipping (b), and finally the prolate hemiellipsoid saturates again (c).

A trivial example of this is shown in the case of having two hemiellipsoids of rotation where the major axis is equal to 20 nm and the minor axis is equal to 5 nm. For one of the hemiellipsoids, it is rotated about the major axis and for the other ellipsoid, it is rotated about the minor axis, allowing one to be prolate and the other oblate. This will give rise to a hysteresis behavior given shown in Fig. (4.4). As can be seen, there is a slow divergence from saturation as the prolate hemiellipsoid begins to saturate perpendicular to the field (a), followed by the avalanche flipping of the oblate hemiellipsoid (b), and finished with a slow saturation of the prolate hemiellipsoid (c).

4.7 Conclusions

There are many different cases where having a numerical value for a demagnetizing factor for a certain geometry is very important, such as for calculating the demagnetizing energy. The method presented above is a general method for obtaining a numerical value for the demagnetizing factor of any arbitrary geometry. This method is verified against the calculation of the demagnetizing factor of a hemisphere analytically.

Bibliography

[1] Aharoni, A.: 1998, *Journal of Applied Physics* **83(6)**, 3432

[2] Beleggia, M. and Graef, M. D.: 2003, *Journal of Magnetism and Magnetic Materials* **263(12)**, L1

[3] Beleggia, M., Graef, M. D., Millev, Y. T., Goode, D. A., and Rowlands, G.: 2005, *Journal of Physics D: Applied Physics* **38(18)**, 3333

[4] Beleggia, M., Vokoun, D., and Graef, M. D.: 2009, *Journal of Magnetism and Magnetic Materials* **321(9)**, 1306

[5] Brown, W. F.: 1962, *Magnetostatic Principles in Ferromagnetism*, North-Holland

[6] Brown Jr, W. F.: 1978, *Micromagnetics*, Krieger, New York

[7] Chen, D.-X., Brug, J., and Goldfarb, R.: 1991, *Magnetics, IEEE Transactions on* **27(4)**, 3601

[8] Donahue, M. and Porter, D.: 1999, *OOMMF User's Guide, Version 1.2a*, Interagency Report NISTIR 6376

[9] Geschwind, S. and Clogston, A. M.: 1957, *Phys. Rev.* **108**, 49

[10] Johnson, P., Gangopadhyay, A. K., Kalyanaraman, R., and Nussinov, Z.: 2012, *Submitted to Phys. Rev. B*

[11] Joseph, R. I.: 1976, *Geophysics* **41(5)**, 1052

[12] Krishna, H., Gangopadhyay, A., Strader, J., and Kalyanaraman, R.: 2011, *Journal of Magnetism and Magnetic Materials* **323(34)**, 356

[13] Krishna, H., Miller, C., Longstreth-Spoor, L., Nussinov, Z., Gangopadhyay, A. K., and Kalyanaraman, R.: 2008, *Journal of Applied Physics* **103(7)**, 073902

[14] Maxwell, J. C.: 1873, *A Treatise on Electricity and Magnetism*, Vol. 2, Oxford: Clarendon Press

[15] Osborn, J. A.: 1945, *Phys. Rev.* **67**, 351

[16] Ratti, G. and Robotti, G.: 1969, *Pure and Applied Geophysics* **75**, 5, 10.1007/BF00875037

[17] Rowland, H. A.: 1873, *Philosophical Magazine Series 4* **46(304)**, 140

[18] Stoner, E. C.: 1945, *Philosophical Magazine Series 7* **36(263)**, 803

[19] Tandon, S., Beleggia, M., Zhu, Y., and Graef, M. D.: 2004a, *Journal of Magnetism and Magnetic Materials* **271(1)**, 9

[20] Tandon, S., Beleggia, M., Zhu, Y., and Graef, M. D.: 2004b, *Journal of Magnetism and Magnetic Materials* **271(1)**, 27

[21] Thompson, W.: 1872, *Reprints of Papers on Electrostatics and Magnetism*, London:Macmillan

Chapter 5

Demagnetization Borne Microscale Skyrmions

5.1 Introduction

A skyrmion, theorized first by Skyrme in 1962 (24), is a state with a vectorial order parameter which is aligned at the system boundary at an opposite direction to what the order parameter assumes at the origin. Skyrmions may appear in diverse arenas, such as elementary particles (24; 2; 11; 5; 26), liquid crystals (27), Bose-Einstein condensates (13; 20; 28), thin magnetic films (15), quantum Hall systems (25; 6; 21; 3), and potentially vortex lattices in type II superconductors (1; 4). Being able to experimentally observe or generate skyrmions is a current research thrust (24; 24; 2; 11; 5; 26; 27; 13; 20; 28; 15; 25; 6; 21; 3; 1; 4; 19; 22; 14).

In the arena of magnetic systems that we will focus on in this work, earlier works

examined large scale skyrmions (9) including large scale textures in patterned vortices as in, e.g., the last figure of Kisielewski et al. (16)(where interesting textures are seen in the figure yet not noted to be skyrmionic). These earlier works did not focus on the ubiqutuous role of demagnetization energy in creating skyrmions nor examined the topological character of such created states. The effect that we advance in this work constitutes a general way of generating skyrmions. Skyrmions may be simply generated *by merely applying a field*. This way of creating skyrmions is far simpler than considerations presented in other recent works.

In this work we demonstrate via micromagnetic simulations that achieving a skyrmion is as simple as creating a nanoparticle of many possible geometries, which is large enough to support a single vortex but small enough to prevent multiple vortices. The demagnetization energy allows for the formation of a vortex at zero-field. We find that as the field increases such that it lies in a direction opposite to the core, the magnetization at the edges may realign itself parallel to the field direction more readily than the magnetization next to the core. Immediately prior to annihilation of the vortex (i.e., the flipping of the magnetization at the system core to become parallel to the applied field direction), the skyrmionic state is most notable. We observed this, relatively ubiquitous, effect in systems with disparate geometries- spheres, hemispheres, ellipsoids, and hemi-ellipsoids. It may be possible to generalize this process so as to experimentally synthesize a skyrmion lattice by simply creating an array of nanoparticles with tunable size and spacing, such as by self-organzation (18; 17). Preliminary simulations of a two-by-two grid of Cobalt hemispheres of radius 20 nm

with varying inter-hemisphere separation indicate that beyond a threshold distance of twice the radius, an array of skyrmions is formed. As the center to center separation is steadily increased, the skyrmionic state becomes more lucid. For small separations, interactions partially thwart the creation of the individual skyrmions.

As is well known, we can quantify a skyrmionic state by calculating the Pontryagin index (also known as a winding number) that is given by (10)

$$Q = \frac{1}{8\pi} \int d^2x \epsilon_{ij} \hat{M} \cdot (\partial_i \hat{M} \times \partial_j \hat{M}). \tag{5.1}$$

In this expression, ϵ_{ij} is the two dimensional anti-symmetric tensor and $\hat{M}$ is the normalized magnetization. For a single skyrmion, this winding number (or topological charge) is equal to unity. Skyrmions are characterized by the non-trivial homotopy class $\pi_2(S^2)$. This homotopy class is characterized by an integer that, for this case, is the Pontryagin index. States with different integer skyrmion number (the Pontryagin index) cannot be continuously deformed into one another.

In the current context, the skyrmionic state resides on a two dimensional plane. On each spatial point of the plane, there is a three dimensional order parameter which, in our case, is the magnetization $\vec{M}$. Topologically, a skyrmion is a magnetic state such that when it is mapped onto a sphere (via stereographic projection) resembles a monopole or hairy ball. This means that on mapping from a flat space to the surface of a sphere, the individual magnetic moments will always point perpendicular to the

surface of the sphere, much like a magnetic monopole.

The above topological classification is valid for an "ideal" skyrmion on an infinite two-dimensional plane or disk with the condition that the local moment $\vec{M}(\vec{r})$ at spatial infinity (irrespective of the location $\vec{r}$ on the infinite disk) all orient in the same direction: $\lim_{r\to\infty} \hat{M}(\vec{r}) = \hat{M}_0$. In such a case $\hat{M}_0$ corresponds to the magnetization at the "point at infinity". On applying a stereographic projection of the infinite plane onto a unit sphere, $\hat{M}_0$ maps onto the magnetization at the north pole of the unit sphere while the oppositely oriented $\hat{M}$ at the origin corresponds to the magnetization at the south pole. In such a case, the winding number is identically equal (in absolute value) to unity. In many physically pertinent geometries, including the systems simulated in this work, there are finite size limits which only allow the magnetization $\vec{M}$ to exhibit the trend of approaching a uniform value $\vec{M}_0$ as one moves away from the center of the system. In this case, the integral in Eq. 5.1 is not an integer. However, it is clear that, in the limit of infinite planar size, these states would become ideal skyrmions and the winding number Q would approach an integer value.

The remainder of this article is organized as follows. In Section 5.2, we provide necessary background. We briefly describe the simulations employed in this work and discuss energetic considerations. Section 5.3 reports on our central result—the numerical observation of skyrmions. We discuss a higher dimensional generalization and the possibility of generating skyrmion lattices. We conclude in section 5.4 with a summary of our results.

5.2 Theory

5.2.1 Simulation Theory

In this work of simulating magnetic states of nanoparticles, the Object Oriented Micromagnetic Framework (OOMMF) 1.2a distribution as provided from NIST was utilized (8). The OOMMF code numerically solves the Landau-Lifshitz Ordinary Differential Equation given by,

$$\frac{d\vec{M}}{dt} = -|\bar{\gamma}|\vec{M} \times \vec{H}_{eff} - \frac{|\bar{\gamma}|\tilde{\alpha}}{M_s}\vec{M} \times \left(\vec{M} \times \vec{H}_{eff}\right) \tag{5.2}$$

where $\vec{M}$ is the magnetization, $\bar{\gamma}$ is the Landau-Lifshitz gyromagnetic ratio, M_s is the saturation magnetization, $\tilde{\alpha}$ is the damping coefficient, and H_{eff} is the effective field given by derivatives of the Gibbs free energy. The Gibbs free energy, in this case, is given by (7),

$$G = \int \left(\frac{1}{2}C\left[\left(\vec{\nabla}\alpha\right)^2 + \left(\vec{\nabla}\beta\right)^2 + \left(\vec{\nabla}\gamma\right)^2\right] + w_a - \frac{1}{2}\vec{M} \cdot \vec{H}' - \vec{M} \cdot \vec{H}_0\right) dV \tag{5.3}$$

where α, β, and γ are the directional cosines, C is proportional to the exchange stiffness constant and depends on the crystal structure, w_a is the crystalline anisotropy term, $\vec{H}'$ is the demagnetization field, and $\vec{H}_0$ is the external magnetic field. The

crystalline anisotropy term can be expressed in terms of anisotropy constants, K_1 and K_2, and directional cosines as,

$$w_a = K_1 \left(\alpha^2\beta^2 + \beta^2\gamma^2 + \gamma^2\alpha^2\right) + K_2\alpha^2\beta^2\gamma^2. \tag{5.4}$$

In the simulations, a metastable state was determined to have been reached when the maximum torque experienced by any one magnetic moment, measured in $\frac{degrees}{ns}$, dropped below 0.2. Once this level of torque was reached, the magnetic state data were saved to a file along with the other properties of the system, including but not limited to, the energies associated with each contribution, overall magnetization, and number of iterations. The magnetic field was then changed to the next value and the iterations continued until saturation of the magnetization was obtained. The magnetic field steps were chosen such that half the steps (typically, a few hundred) were during the increasing field portion and the other half in the decreasing field portion. The data stored in the file were used later to generate the hysteresis plots, track the energy changes associated with the field variations, and the spatial orientations of the magnetic moments. Unless specified otherwise, the parameters chosen in the simulations correspond to those for Cobalt, as shown in Table (5.1).

parameter	value used in this work
Exchange Stiffness Constant (A)	$2.5 \times 10^{-11} \frac{J}{m}$
Saturation Magnetization (M_s)	$1.4 \times 10^{6} \frac{A}{m}$
Damping Constant ($\tilde{\alpha}$)	0.5
Landau-Lifshitz Gyromagnetic Ratio ($\bar{\gamma}$)	$2.21 \times 10^{5} \frac{m}{A \cdot s}$
Stopping Torque ($\frac{dm}{dt}$)	$0.19 \frac{deg}{ns}$

Table 5.1: Table of parameters used in the simulations of particles in this work. The exchange stiffness constant, saturation magnetization, and crystalline anisotropy constant are material specific and are chosen for Cobalt. The damping constant, Landau-Lifshitz-Giblert gyromagnetic ratio, and stopping torque are material independent parameters.

5.2.2 Energy Considerations

In our simulations, we considered field, demagnetization, and exchange energies. For simplicity, we neglected crystalline anisotropy effects. The field tries to align the local magnetic moments parallel to it while exchange effects favor an alignment of the magnetic moments with their nearest neighbors. The (universally geometry borne) demagnetization energy directly relates to dipole-dipole interactions (7). Demagnetization energy is often the dominant term for long range behaviors while exchange effects tend to dominate at short spatial scales.

As is well known, the competition between the long range and the short range energy contributions leads to the creation of domain walls. The demagnetization favors oppositely oriented moments at the expense of exchange effects that favor slow variations amongst neighbors. Ultimately, this tradeoff gives rise to domain walls in micromagnetic systems.

The potential energy from demagnetization of a system is given by

$$\mathcal{E}_M = -\frac{1}{2}\sum_i \vec{m}_i \cdot \vec{h}'_i, \tag{5.5}$$

where $\vec{h}'_i$ is the effective field at position i that originates from all other dipoles. This field can be written as

$$\vec{h}'_i = \vec{H}' + \frac{4}{3}\pi\vec{M} + \vec{h}''_i, \tag{5.6}$$

where $\vec{H}'$ is the megascopic field from the poles due to $\vec{M}$ outside of a physically small sphere around site i. The second term subtracts the effective field inside an arbitrary small region (or sphere) centered about point i, and $\vec{h}''_i$ is the field at site i created by dipoles inside this region. In general, $\vec{h}''_i$ depends on the crystal lattice structure. In the continuum limit, the sum becomes an integral of the form,

$$\mathcal{E}_M = -\frac{1}{2}\int \vec{M} \cdot (\vec{H}' + \frac{4}{3}\pi\vec{M} + \Lambda \cdot \vec{M})dV. \tag{5.7}$$

The tensor Λ in the third term depends only on the crystal structure and local magnetization and can grouped with crystalline anisotropy. This tensor also vanishes for cubic crystals identically. The second term in this expression is a constant proportional to M_s^2 and can be ignored leaving,

$$\mathcal{E}_M = -\frac{1}{2}\int \vec{M}\cdot\vec{H}' dV. \tag{5.8}$$

The demagnetization field, $\vec{H}'$, can equivalently be derived from Maxwell's equations. It can be expressed as the negative gradient of a potential, U that satisfies the equations,

$$\nabla^2 U_{in} = \gamma_B \vec{\nabla}\cdot\vec{M} \tag{5.9}$$

$$\nabla^2 U_{out} = 0, \tag{5.10}$$

with the surface boundary conditions,

$$U_{in} = U_{out} \tag{5.11}$$

$$\frac{\partial U_{in}}{\partial n} - \frac{\partial U_{out}}{\partial n} = \gamma_B \vec{M}\cdot\vec{n}. \tag{5.12}$$

where the constant γ_B is, in our units, 4π.

Lastly, the potential needs to be regular at infinity, such that $|rU|$ and $|r^2U|$ are bounded as $r \to \infty$. Our simulations directly capture the demagnetization field effects.

From the standpoint of energy, for a skyrmion to be possible, the dimensions of the

ellipsoid must be larger than the critical dimensions at which vortices can nucleate in a given system. For example, for the hemispherical geometry, with the typical values of Table 5.1, the critical radius was found to be $19\,nm$. For larger radii, vortices are the preferred state before reaching zero field. The vortex will nucleate such that the core is parallel to the field and the remainder of the vortex lies in the plane perpendicular to the field. Once the field begins to oppose the direction of the moments at the core, the energy cost of eliminating the core is significantly higher than allowing the outer magnetic moments to align more with the field. When the exchange energy cost of the skyrmionic state becomes greater than the demagnetization energy for a uniform magnetization, the core flips, annihilating the skyrmion, and the magnetization saturates. Immediately, prior to this, though, a skyrmionic state can be achieved.

Ezawa (9) raised the specter of a skyrmionic state in thin films via the computation of the energy of such assumed variational states within a field theoretic framework of a non-linear sigma model. Dipole-dipole interactions may stabilize such a state below a critical field. Our exact numerical calculations for the evolution of the magnetic states demonstrate that not only are skyrmionic states viable structures, but are actually the precise lowest energy state for slices of hemispheres and other general structures.

5.3 Results and Discussion

5.3.1 Observation of a Skyrmion

As our numerical simulations vividly illustrate, just prior to the annihilation of the vortex, the magnetic moments at the edge of the system start to orient themselves in a direction opposite to that in the core. On increasing the radius of the simulated hemispheres and spheres, the configurations next to the basal plane better conformed to the full skyrmion topology (i.e., that on an infinite plane). It should be noted here, that as the radius of a hemisphere increases, the crossover to a double vortex state will eventually occur, but if one vortex is maintained, in the limit of large radii, a full skyrmion would be expected. This may be possible in materials with large exchange constant and small saturation magnetization. In what follows, we will employ the typical values appearing in Table (5.1). The skyrmion state for the bottom layer (basal plane) of a hemisphere of radius $24\,nm$ is shown in Fig. (5.1).

A similar configuration was observed in simulation runs for nanospheres. For a sphere, symmetry does not favor any particular direction, but that symmetry is broken once a field is applied. Skyrmions were observed in runs of spheres large enough to support a vortex which corresponds to a radius of $\approx 15\,nm$. As the radius of the sphere increases, the edge magnetic moments and the core magnetic moments become more antiparallel. A skyrmion in a sphere of radius $59nm$ is shown in Fig. (5.2).

Once skyrmions were observed in these systems, it begged the question, "Do these

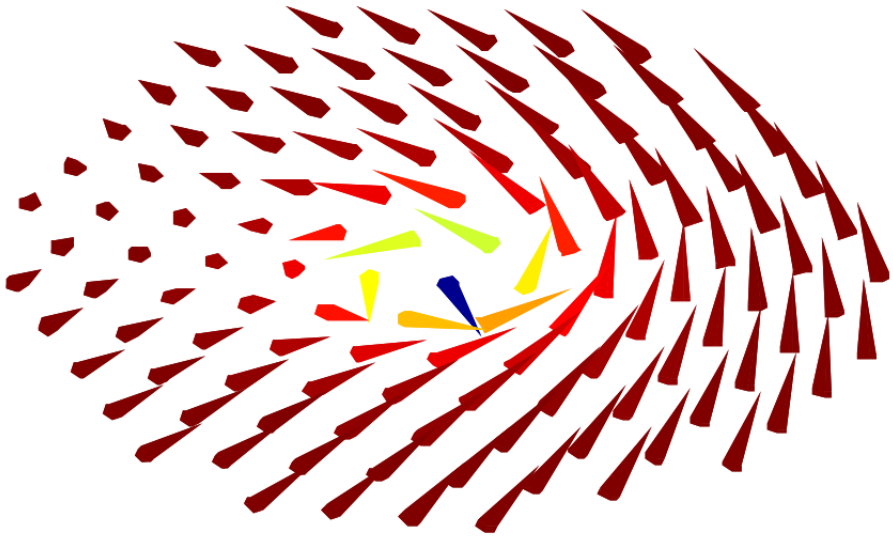

Figure 5.1: Vector plot of the skyrmion state for the bottom slice of a hemisphere of radius 24 nm. Not all local magnetic moments are shown for the sake of clarity.

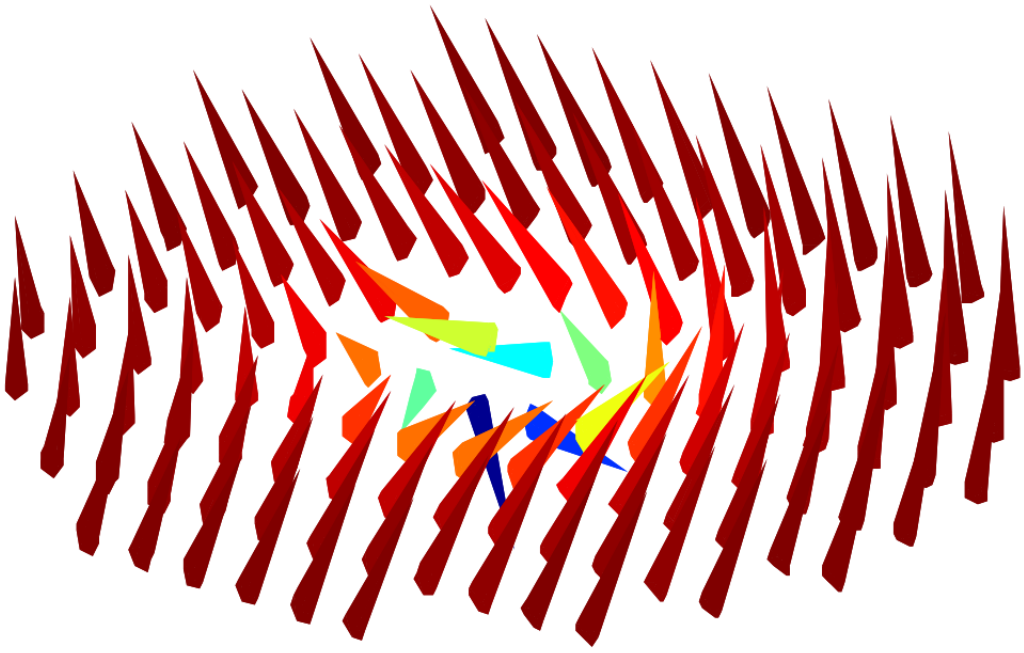

Figure 5.2: Vector plot of the skyrmion state in a sphere of radius 59nm. The slice is along the equator of the sphere. Only a subset of local magnetic moments is shown for clarity.

occur in ellipsoids and hemi-ellipsoids?" Upon examining this, indeed skyrmions can be observed in oblate ellipsoids and hemi-ellipsoids as shown in Figs. (5.3, 5.4).

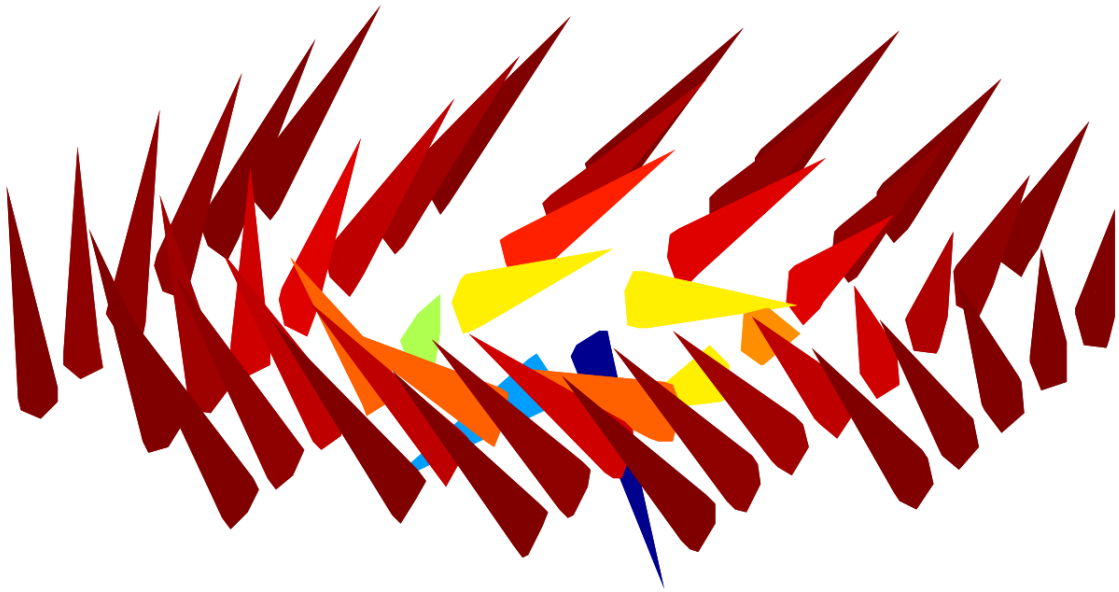

Figure 5.3: Vector plot of the skyrmion state in an ellipsoid with major axis of $20\,nm$ and minor axis of $15\,nm$. The slice is along the equator of the ellipsoid. Only a subset of local magnetic moments is shown for clarity.

To verify that these are structures approach those of skyrmions and to quantitively monitor their deviations from an ideal skyrmionic state (for which the Pontryfin index is unity),we computed the Pontryagin index at different cross sections of the hemisphere in an attempt to determine how close to an ideal skyrmion these states are. These cross sections were those of the hemisphere with planes parallel to the basal plane(i.e., that at the base of the hemisphere). For a hemisphere with radius $30\,nm$, we calculated the skyrmion number Q for thirty individual parallel layers vertically separated by $1\,nm$. We numerically evaluated the integral of Eq. (5.1) for all of these layers and examined how it changes as the field increases from 0 to $0.6\,T$.

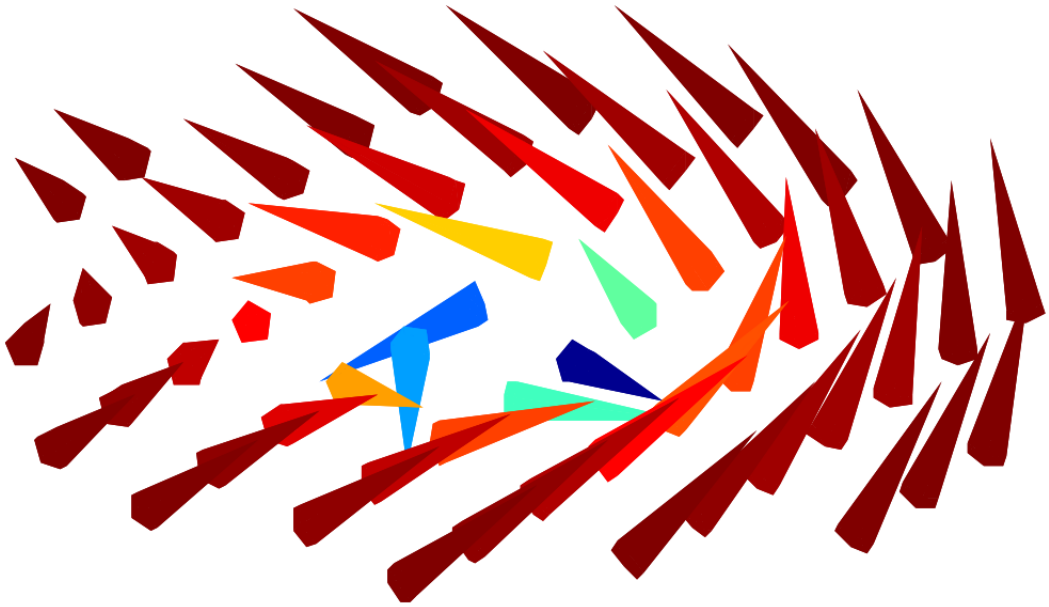

Figure 5.4: Vector plot of the skyrmion state in a hemi-ellipsoid with major axis of $20nm$ and minor axis of $15\,nm$. The slice is along the base of the hemi-ellipsoid. Only a subset of local magnetic moments is shown for clarity.

These data are shown in Fig. (5.5).

Visualizing this in the geometry of the hemisphere specifically, one can look at how the Pontryagin index varies along various planes of a hemisphere, starting from the equator and moving to the pole. It can be clearly seen that the skyrmionic behavior exists for most of the height of the hemisphere and only the cap deviates from the rest of the system. The size of this cap depends on the given field strength as can be seen in the case of 0 field (Fig. (5.6(a))) and with a field of $0.6\,T$ (Fig. (5.6(b))). At higher fields, prior to the annihilation of the vortex, the Pontryagin index approaches an integer value, as expected for an ideal skyrmionic state.

Performing similar analysis on the hemi-ellipsoids and visualizing the Pontryagin index and its variance with height, it can be seen that the same behavior exists in a

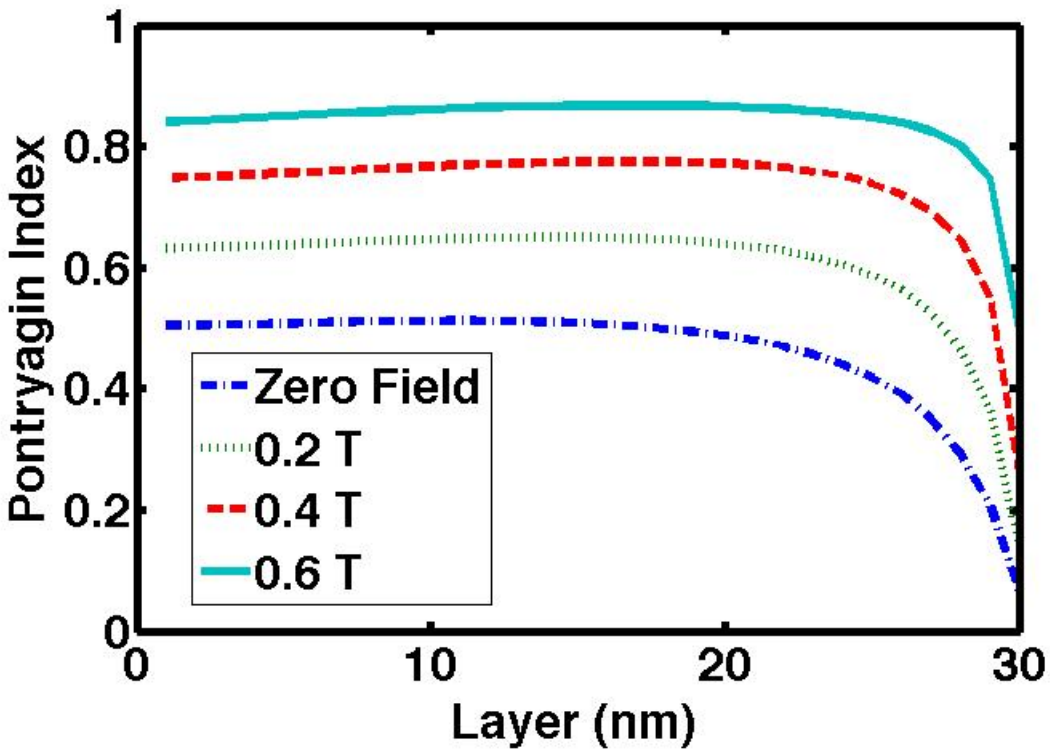

Figure 5.5: Plot of the Pontryagin index versus the z-coordinate of the slice taken from the hemisphere of radius $30\,nm$. These are shown for increasing field from zero field (dark blue dot-dash line), $0.2\,T$ (green dotted line), $0.4\,T$ (red dashed line), and $0.6\,T$ (teal solid line).

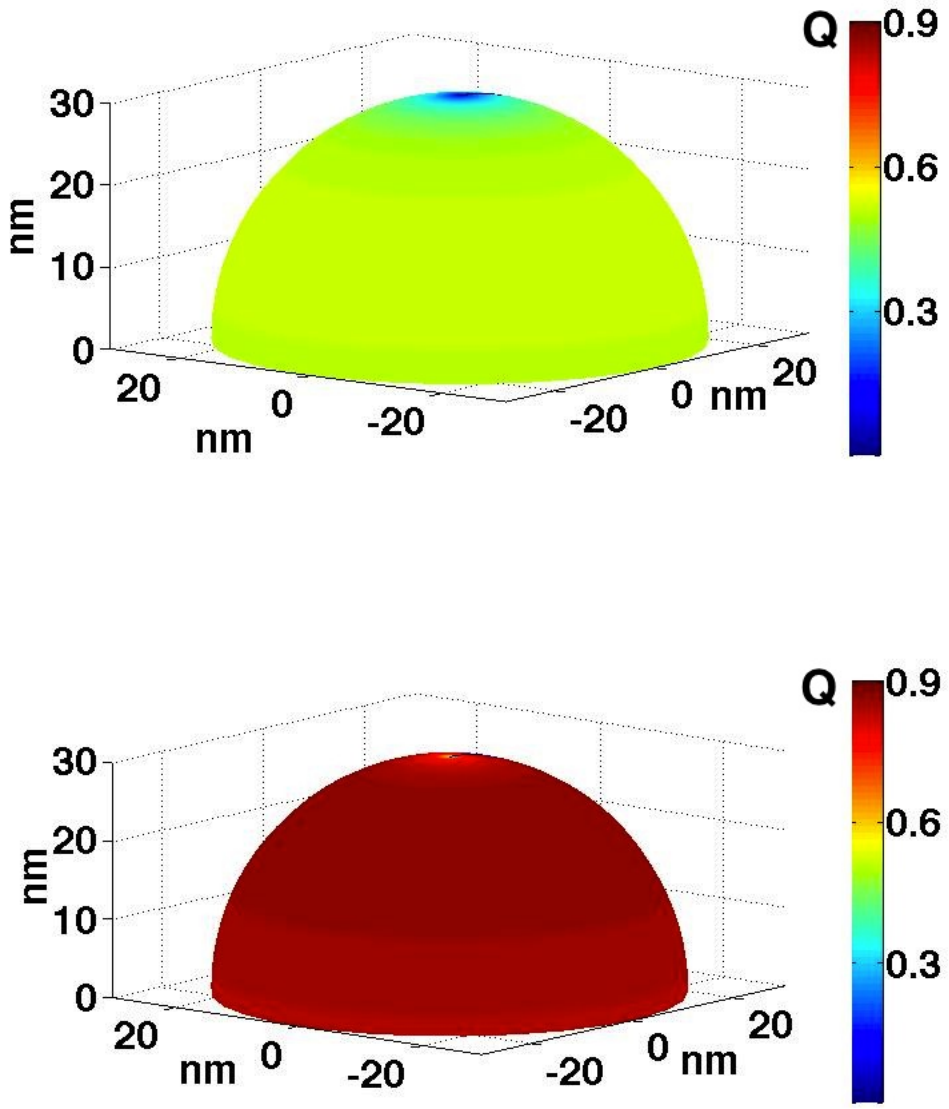

Figure 5.6: Three dimensional plots of the Pontryagin index for a hemisphere of radius $30\,nm$ at (a) zero field and (b) $0.6\,T$

less extreme way than the hemispheres. This behavior can be seen in Fig. (5.9) for hemi-ellipsoids of fixed 30 nm major axis and varying minor axis.

In examining the hysteresis behavior of the hemi-ellipsoids, one can see a trend as the z-dimension goes from the hemisphere radius (20 nm) to the minimum simulated size of 5 nm. This trend shows a movement from extensive vortex and skyrmionic behavior in the more hemispheric geometries and less vortex and skyrmionic behavior in the more ellipsoidal geometries.

Although it will not be considered in this work, crystalline anisotropy could influence the formation of skyrmions in a number of ways. In the case of a single crystal, the vortex state would be more difficult to nucleate and thus the skyrmionic state is less energetically favorable. When many crystalline grains are present, the results discussed here are valid as the large number or randomly oriented crystals will, on average, not favor any direction, and thus will not favor any one direction.

5.3.2 Generalization to a Hedgehog

These results lead to the question of whether this can be generalized to more than two dimensions. The natural generalization from the two-dimensional skyrmion to a three-dimensional magnetic state would be the hedgehog. The hedgehog resides in three spatial dimensions coupled with a three dimensional order parameter. The canonical example of a hedgehog is$\vec{M} = M_s\hat{r}$ where the magnetization always points outwards. A skyrmion is related to a hedgehog via a stereographic projection from the sphere onto a plane where the south pole of the hedgehog projects to the core of

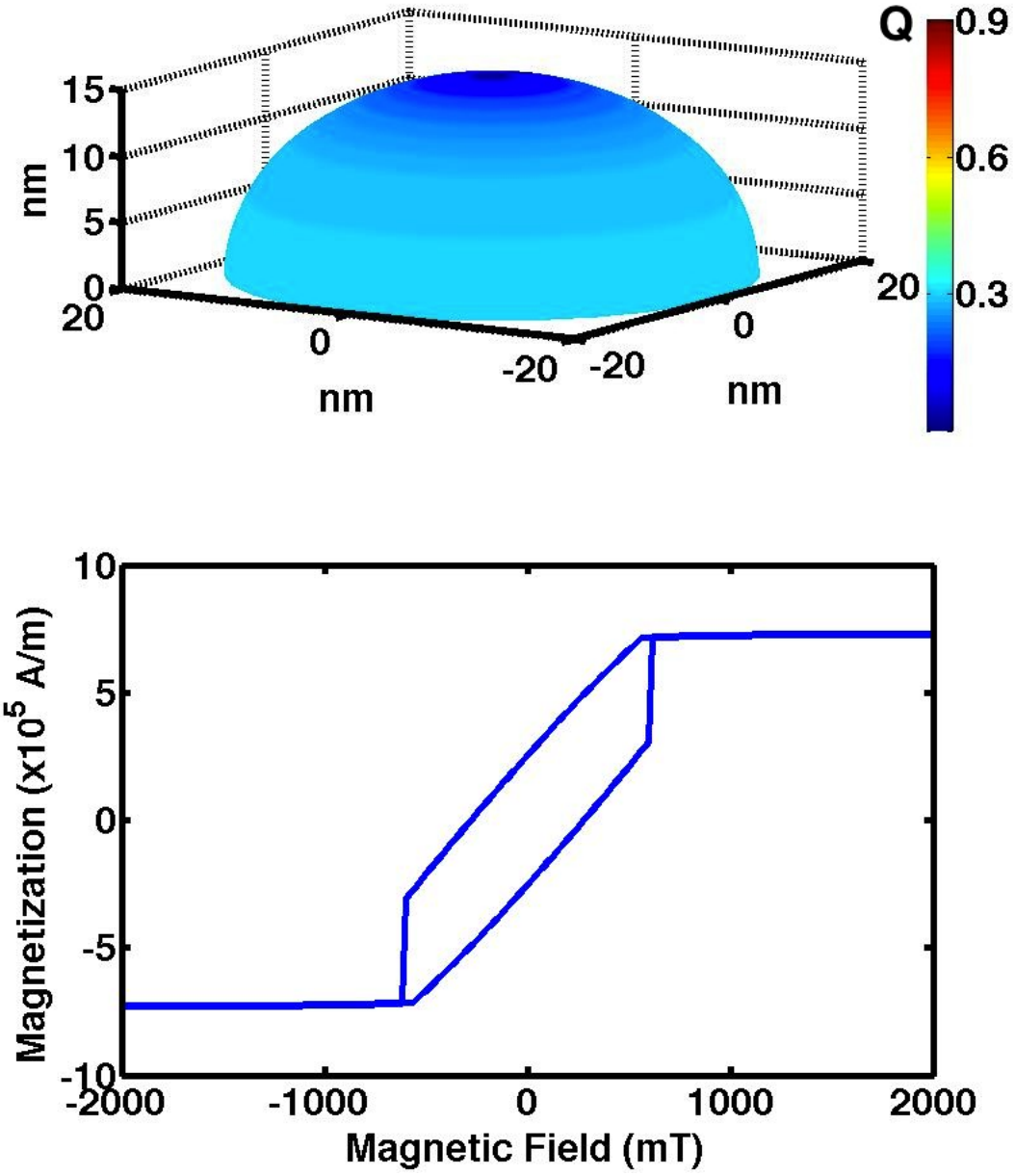

Figure 5.7: Plot of the Pontryagin index and how it varies with height inside hemi-ellipsoids of 30 nm radius major axis and the minor axis is 15 nm. This is shown for a field equal to 0.2 T pointing in the negative z-direction (perpendicular to the face of the hemi-ellipsoids). As will be noted, the existence of skyrmionic behavior is not prevalent in the more flattened hemiellipsoinds and vanishes at this field between minor axis 15 nm and 10 nm. The associated partial hysteresis loops for each of these hemi-ellipsoid runs are shown in Fig (b).

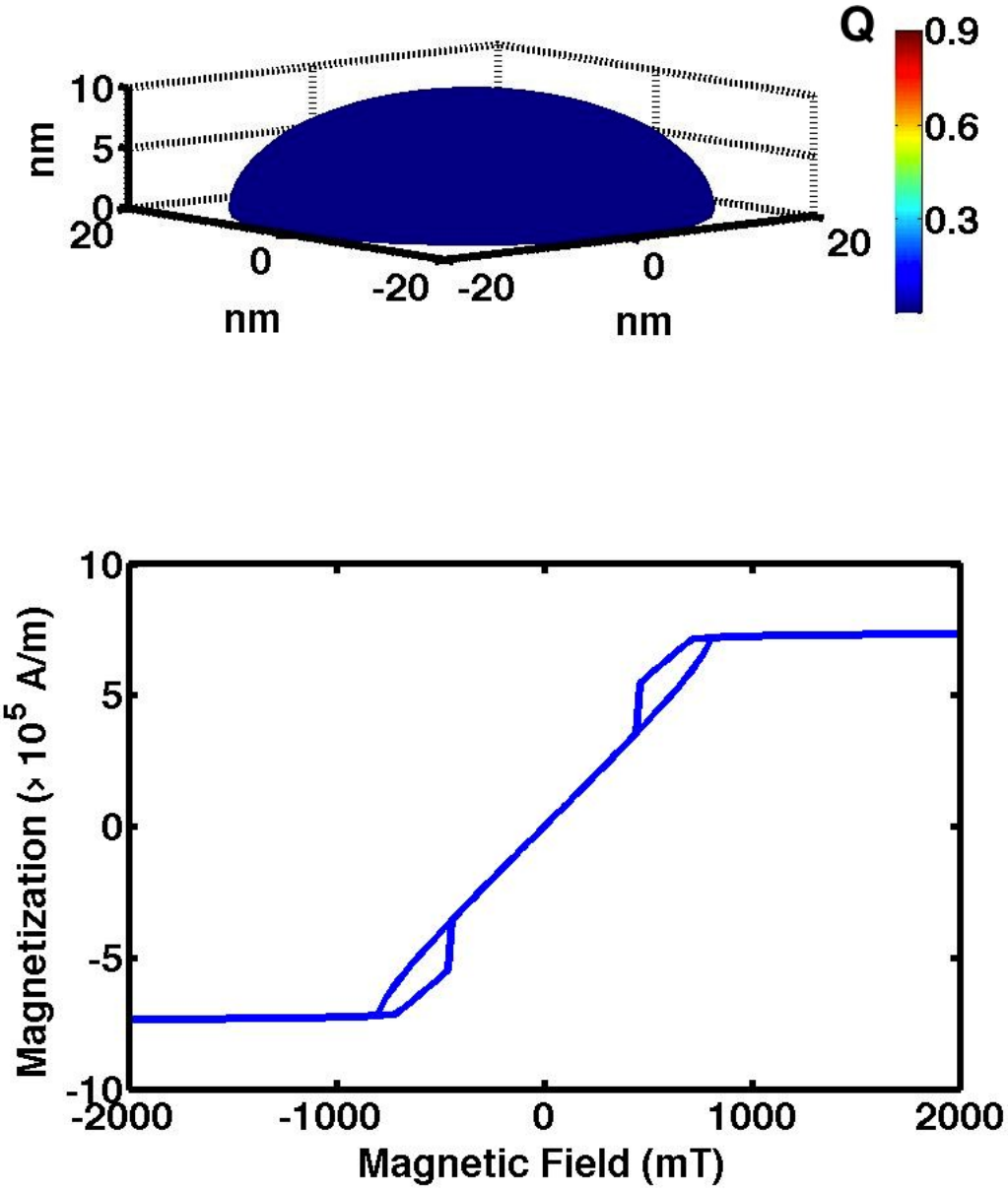

Figure 5.8: Plot of the Pontryagin index and how it varies with height inside hemi-ellipsoids of 30 nm radius major axis and the minor axis of 10 nm (a). This is shown for a field equal to 0.2 T pointing in the negative z-direction (perpendicular to the face of the hemi-ellipsoids). As will be noted, the existence of skyrmionic behavior is not prevalent in the more flattened hemiellipsoinds and vanishes at this field between minor axis 15 nm and 10 nm. The associated partial hysteresis loops for each of these hemi-ellipsoid runs are shown in Fig (b).

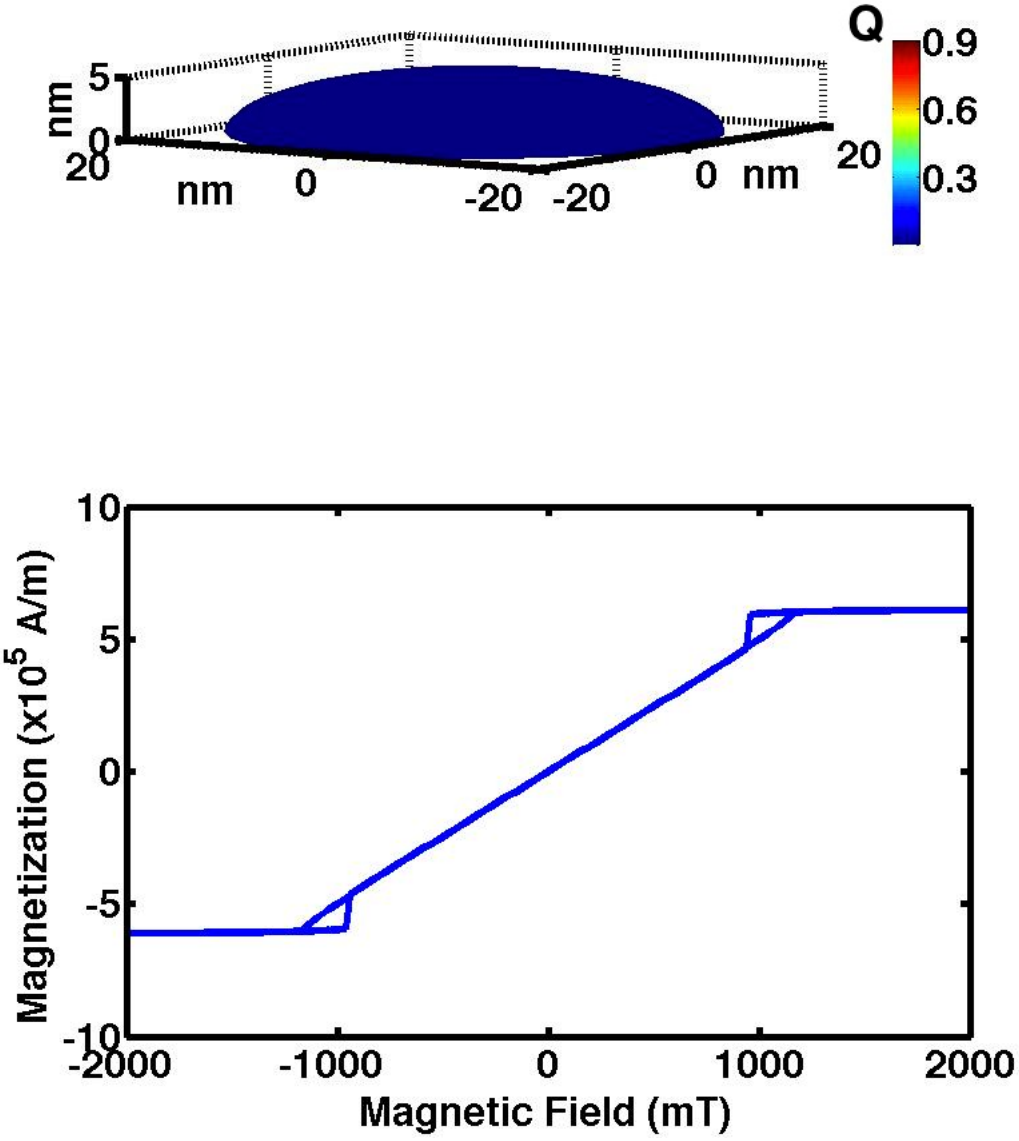

Figure 5.9: Plot of the Pontryagin index and how it varies with height inside hemi-ellipsoids of 30 nm radius major axis and the minor axis of 5 nm (a). This is shown for a field equal to 0.2 T pointing in the negative z-direction (perpendicular to the face of the hemi-ellipsoids). As will be noted, the existence of skyrmionic behavior is not prevalent in the more flattened hemiellipsoinds and vanishes at this field between minor axis 15 nm and 10 nm. The associated partial hysteresis loops for each of these hemi-ellipsoid runs are shown in Fig (b).

the skyrmion on the plane and the north pole of the hedgehog projects to the points at infinity on the plane. Calculating the demagnetizing field for this state in a sphere gives rise to a potential and field equal to

$$U(r) = \gamma_B M_s (r - R), \tag{5.13}$$

$$\vec{H} = -\gamma_B M_s \hat{r}, \tag{5.14}$$

where r is the radial coordinate and R is the radius of the hedgehog.

Plugging this into Eq. (5.8), one finds the energy of the hedgehog to be $2\pi M_s^2 (4\pi/3) R^3$. Comparing this to the energy of the uniformly magnetized state, $(1/2)(4\pi/3)^2 M_s^2 R^3$, it can easily be seen that the hedgehog has three times the energy of the uniform state. This, combined with the fact that the exchange energy and the field energy will favor the uniform state, the hedgehog state will not be possible in a sphere.

If one were to continuously deform the hedgehog by rotating the local magnetic moments by $\pi/2$ such that $\vec{M} = M_s f(z)\hat{\phi}$ where $f(z)$ is a function that goes to 0 as $z \to 0$ such that the exchange energy does not diverge, one would find the demagnetization energy of that state to be identically 0. The field energy in this system is also 0 for a field that is applied along the z-axis. The exchange energy is given by $(4\pi/3)RC$ where C is the exchange stiffness constant. The total energy of this state is equal to the exchange energy, and comparing this to the uniform state, a hedgehog of this form is favorable for,

$$R \geq \sqrt{\frac{C}{\frac{2\pi\mu_0 M^2}{3} - MH_0}}. \tag{5.15}$$

For $C = 2.5 \times 10^{-11} J/m$ and $M_s = 1.4 \times 10^6 A/m$ as it is for Cobalt, at 0 field, this radius works out to be $\approx 3.5 \mu m$.

5.3.3 Skyrmion Array

It is illuminating to consider the possibility of an array of skyrmions. As briefly discussed below, we find that effective particle interactions may thwart the creation of a skyrmion lattice when these particles are not far separated. However, for sufficiently large center to center separations, a Skryme lattice may be achieved. In preliminary simulations of arrays of nanoparticle arrays, simulations of a two-by-two grid of hemispheres of radius 20 nm with a variable separation show that a center to center separation of four times the radius is close enough that the nanoparticles still interact magnetically and prevent the formation of an array of skyrmions. As expected, further separation should approach the the single particle result of skyrmions, as we briefly discuss next.

The transition from the array of particles which support individual vortices to the array of particles that are clearly interacting with each other can be seen in Fig. (5.11). In this figure, the annihilation of the vortices can be seen as the particles realign their magnetization to form a state where the local magnetization orients

in the counterclockwise direction from particle to particle, yet within each particle, when moving in the counterclockwise direction, the local magnetization changes from oriented in the negative z-direction to the positive z-direction.

In repeating these simulations for a 3x3 array of hemispherical nanoparticles as shown in Fig. (5.12), the same behavior was observed. This array was similar to the 2x2 array in that it had nanoparticles with diameters of 40 nm and center to center separation of 80 nm. The annihilation of the vortices occurred at a slightly larger field (0.08T rather than 0.1T).

The stability of the skyrmion state depends on the separation distance between the nanoparticles. Existence of these states has been studied at a range of center-to-center separations spanning 50 nm to 200 nm, and the critical field at which the skyrmions are no longer energetically favorable is plotted versus the center-to-center separation in Fig. (5.10).

5.4 Conclusion

We conclude with a brief synopsis of our findings. We carried a systematic numerical study of the magnetization of small nanoparticles in the presence of an external magnetic field. These systems were simulated for different sizes and geometry (sphere, hemisphere, ellipsoids). Our analysis ignored anisotropy (crystalline, strain, etc.) effects. We find that, as has been widely reported in the literature (23; 12), beyond a critical diameter, the particles enter into a single vortex state under zero external field;

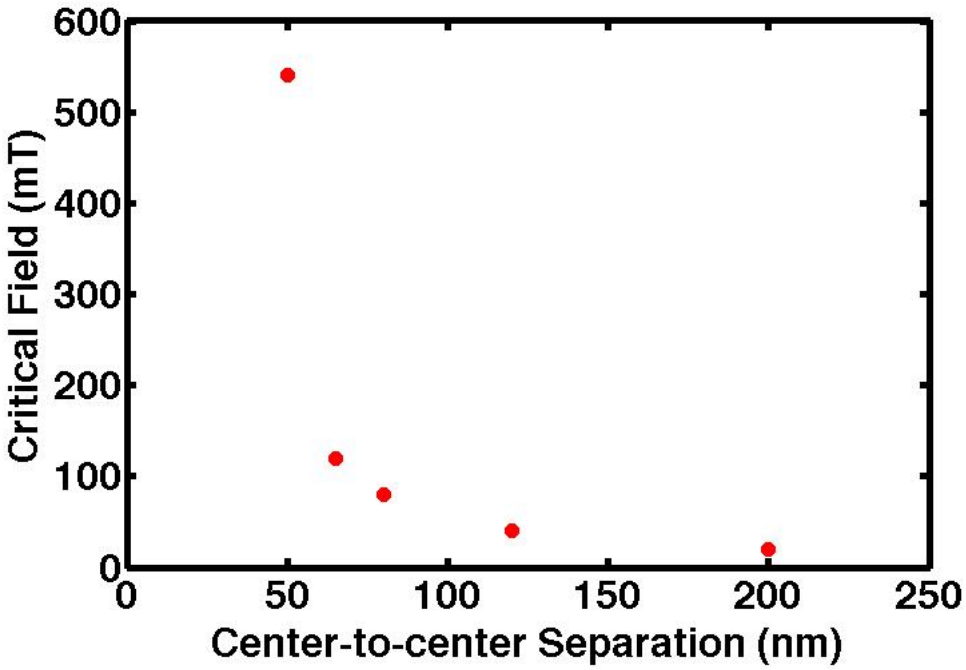

Figure 5.10: Plot of critical field at which skyrmions are no longer energetically favorable versus the center-to-center separation.

multiple vortices are possible for much larger particles. Our key new result concerns *the creation of skyrmions in the single vortex state*. As the field is increased, vortex annihilation is accompanied by the formation of a skyrmionic state wherein the magnetization of the vortex core points to a direction opposite to that at the edge of the nanoparticle. Our result illustrates how geometry plays a pivotal role. Spheres and hemispheres more readily achieve skyrmionic states than higher eccentricity ellipsoids. Our preliminary results suggested that for center to center separations larger than twice the particle diameters, an array of skyrmions may be realized. More detailed studies of skyrmion lattices for such particle arrays are planned for the future.

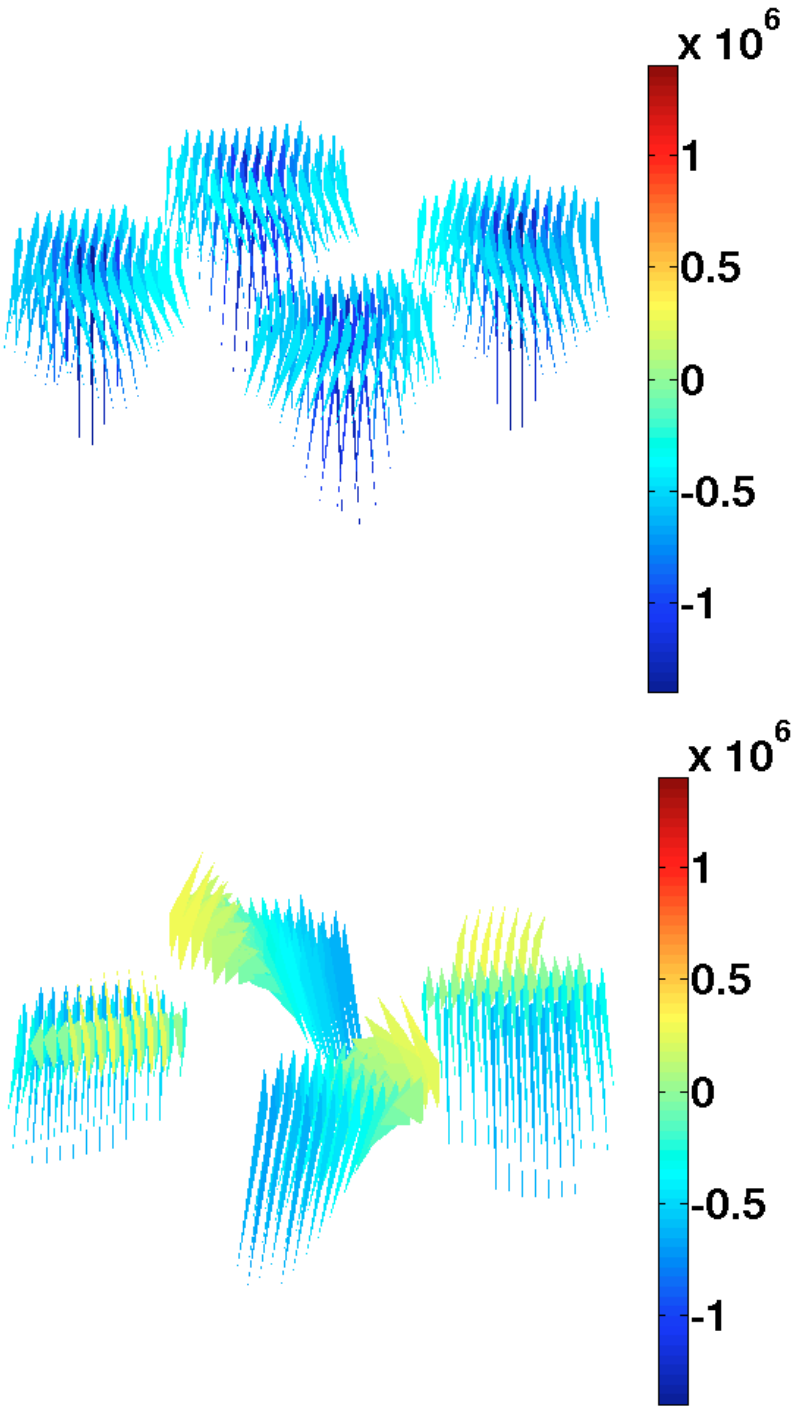

Figure 5.11: Vector plot of a 2x2 array of hemispheres with radius $20nm$ and center to center separation $80nm$ at fields of $0.12T$ pointing in the negative z-direction (a) and $0.1T$ pointing in the negative z-direction (b). Colorscale corresponds to z-component of the local magnetic moment in units of A/m.

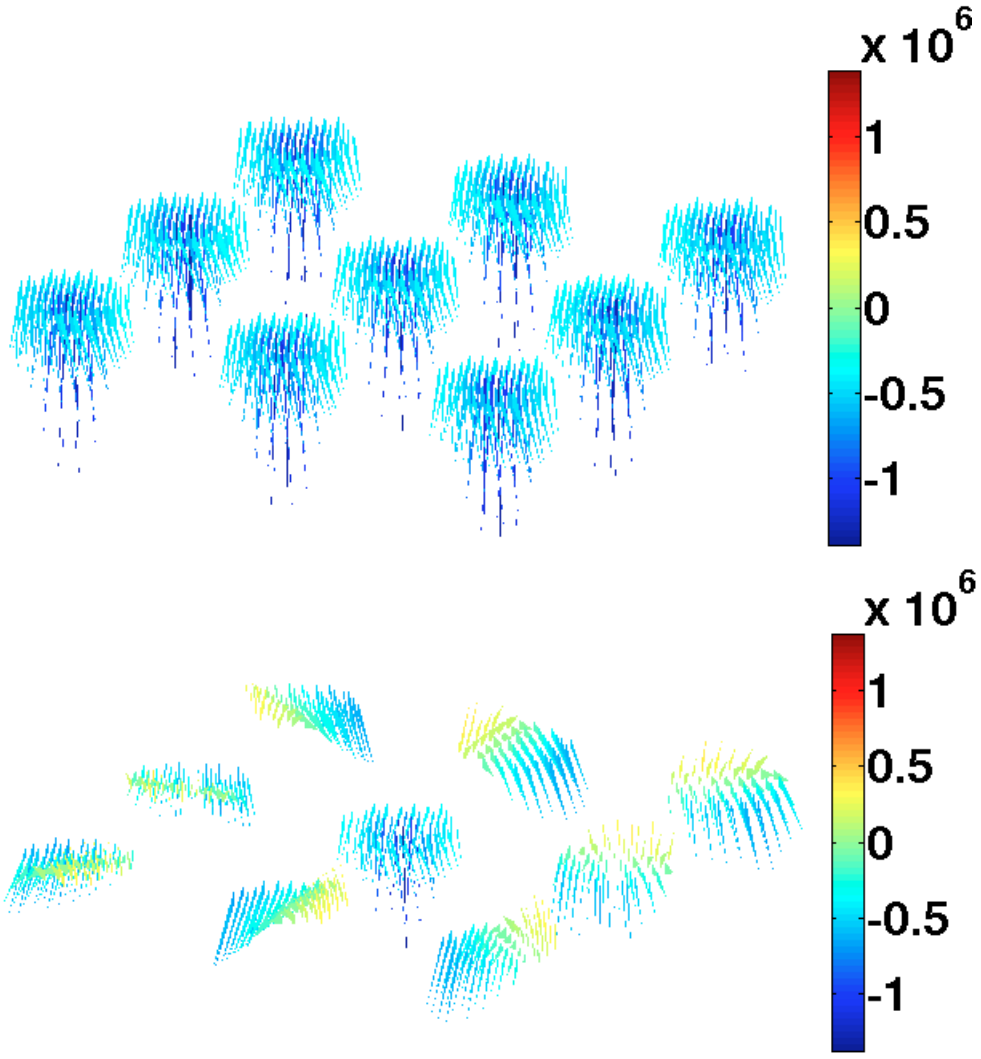

Figure 5.12: Vector plot of a 3x3 array of hemispheres with radius $20\,nm$ and center to center separation $80\,nm$ at fields of $0.1\,T$ pointing in the negative z-direction (a) and $0.08T$ pointing in the negative z-direction (b). Colorscale corresponds to z-component of the local magnetic moment in units of A/m.

Bibliography

[1] Abrikosov, A. A.: 2004, *Rev. Mod. Phys.* **76**, 975

[2] Atiyah, M. and Manton, N.: 1989, *Physics Letters B* **222(34)**, 438

[3] Barrett, S. E., Dabbagh, G., Pfeiffer, L. N., West, K. W., and Tycko, R.: 1995, *Phys. Rev. Lett.* **74**, 5112

[4] Baskaran, G.: 2011

[5] Battye, R. A. and Sutcliffe, P. M.: 1997, *Phys. Rev. Lett.* **79**, 363

[6] Brey, L., Fertig, H. A., Côté, R., and MacDonald, A. H.: 1995, *Phys. Rev. Lett.* **75**, 2562

[7] Brown Jr, W. F.: 1978, *Micromagnetics*, Krieger, New York

[8] Donahue, M. and Porter, D.: 1999, *OOMMF User's Guide, Version 1.2a*, Interagency Report NISTIR 6376

[9] Ezawa, M.: 2010, *Phys. Rev. Lett.* **105**, 197202

[10] Fradkin, E.: 1999, *Field Theories of Condensed Matter Systems*, Advanced Books Classics Series, Perseus Books

[11] Houghton, C. J., Manton, N. S., and Sutcliffe, P. M.: 1998, *Nuclear Physics B* **510(3)**, 507

[12] Hubert, A. and Schäfer, R.: 1998, *Magnetic domains: the analysis of magnetic microstructures*, Springer

[13] Khawaja, U. A. and Stoof, H.: 2001, *Nature* **411**, 918

[14] Kirakosyan, A. and Pokrovsky, V.: 2006, *Journal of Magnetism and Magnetic Materials* **305(2)**, 413

[15] Kiselev, N. S., Bogdanov, A. N., Schafer, R., and Rosler, U. K.: 2011, *Journal of Physics D: Applied Physics* **44(39)**, 392001

[16] Kisielewski, M., Maziewski, A., and Zablotskii, V.: 2006, *physica status solidi (c)* **3(1)**, 1

[17] Krishna, H., Gangopadhyay, A., Strader, J., and Kalyanaraman, R.: 2011, *Journal of Magnetism and Magnetic Materials* **323(34)**, 356

[18] Krishna, H., Miller, C., Longstreth-Spoor, L., Nussinov, Z., Gangopadhyay, A. K., and Kalyanaraman, R.: 2008, *Journal of Applied Physics* **103(7)**, 073902

[19] Leslie, L. S., Hansen, A., Wright, K. C., Deutsch, B. M., and Bigelow, N. P.: 2009, *Phys. Rev. Lett.* **103**, 250401

[20] Marzlin, K.-P., Zhang, W., and Sanders, B. C.: 2000, *Phys. Rev. A* **62**, 013602

[21] Schmeller, A., Eisenstein, J. P., Pfeiffer, L. N., and West, K. W.: 1995, *Phys. Rev. Lett.* **75**, 4290

[22] Schulz, T., Ritz, R., Bauer, A., Halder, A., Wagner, M., Franz, C., Pfleiderer, C., Everschor, K., Garst, M., and Rosch, A.: 2012, *Nature Physics* **8**, 301

[23] Shinjo, T., Okuno, T., Hassdorf, R., Shigeto, . K., and Ono, T.: 2000, *Science* **289(5481)**, 930

[24] Skyrme, T.: 1962, *Nuclear Physics* **31(0)**, 556

[25] Sondhi, S. L., Karlhede, A., Kivelson, S. A., and Rezayi, E. H.: 1993, *Phys. Rev. B* **47**, 16419

[26] Wong, S. M. H.: 2002

[27] Wright, D. C. and Mermin, N. D.: 1989, *Rev. Mod. Phys.* **61**, 385

[28] Zhai, H., Chen, W. Q., Xu, Z., and Chang, L.: 2003, *Phys. Rev. A* **68**, 043602

Chapter 6

An exact mapping between dissipative classical and quantum systems and its consequences- quantum critical jamming and quantum dynamical heterogeneities

6.1 Introduction

A prominent centerpiece in the understanding of numerous systems is Landau Fermi-liquid theory (LFT); this theory allows the understanding of phenomena such as conventional metals and low temperature He-3 liquids. LFT is centered on the

premise that the low energy states of interacting electron systems may be captured by long-lived fermionic quasi-particles with renormalized parameters (e.g., effective masses that differ from those of the bare electron). The last three decades have seen the discovery of materials in which electronic behavior deviates from simple LFT. These "singular" or "non-Fermi liquids" (NFL) include the high-temperature cuprate superconductors and "heavy fermions" (in which the effective electron mass becomes very large). While there are clear indications of changes in the dynamics in these systems–including putative quantum critical points (1; 2)– there is, in most cases, no clear experimentally measured length scale that exhibits a clear divergence. A quantum critical point is associated with a continuous phase transition at (absolute) zero temperature. Typically, this may occur in a system whose transition temperature is driven to zero by doping or the application of magnetic fields or pressure. Within a quantum critical regime, response functions follow universal power law scaling in both space and time. Specifically, at a quantum critical point, the effective infrared (IR) fixed point theory exhibits scaling invariance in space-time: $t \to \lambda t, x \to \lambda^{1/z} x$ with a dynamical exponent z that can, depending on the theory at hand, assume various canonical values. Unlike classical critical points whose associated critical fluctuations are confined to a narrow region near the phase transition, quantum critical fluctuations appear over a wide range of temperatures above the quantum critical point. These fluctuations may generally lead to a radical departure of the system's electronic properties from standard LFT type behavior. These features are anticipated to be common across many strongly correlated electronic systems and may be associated,

in some electronic systems, with a change of Fermi surface topology (3).

Many NFL systems exhibit numerous phases (including, quite notably, superconductivity). Indeed, competing orders and proliferation of multiple low energy states can lead to glassy behavior (4). The length scales characterizing these electronic systems undergo a much milder change than the corresponding changes in the dynamics. All of this suggests an effective infrared (IR) fixed point quantum field theory is invariant under scaling in time but not in space- i.e., the effective dynamical exponent $z \to \infty$. Response functions such as those of the marginal fermi liquid form describing cuprates show a marked frequency dependence but essentially no spatial momentum dependence. In this work, we will derive quantum systems with dynamical exponents $z \gg 1$.

It is natural to look elsewhere in physics where similar phenomena appear. One arena immediately comes to mind. In classical structural glasses there is a dramatic change in the dynamics as a supercooled liquid is quenched into a glass without the appearance of easily discernible large changes in measurable standard static length scales. While the ergodicity breaking that accompanies a glass transition cannot occur in a finite size system, it essentially mandates the appearance of a diverging static length scale (5), but such divergent length scales generally do not simply manifest themselves in bare standard correlation functions. General correlation functions which may monitor subtle changes include the "point to set" (6) correlations and others. Practically, in most instances (7) no clear signatures of a divergent length scales are easily seen in standard static two-point correlation functions.

A far more transparent growth in length scales is seen from four-point correlation functions that quantify the change in correlations as the system evolves in time. These correlation functions afford a glimpse into the length and time scaling which describe dynamical heterogeneities that characterize the spatially non-uniform rate of change or dynamics in the system. The length scale associated with these heterogeneities was seen to grow as the characteristic relaxation times increased.

We may use similar correlation functions to characterize strongly correlated electronic systems in which there are strongly discernible changes in the dynamics but no obvious experimentally accessible tools that point to accompanying divergent length scales in a general way (8). To our knowledge, to date, dynamical heterogeneities (nor general static measures such as those of the point-to-set method) have not been systematically probed for in electronic systems nor has their existence been established as a matter of principle in quantum system. Initial ideas concerning non-uniform doping-driven heterogeneities were discussed in (9). In this work, we flesh out the blueprint for a proof outlined in (10) and we will provide concrete "matter of principle" theoretical testimony of quantum dynamical heterogeneities in clean systems and related properties in quantum many body systems.

As is well appreciated, non-uniform spatial systems often exhibit interesting dynamical properties. For times shorter than the equilibration times, the auto-correlation of local fluctuations

$$C(t) = \langle \delta\phi(x,0)\delta\phi(x,t)\rangle. \tag{6.1}$$

plays the role of an "order parameter." This two-point correlation forms an analogue of the Edwards-Anderson (11) order parameter that appears in spin glasses. When they decay slowly with the time separation t, these autocorrelation functions clearly illustrate the presence of long range temporal correlations. The spatial correlation amongst pair products of time separated products of fields (such as those in Eq. (6.1)) at different spatial sites is a four point correlation function (12) that attempts to measure cooperation

$$G_4(x-y,t) = \langle \delta\phi(x,t)\delta\phi(x,0)\delta\phi(y,t)\delta\phi(y,0)\rangle - C^2(t). \tag{6.2}$$

This quantity relates the dynamics at two different spatial points x and y.

6.2 Quantum dynamical heterogeneities and quantum critical Jamming

In order to illustrate how, as a matter of principle, the physics of such classical dissipative systems can appear in clean quantum systems at zero temperature, we employ the mapping (13; 14; 15; 16) between classical viscous systems and quantum many body systems. Below (and in Section E), we briefly review this mapping and then discuss new consequences.

6.2.1 Lightning review of dissipative classical to quantum mapping and a new simple generalization

The crux of the mapping between dissipative classical systems and many body bosonic theories (13; 14; 15) is the realization that the equation of motion for a dissipative classical system is a first differential equation in time as is the Schrödinger equation. Using this equivalence, systems obeying the Langevin equation,

$$\gamma_i \frac{dx_i}{dt} = -\frac{\partial}{\partial \vec{x}_i} V_{\mathsf{N}}(\vec{x}_1, ..., \vec{x}_N) + \eta_i(t), \tag{6.3}$$

[with γ_i being the coefficients of friction, $\eta_i^\alpha(t)$ the Gaussian noise with $\langle \eta_i^\alpha(t)\eta_j^\beta(t')\rangle = 2T_{cl}\gamma_i\delta_{ij}\delta_{\alpha\beta}\delta(t-t')$ where T_{cl} the effective temperature of the classical system and, $\alpha, \beta = 1, 2, \ldots, d$ with d being the spatial dimensionality] can be exactly mapped (13; 14; 15) onto a many body system of bosons with mass $m_i = \gamma_i/(2T_{cl})$ at zero temperature which is governed by the Hamiltonian

$$\begin{aligned} H &= \sum_i \frac{1}{\gamma_i}\left[-T_{cl}\frac{\partial^2}{\partial \vec{x}_i^2} - \frac{1}{2}\nabla_i^2 V_{\mathsf{N}} + \frac{1}{4T_{cl}}(\nabla_i V_{\mathsf{N}})^2\right] \\ &\equiv \sum_i \frac{p_i^2}{2m_i} + \mathcal{V}_{\mathsf{Quantum}}(\{\vec{x}\}). \end{aligned} \tag{6.4}$$

The many body quantum potential $\mathcal{V}_{\mathsf{Quantum}}(\{\vec{x}\})$ is constructed from the the gradients of the classical potential energy V_N as identified in Eq. (6.4). Under this mapping, a dissipative classical system with a potential energy V_N that captures repulsive hard core spheres maps onto a bosonic system at zero temperature with (as

is apparent in the many body potential energy $\mathcal{V}_{\mathsf{Quantum}}$) similar dominant *hard-core* interactions. (15) In the Section E, we summarize, following (15), key aspects of this mapping. We now proceed to set the stage for our new result and its consequences.

In what follows, we trivially generalize earlier results for the dynamical structure factor and consider a general classical expectation value of the form

$$G_{\mathsf{classical}}(t) = \langle \mathcal{O}(t)\mathcal{O}(0)\rangle \tag{6.5}$$

where $\mathcal{O}(t)$ is *any* quantity. We may trivially replicate the steps of Biroli et al. (15) and extend these for general $\mathcal{O}$ (instead of the density function as considered in their work). We furthermore relate this result to a rather simple "complexification" of the time coordinate (or *Wick-type rotation*) in going from general classical correlation functions of the form of Eq. (6.5) to their corresponding bosonic counterparts. The final result is rather simple (Eq.(6.8)). If the spectral decomposition of Eq. (6.5) is given by

$$G_{\mathsf{classical}}(t) = \int_0^\infty d\omega\ W(\omega)e^{-\omega t}, \tag{6.6}$$

then the corresponding quantum response functions of operators $\hat{\mathcal{O}}$, in the ground state $|0\rangle$ of a bosonic system governed by the potential energy of Eq. (C.11), will be

given by

$$R_{\mathsf{Quantum}}(t) = \int_0^\infty \frac{d\omega}{2\pi} W(\omega) \cos \omega t. \tag{6.7}$$

The derivations of Eqs.(6.6,6.7) are carried in the Section E (see Eqs. (E.20, E.34) respectively).

Comparing Eqs. (6.6, 6.7), we see that, for *any* quantity $\mathcal{O}_q(t)$ if the quantum correlation function $G_{\mathsf{Quantum}}(\vec{q}, t)$ is evaluated with the quantum many body potential $\mathcal{V}_{\mathsf{Quantum}}(\{\vec{x}\})$ of Eq. (C.11) while the classical correlation function is computed for a system with a potential $V_{\mathsf{classical}}(\{\vec{x}\})$ then a very simple relation exists,

$$\boxed{R_{\mathsf{Quantum}}(t) = \frac{1}{2}(G_{\mathsf{classical}}(it) + G_{\mathsf{classical}}(-it)).} \tag{6.8}$$

[Alternatively, for a real $W(\omega)$, this is given by the real part of $G_{\mathsf{classical}}(it)$.] Eq. (6.8) is a key result of this work. In Section E, we provide a more detailed derivation of Eqs. (6.6, 6.7) that lead to Eq. (6.8). More general relation for correlation functions in systems with time dependent Hamiltonians (concerning evolving the system out of equilibrium classically or out of its ground state quantum mechanically) appear in Eqs. (E.17, E.21, E.22). Typically, in glassy systems, the correlation function of Eq. (6.5) is a superposition of many decaying modes- i.e., W is non-trivial distribution with finite width. As evident from Eqs. (6.6, 6.7), this distribution of modes will persist in

the corresponding quantum problem. For instance, if $G_{\mathsf{classical}} = A\exp[-(t/\tau)^a]$ then

$$R_{\mathsf{Quantum}} = Ae^{(-\frac{t}{\tau})^a \cos\frac{\pi a}{2}} \cos\Big[\Big(\frac{t}{\tau}\Big)^a \sin\frac{\pi a}{2}\Big]. \tag{6.9}$$

With the aid of the general relation of Eq. (6.8) (contrary to stated in (15)), the quantum correlation function that corresponds to a general stretched exponential correlation function in the classical arena can be computed analytically and is, indeed, given by Eq.(6.9). A trivial yet important particular realization of Eq. (6.8) is that of static correlations ($t = 0$) which, as is evident from Eq. (6.8), are identical in the classical and quantum systems.

6.3 Glassy quantum dynamics

Response functions in systems of variable plasticity such as various glass formers as their temperature is lowered (as well as various electronic systems) indicate, in a nearly universal fashion, the presence of a distribution of local relaxation times that lead to, e.g., the canonical Cole-Cole or Cole-Davidson and related forms as we briefly elaborate. In an over-damped dissipative system, an impulse (e.g., an external electric field or an elastic deformation) at time $t = 0$ leads to a response $g(t)$ which at later times, scales as $g_{single} \sim \exp(-t/\tau)$ where τ is the (single) relaxation time. When Fourier transformed to the complex frequency (ω) plane, this leads to $g_{single}(\omega) = g_0/(1 - i\omega\tau)$. In systems that exhibit a distribution ($P(\tau')$ of local relaxation events, the response functions attain the form $\int d\tau' P(\tau')\exp(-t/\tau')$.

Empirically, in dissipative plastic systems, relaxations scale as $(\exp(-t/\tau)^a)$ with a power $0 < a < 1$ that leads to a "stretching" (slower decay) of the response function as compared to its single over-damped mode form of $\exp(-t/\tau)$. This stretched exponential and other similar forms of the response function capture the epitome of the distribution of relaxation times. Two widely used relaxation time distributions are the Cole-Cole (CC) and Davidson-Cole (DC) functions that describe a superposition of over-damped oscillators.(17; 18) With $g(\omega) = g_0 G(\omega)$, where g_0 is a constant, these two forms are given by different choices for the function G,

$$G_{CC}(\omega) = 1/[1 - (i\omega\tau)^\alpha],$$
$$G_{DC}(\omega) = 1/[1 - i\omega\tau]^\beta. \tag{6.10}$$

Values of α and β that differ from unity qualitatively play the role of the real-time stretching exponent c. This distribution of relaxation times might be associated with different local dynamics (dynamical heterogeneities) to which we will turn shortly in subsection 6.3.1.

In the absence of imposed external disorder, when fluid components fall out of equilibrium by sufficient rapid cooling (so-called "super-cooling") to low enough temperatures, the resultant state is termed a "glass". As liquids are supercooled, their characteristic relaxation times and viscosity may increase dramatically.

Empirically, there are two time scales that govern the dynamics of supercooled liquids. These are called the α and β relaxation times. The α relaxation is asso-

ciated with cooperative motion and the dramatic viscosity increase (especially so in the "fragile" glass-formers). Empirically, the α relaxation times are given by Vogel-Fulcher-Tammann form for glasses (19),

$$\tau(T) = \begin{cases} \tau_0 \, e^{\Delta/(T-T_0)} & \text{for } T > T_0, \\ \\ \infty & \text{for } T \leq T_0. \end{cases} \tag{6.11}$$

Here, T_0 is the temperature at which the relaxation times would truly diverge and Δ is an energy scale. It is noteworthy that there are other relaxation forms such as those of the mode coupling theory (20).

By a trivial application of our result of Eq. (6.8), all of these lead to quantum zero-temperature counterparts.

6.3.1 Quantum dynamical heterogeneities

Our key result of Eq. (6.8) provides a natural bridge between classical and quantum correlations between disparate operators $\{\hat{\mathcal{O}}(t)\}$. The remainder of this work will largely focus on consequences of this relation. From it, correlation times $\{\tau_\alpha\}$ that appear in the classical problem will rear their head in the quantum problem (and vice versa).

We now focus on an intriguing aspect of classical glasses which by virtue of the relation of Eq. (6.8) [as alluded to in (10)] leads to the appearance of new dynamical correlations in quantum systems. Disorder free models for classical glass formers

(including various simulated quenched systems such as those endowed with various classical potentials V_N (e.g., (22)) that do not permit simple crystalline orders) are known to exhibit "dynamical heterogeneities" (DH)- a non-uniform distribution of local velocities (21) with the location of the more rapidly moving particles changing with time. By invoking Eq. (6.8), we see that *Quantum dynamical heterogeneities* (10) appear in their corresponding zero temperature quantum counterparts. That is, in disorder free quantum systems derived (via Eq. (6.4)) from the corresponding classical systems, zero point dynamics is spatially non-uniform.

The presence of DH is seen by numerous probes (21). One often used metric is that of the four-point correlations of Eq. (6.2) in various guises. These correlation functions are of the form of Eq. (6.5) with $\mathcal{O}(t)$ denoting the overlap between fields ϕ when these are separated in time,

$$\mathcal{O}(t) = \phi_q(t)\phi_{-q}(0) - \langle\phi_q(t)\rangle\langle\phi_{-q}(0)\rangle, \tag{6.12}$$

with $\vec{q}$ any wave-vector. Typically, ϕ is set equal to the particle density ρ. When Eq. (6.12) is substituted into Eq. (6.5), the Fourier space correlation functions (denoted $S_4^{\mathsf{classical}}(\vec{q},t)$ below) typically have an Ornstein-Zernicke type or similar related forms, e.g., (23)

$$S_4^{\mathsf{classical}}(\vec{q},t) = \frac{\chi_4(t)}{1+q^2\xi_4(t)^2}, \tag{6.13}$$

with the length scale $\xi_4(t)$ representing the size of the typical dynamical heterogeneities when the system is examined at two times separated by an interval t. We may next invoke Eq. (6.8) to generate the quantum counter-part of Eq. (6.13) (or of any other related form) and Fourier transform to real space to obtain, in the notation of Eq. (6.2), the spatial bosonic correlation function $G_4^{\mathsf{Quantum}}(\vec{x}-\vec{y},t)$ associated with the potential $\mathcal{V}_{\mathsf{Quantum}}$ of Eq.(C.11). The Fourier integral will be dominated by momentum space poles at $q = \pm i\xi_4^{-1}$. It is clear that in employing the transformation of Eq. (6.8), $G_4^{\mathsf{Quantum}}(\vec{x}-\vec{y},t)$ will exhibit exponential decay with the very same correlation length ξ_4 that is present in the classical system. This affords a direct proof of the dynamical length scales ξ_4 in *all zero temperature quantum counter-parts* (given by Eq. (6.4)) to any dissipative classical system that is known to exhibit these (and there are numerous known classical systems that exhibit dynamical heterogeneities (21)).

6.3.2 Rapidly increasing time scale with concomitant slowly increasing length scales in quantum glasses

There is a proof that a growing static length scale must accompany the diverging relaxation times of glass transitions (5). Some evidence has indeed been found for growing correlation lengths (static and those describing dynamic inhomogeneities) (27; 28; 29). As we noted earlier in this work, correlation lengths were studied via "point-to-set" correlations (6; 30) and pattern repetition size (31). Other current

common methods of characterizing structures include (a) Voronoi polyhedra, (32; 33; 34), (b) Honeycutt-Andersen indices (35), and (c) bond orientation (36): all centering on an atom or a given link. More recent approaches include graph theoretical tools (37). Not withstanding current progress, it is fair to say that currently most "natural" textbook type length scales do not increase as dramatically as the relaxation time does as a liquid is supercooled towards the glass transition temperature.

It is worthwhile to highlight that one of the most pertinent naturally increasing length scales is that associated with the typical size of the dynamical heterogeneity (i.e., ξ_4 of Eq. (6.13)). Similar to other measures, this typical length scale does not increase as rapidly as the characteristic relaxation time does as the glass transition is approached. Recent work for a three-dimensional bi-disperse repulsive glass (38) [with the pair potential $V(|\vec{x}|) = \epsilon(\sigma_{ab}/r)^{12}$ between two particles (a, b) of two possible types $((a, b) \in 1, 2)$ with $\sigma_{ab} = (\sigma_a + \sigma_b)/2$ and $\sigma_2/\sigma_1 = 1.2)$], suggests that

$$\tau \sim \exp(k\xi^{\theta}) \tag{6.14}$$

with $\theta \simeq 1.3$ and k a constant. (An alternate assumed algebraic form $\tau \sim \xi_4^z$ leads to an extremely large dynamical exponent $z \simeq 10.8$.) In these cases, the dynamics changes dramatically with little notable change in the spatial correlation length.

6.3.3 Quantum Critical Jamming

The mapping between dissipative classical and quantum systems also suggests a new quantum critical point in related systems. The classical jamming transition (39; 40; 41; 42; 43; 44; 45; 46; 47; 48) of hard spheres/disks from a jammed system at high density to an unjammed one with spatially heterogeneous motion at lower densities is a continuous transition with known critical exponents, both static (40) and dynamic (48). Replicating the mapping of the previous subsection (and, in particular, Eq. (6.8) therein), we may derive an analog quantum system harboring a zero temperature transition with similar critical exponents. The classical zero temperature critical point ("point J") (39; 40) may rear its head anew in the form of *quantum critical jamming* (at a new critical point—"Quantum point J") of the bosonic systems with dynamical exponents as we may ascertain from those reported for the classical jamming system (48). The classical zero temperature system ($T_{cl} = 0$) maps, according to Eq. (6.4), onto a quantum system in the large mass limit. Bosons at infinite mass are not trivial due their statistics Specifically, for a system of mono-disperse soft spheres with a repulsive force that is linear in the amount of compression, it was found that the correlation length ξ and relaxation time τ scale (48) as

$$\xi \sim (\rho_J - \rho)^{-0.7},$$
$$\tau \sim (\rho_J - \rho)^{-3.3}. \tag{6.15}$$

In Eq. (6.15), ρ denotes the density with ρ_J being the critical density at the jamming transition. Eq. (6.15) describes how the spatial and time scales diverge as the density is increased and approaches (from below) the density at the jamming transition. Taken together, these imply that, on approaching the transition, the relaxation time increases much more rapidly than the correlation length, $\tau \sim \xi^z$ with a very large effective dynamical exponent $z \simeq 4.6$. By use of Eq. (6.8), the same behavior is to be expected for the quantum system governed by the corresponding quantum potential $\mathcal{V}_{\mathsf{Quantum}}$. In physical terms, for charged bosons, the jamming transition constitutes a transition from a metallic system (when the system is unjammed and behaves as a fluid) to a jammed state (an insulator). As in earlier sections, we see that time scales increase far more precipitously than spatial correlation lengths.

6.4 Lattice systems

Thus far, we focused on continuum viscous classical systems which, as we have seen, mapped onto continuum bosonic systems. We briefly remark on classical lattice systems which similarly exhibit dynamical heterogeneities and a jamming type transition. Refs.(51; 52) studied, respectively, the 2DN3 and 3DN2 models on the square and cubic lattice models in $D = 2$ and $D = 3$ dimensions. In the N3 model, particles are endowed with hard core repulsive interactions that extend up to a distance of three steps on the lattice. Similarly, in the N2 model particles cannot be nearest neighbors nor next nearest neighbors (i.e., the repulsive hard-core interactions extend up to a

distance of two steps on the lattice). Thus, similar to the continuum systems that we discussed earlier, these models may be regarded as that of classical hard core spheres. Following the mapping reviewed earlier, the quantum counterpart of such systems is that of dominant hard sphere interactions. In the classical systems, simulation starts (51; 52) with an infinitely fast quenching wherein particles are added whenever possible and diffuse otherwise; this process is halted when the desired density is reached. A clear increase was noted in the length scales that characterize the dynamical heterogeneity (51; 52). The continuum jamming transition discussed earlier may have a lattice counterpart for Cooper pairs as we now elaborate on. A natural quantum counterpart to the N3 (N2) model is given by an extended Bose Hubbard (53; 54) type model with infinite hard core repulsions,

$$H = -t \sum_{\langle ij \rangle} (b_i^\dagger b_j + h.c.) + U \sum_i n_i(n_i - 1) + \sum_{ij} V_{ij} n_i n_j, \tag{6.16}$$

where $V_{ij} \to \infty$ for lattice sites i and j which are fewer than four (or three) steps apart and the onsite Hubbard repulsion U is divergent ($U \to \infty$) as well. The Hubbard term leads to a penalty only when there is a double or higher occupancy. Based on our considerations thus far, we expect to obtain the quantum bosonic counterpart to the classical jamming transitions found in the classical 2DN3 and 3DN2 models. This bosonic system may have all of the characteristics of the classical jammed system including dynamical heterogeneities and a large dynamical exponent z. For completeness, we briefly comment on the difference between the lattice system of

Eq. (6.16) and the "Bose glass" first introduced in (53). The Bose glass appears in the bare (i.e., that with $V_{ij} = 0$) disordered rendition of Eq. (6.16) with the general Bose Hubbard Hamiltonian (with general finite repulsion U) being further augmented by a local chemical potential term $-\sum_i \mu_i n_i$ wherein μ_i is a spatially non-uniform random quantity. By contrast, the lattice Hamiltonian of Eq. (6.16) as well as the continuum models that we discussed in earlier sections are free of disorder. The amorphous characteristics that these clean systems may exhibit are borne out of "self-generated" randomness (55)—not randomness that is present in the parameters defining the system.

6.5 Electronic systems with pairing interactions

Up to now, building on and extending the mapping between classical dissipative systems and zero temperature bosonic theories, we focused on hard core bosons. We now turn to the ground states of Fermi systems. In particular, in this section, we will consider standard electronic systems with pairing interactions,

$$H = \sum_{\vec{k},\sigma} \epsilon_{\vec{k}} c^\dagger_{\vec{k}\sigma} c_{\vec{k}\sigma} + \sum_{\vec{k},\vec{l}} V_{\vec{k},\vec{l}} c^\dagger_{\vec{k}\uparrow} c^\dagger_{-\vec{k}\downarrow} c_{-\vec{l}\downarrow} c_{\vec{l}\uparrow}, \tag{6.17}$$

where $\sigma = \uparrow, \downarrow$ is the spin polarization index and V_{kl} is the interaction strength between the Cooper pairs

$|\vec{k}\uparrow; -\vec{k}\downarrow\rangle$ and $|\vec{l}\downarrow; -\vec{l}\uparrow\rangle$. As is well known (and is readily verified), the following

Fermi billinears

$$\bar{b}^{\dagger}_{\vec{k}} = c^{\dagger}_{\vec{k}\uparrow} c^{\dagger}_{-\vec{k}\downarrow},$$
$$\bar{b}_{\vec{k}} = c_{-\vec{k}\downarrow} c_{\vec{k}\uparrow} \tag{6.18}$$

corresponding to the creation/annihilation of Cooper pairs satisfy hard core Bose algebra. We next consider what occurs if, within the ground state, the occupancies of the single particle states are correlated inasmuch as the electronic states on which the standard pairing Hamiltonian of Eq. (6.18) operates can be created by applications of Cooper pair creation operators on the vacuum (i.e., if the ground state is invariant under the combined operations of parity $\mathcal{P}$ ($\vec{k} \to -\vec{k}$) and time reversal $\mathcal{T}$ ($\sigma \to -\sigma$)). When the ground state is strictly invariant under the combined effect of these $\mathcal{PT}$ symmetries we may express the Hamiltonian of Eq. (6.17) as a bilinear in the hard core Bose operators,

$$H = \sum_{\vec{k},\vec{l}} (2\epsilon_{\vec{k}} \delta_{\vec{k},\vec{l}} + V_{\vec{k},\vec{l}}) \bar{b}^{\dagger}_{k} \bar{b}_{l}. \tag{6.19}$$

As is well known, the hard core Bose algebra of the $\bar{b}^{\dagger}_{\vec{k}}$ and $\bar{b}_{\vec{k}}$ operators is identical to that of the spin $S = 1/2$ raising and lowering operators $S^{+}_{\vec{k}}$ and $S^{-}_{\vec{k}}$. Thus, Eq. (6.19) is equivalent to an XY model. In situations in which the band dispersion $\epsilon_{\vec{k}}$ is nearly flat (and may be omitted for fixed particle number), in determining the ground state(s), we must only find the pairing V that affects pair hopping. Similar

considerations apply in real-space when Coopers are short ranged and may be replaced by real-space hard-core bosons. Hard core real space contact interactions correspond to uniform $V_{\vec{k},\vec{l}}$ (independent of $\vec{k}$ and $\vec{l}$) as in the BCS form for the pairing interactions. In such cases, whenever the system is dominated by hard core contact interactions between bosons, replicating our analysis thus far, at zero temperature, the system may undergo a jamming type transition at sufficiently high densities and display rapidly increasing relaxation times concomitant with spatial correlations that do not increase as dramatically as the relaxation times do on approaching this transition.

6.6 Conclusions

The central result of this work is the exact correspondence of Eq. (6.8). This equality relates **(i)** the autocorrelation function of Eq. (6.5), for *any quantity* $\mathcal{O}$ when evaluated for the classical dissipative system of Eq. (6.3) with a many body potential energy V_N, to **(ii)** the autocorrelation function of the very same corresponding quantum operator $\hat{\mathcal{O}}$ in a bosonic system governed by the Hamiltonian of Eq. (6.4). When fused with known results for dissipative classical systems, this extremely versatile equality immediately leads to numerous effects which we introduced and readily proved as a matter of principle. These include:

• *Quantum dynamical heterogeneities* (QDH). We illustrated that similar to classical systems even in the absence of disorder, bosonic systems can, at zero temperature, exhibit spatially non-uniform zero point motion. Of course, in translationally invari-

ant systems, the average (time averaged) dynamics is uniform. However, at any given time, there are particles that move more rapidly than others.

• The length scale characterizing the zero temperature QDH, the four-point correlation length ξ_4 (a trivial analog of its classical counterpart) may increase as the dynamics of the clean Bose system becomes progressively sluggish. However, albeit its rise, this length scale may increase much more slowly than the relaxation time. The far more rapid increase of the relaxation time as compared to readily measured length scales is a hallmark of many electronic systems. Cast in terms of quantum critical scaling (if and when it might be realized), the effective dynamical exponent z capturing the relation between correlation lengths and times $\tau \sim \xi^z$, is very large ($z \gg 1$). Other relations such as those of Eq. (6.14) may hold once they are established for viscous classical systems.

• Similar to classical systems, quantum systems may jam at high densities notwithstanding zero point motion. The character of the jamming transition in zero temperature quantum systems is identical to that of that of their corresponding counterparts. As the classical systems exhibit a critical point at the jamming transition (at "point J") so do their bosonic counterparts. As a result, we established the existence of a new quantum critical point—associated with a *quantum critical jamming* of a hard core Bose system. As in the other systems that we discuss the characteristic relaxation time diverges more precipitously than the correlation length on approaching the transition ("Quantum point J") with a large effective dynamical exponent $z \simeq 4.6$.

• The off-lattice theories that we discuss above may have a broad applicability

as continuum theories describe the same physics as their lattice renditions do in the vicinity of critical points. In Section 6.4, we discussed specific possible lattice renditions.

• The results that we derived for zero temperature bosonic theories suggest similar features in electronic systems. In some cases, as discussed in Section 6.5, finding the ground states interacting electronic systems can be cast in terms of a corresponding zero temperature hard-core Bose problem.

Thus, with the aid of the viscous classical-many body quantum correspondence of Eq. (6.8), we trivially established all of these results sans the need to perform various standard and far more laborious computations for quantum systems.

Bibliography

[1] S. Sachdev, *Quantum Phase Transitions*, (Cambridge University Press, 2004).

[2] C. M. Varma, Z. Nussinov, and W. van Saarloos, Physics Rep. **361**, 267 (2002).

[3] Y. S. Oh, *et al.*, Phys. Rev. Lett. **98**, 016401 (2007).

[4] Z. Nussinov, I. Vekhter, and A. V. Balatsky, Phys. Rev. B **79,** 165122. (2009).

[5] A. Montanari and G. Semerjian, J. Stat. Phys. **125**, 23 (2006).

[6] G. Biroli, J.-P. Bouchaud, A. Cavagna, T. S. Grigera, and P. Verrocchio, Nature Phys. **4**, 771 (2008).

[7] H. Tanaka, T. Kawasaki, H. Shintani, and K. Watanabe, Nature Mat. **9**, 324 (2010).

[8] M. J. Lawler, *et al.*, Nature Lett. **466**, 347 (2010).

[9] C. Panagopoulos and V. Dobrosavljevic, Phys. Rev. B **72**, 014536 (2005).

[10] Z. Nussinov, Physics **1**, 40 (2008).

[11] S. F. Edwards and P. W. Anderson, J. Phys. F: Metal Phys. **5**, 965 (1975).

[12] C. Dasgupta A. V. Indrani, S. Ramaswamy, and M. K. Phani, Europhys Lett.**15**, 307 (1991).

[13] G. Parisi, *Statistical Field Theory*, (Addison Wesley, New York, 1988).

[14] J. Zinn-Justin, *Quantum Field Theory and Critical Phenomena*, (Oxford University Press, 2002).

[15] G. Biroli, C. Chamon, and F. Zamponi, Phys. Rev. B **78**, 224306 (2008).

[16] C. Castelnovo, C. Chamon, and D. Sherrington, Phys. Rev. B **81**, 184303 (2010)

[17] K. S. Cole and R. H. Cole, J. of Chem. Phys. **9**, 341 (1941).

[18] 66. D.W. Davidson and R. H. Cole, Journal of Chem. Phys. **18**, 1417 (1950); ibid. **19**, 1484 (1951).

[19] J. Rault, J. of Non-Crystalline Solids **271**, 177 (2000)

[20] D. R. Reichman and P. Charbonneau, J. Stat. Mech. P05013 (2005)

[21] H. Sillescu, J. Non-Cryst. Solids **243**, 81 (1999); M.D. Ediger, Ann. Rev. Phys. Chem. **51**, 99 (2000); R. Richert, J. Phys.: Condens. Mat. **14**, R703 (2002); W. Kob, C. Donati, S.J. Plimpton, P.H. Poole, and S.C. Glotzer, Phys. Rev. Lett. **79**, 2827 (1997); C. Donati, J.F. Douglas, W. Kob, S.J. Plimpton, P.H. Poole, and S.C. Glotzer, ibid, **80**, 2338 (1998); S.C. Glotzer, J. Non-Cryst. Solids **274**, 342 (2000); Y. Gebremichael, T.B. Schroder, F.W. Starr, and S.C. Glotzer, Phys. Rev. E **64**, 051503 (2001).

[22] W. Kob and H. C. Andersen, Phys. Rev. E **51**, 4626 (1995).

[23] S. Karmakar, C. Dasgupta, and S. Sastry, PNAS **106**, 3675 (2009)

[24] W. Kob, C. Donati, S. J. Plimpton, P. H. Poole, and S. C. Glotzer, Phys. Rev. Lett. **79**, 2827 (1997)

[25] R. P. A. Dullens and W. K. Kegel, Phys. Rev. E **71**, 011405 (2005)

[26] J.-X. Lin, C. Reichhardt, Z. Nussinov. L. P. Pryadko, and C. J. Olson Reichhardt, Phys. Rev. E **74**, 011403 (2006)

[27] M. Mosayebi, E. D. Gado, P. Iig, and H. C. Ottinger, ‘ Phys. Rev. Lett. **104**, 205704 (2010)

[28] L. Berthier, G. Biroli, J.-P. Bouchaud, L. Cipelletti, D. El Masri, D. L'Hote, F. Ladieu, and M. Pierno, Science **310**, 1797 (2005).

[29] S. Karmakar, C. Dasgupta, and S. Sastry, Proc. Natl. Acad. Sci. U.S.A. **106**, 3675 (2010).

[30] J.-P. Bouchaud and G. Biroli, J. Chem. Phys. **121**, 7347 (2004)

[31] J. Kurchan and D. Levine, e-print arXiv:0904.4850 (2009).

[32] E. Aharonov, E. Bouchbinder, H. G. E. Hentschel, V. Ilyin, N. Makedonska, I. Procaccia, and N. Schupper, Euro. Phys. Lett. **77**, 56002 (2007)

[33] H. W. Sheng, W. K. Luo, F. M. Alamgir, J. M. Bai, and E. Ma, Nature **439**, 419 (2006)

[34] J. L. Finney, Proc. R. Soc. London, Ser. A **319**, 1539, 479 (1970)

[35] J. Dana Honeycutt and Hans C. Andersen, J. Phys. Chem. **91**, 4950 (1987)

[36] P. J. Steinhardt, D. R. Nelson and M. Ronchetti, Phys. Rev. B **28**, 784(1983)

[37] P. Ronhovde, S. Chakrabarty, M. Sahu, K. F. Kelton, N. A. Mauro, K . K. Sahu, and Z. Nussinov, European Physics Journal E **34**, 105 (2011); P. Ronhovde, S. Chakrabarty, M. Sahu, K. K. Sahu, K. F. Kelton, N. Mauro, and Z. Nussinov, Scientific Reports **2**, 329 (2012)

[38] H. Mizuno and R. Yamamoto, Phys. Rev. E **84**, 011506 (2011)

[39] A.J. Liu and S. R. Nagel, Nature (London) **396**, 21 (1998)

[40] C. S. O'Hern, S. A. Langer, A. J. Liu, and S. R. Nagel, Phys. Rev. Lett. **88**, 075507 (2002)

[41] C. S. O'Hern, L. E. Silbert, A. J. Liu, and S. R. Nagel, Phys. Rev. E **68**, 011306 (2003)

[42] J. A. Drocco, M. B. Hastings, C. J. Olson Reichhardt, and C. Reichhardt Phys. Rev. Lett. **95**, 088001 (2005)

[43] O. Dauchot, G. Marty, and G. Biroli, Phys. Rev. Lett. **95**, 265701 (2005)

[44] A. R. Abate and D. J. Durian, Phys. Rev. E **74**, 031308 (2006)

[45] A. R. Abate and D J. Durian, Phys. Rev. E **76**, 021306 (2007)

[46] A. S. Keys, A. R. Abate, S C. Glotzer, and D. J. Durian, Nature Phys. **3**, 260 (2007)

[47] F. Lechenault, O. Dauchot, G. Biroli, and J.-P. Bouchaud, Europhys. Lett. **83**, 46003 (2008)

[48] T. Hatano, Phys. Rev. E **79**, 050301(R) (2009)

[49] B. U. Felderhof, Reports Math. Phys. **1**, 215 (1970); B. U. Felderhof and M. Suzuki, Physica **56**, 43 (1971)

[50] "Spin Glass Theory and Beyond", M. Mezard, G. Parisi and M. A. Virasoro World Scientific, Singapore (Teaneck, N J.), 1987.

[51] Z. Rotman and E. Eisenberg, Phys. Rev. Lett. **105**, 225503 (2010).

[52] H. Levit, Z. Rotman, and E. Eisenberg, Phys. Rev. E **85**, 011502 (2012).

[53] M. P. A. Fisher, P. B. Weichman, G. Grinstein, and D. S. Fisher, Phys. Rev. B **40**, 546 (1989)

[54] G.T. Zimanyi, P.A. Crowell, R.T. Scalettar, and G.G. Batrouni, Phys. Rev. B **50**, 6515 (1994).

[55] J. Schmalian and P. G. Wolynes, Phys. Rev. Lett. **85**, 836 (2000).

Chapter 7

Conclusion

This dissertation presents new results dealing with the appearance of patterns (both classical and quantum) in diverse arenas including classical and quantum systems. These patterns included solving the Nonlinear Schrödinger Equation in the context of rogue waves. It also included results dealing with magnetic behavior of Cobalt nanoparticles with a focus on hemispherical particles and a focus on the effects of demagnetizing energy. Lastly, this dissertation predicts appearance of quantum "dynamical heterogeneities" in systems.

In Chapter 3, the Nonlinear Schrödinger Equation was solved in a very general fashion. These solutions were used to generate approximate solutions in the form of a generalized compacton where the rogue wave is surrounded by a periodic background rather than a constant background. This was followed by a discussion of the case of $d+1$ dimensions and external noise and source terms were discussed. Next, the connection to ϕ^4 field theories is drawn as the Nonlinear Schrödinger Equation is the

nonrelativistic equation of motion of a ϕ^4 theory. Finally, a possible way for rogue waves to appear as the opposite of a dissipative process due to the time-reversal invariance of the theory.

In Chapter 4, the general expression for the demagnetizing factor of a hemisphere is calculated and given in its full spatially dependent form in Appendix B. This is verified by taking limits for the apex and the center of the base of the hemisphere which can be verified by basic electrodynamics. This is further checked by introducing a new method for numerically calculating the demagnetizing factor for a general geometry. Included in this chapter is a brief discussion of using shape anisotropy to create controlled hysteresis loops with jumps at certain field strengths.

In Chapter 5, observations of skyrmions in simulations of Cobalt nanoparticles were discussed. The observation of the skyrmions were significant because they are stabilized by a balance of only field, demagnetization, and exchange energies. In the past, complicated balancing of other anisotropies were needed to allow for the skyrmionic state. Lastly, arrays of skyrmions were analyzed along with the stability of the skyrmion state in these arrays.

In Chapter 6, a very general result was derived allowing a mapping between classical and quantum systems. This mapping can be used to translate classical systems that are easy to generate results into quantum systems of fermions and bosons which can be quite difficult. This general mapping allows for results to be derived dealing with quantum jamming and dynamical heterogeneities.

Appendix A

Sample MIF 2.1 File Used for OOMMF Simulations

In this section is contained an example input file for the OOMMF simulations done in this work. This specific file generates a Cobalt hemisphere of radius 10 nm going through a range of fields starting at $2\,T$ in the negative z-direction, going up to $2\,T$ in the positive z-direction, and then back down to $2\,T$ in the negative z-direction.

```
# MIF 2.1
# This file converted from MIF 1.1 format by MIF Conversion utility 1.2.0.1
# Original file: /Users/patrickjohnson/Downloads/oommf/Disk5by10.mif
#
# Cobalt Info
#
set PI [ expr { 4*atan(1.) } ]
```

```
set MU0 [ expr { 4*$PI*1e-7 } ]

proc Hemi { radius x y z xmin ymin zmin xmax ymax zmax} {

global RegionArray

set distance [expr {$x*$x+$y*$y+$z*$z}]

set radius2 [expr {$radius*$radius}]

if {$distance<$radius2} {

if {$z >0} {

return 1

}

}

return 0

}

Specify Oxs _ScriptAtlas:hemisphere {

xrange {-12e-9 12e-9}

yrange {-12e-9 12e-9}

zrange {-2e-9 12e-9}

regions { cobalt }

script _args { rawpt minpt maxpt}

script { Hemi 10e-9 }

}

Specify Oxs _RectangularMesh:mesh {

cellsize {1e-9 1e-9 1e-9}
```

```
atlas :hemisphere

}

Specify Oxs _UniformExchange {

A 2.5E-11

}

Specify Oxs _Demag {}

Specify Oxs_UZeeman:extfield0 [ subst {

comment {Field values in Tesla; scale to A/m}

multiplier [ expr {1/ $ MU0 } ]

Hrange {

{0 0 -2 0 0 2 200}

{0 0 2 0 0 -2 200}

}

}]

Specify Oxs _EulerEvolve {

do _precess 1

gamma _LL 2.21e5

alpha 0.5

}

Specify Oxs _TimeDriver {

basename Hemisphere10nmZ-Field/Hemisphere10nmZ-Field

vector_field_output_format {binary 4}
```

```
    scalar_output_format %.15g

    evolver Oxs_EulerEvolve

    mesh :mesh

    stopping_dm_dt 0.19819739783994714

    stage_count 401

    Ms {Oxs_AtlasScalarField {

    atlas :hemisphere

    values {

    universe 0

    cobalt 1400E3

    } } }

    m0 { Oxs_UniformVectorField { norm 1 vector { -0.8 0.6 0} } }

    }

    Destination archive10nmZ-Field:data mmArchive new

    Destination archive10nmZ-Field:mag mmArchive new

    Schedule DataTable archive10nmZ-Field:data Stage 1

    Schedule Oxs_TimeDriver::Magnetization archive10nmZ-Field:mag Stage 1

    ########################################

    # Unused fields:

    Ignore {

    totalfieldoutputformat: binary 4

}
```

To comment on the different parts of this file. It begins with a comment section as designated by the # sign followed by descriptions of the generation of the file. Following that is the setting constant parameters such as π and μ_0.

The "proc Hemi" section of the file determines the geometry of the system. In the example file shown here, it is a hemisphere geometry. The arguments being passed to this routine are the radius, the Cartesian coordinates, and the range of Cartesian coordinates as determined by the "Oxs_ScriptAtlas" routine. The specifications of arguments "rawpt minpt maxpt," specifies that the script will be passed the raw coordinates (x, y, z), the minimum values for the coordinates (xmin, ymin, zmin), and the maximum values for the coordinates (xmax, ymax, zmax). The mathematics calculates the distance from the current point to the origin and decides whether it is inside or outside the hemisphere and returns a 1 for inside and 0 for outside.

The "Oxs_ScriptAtlas:hemisphere" routine specifies the size of the system by specifying what range all the coordinates span along with radius, which is specified in the "script {Hemi 10e-9}" as $10\,nm$ in this file.

The "Oxs_RectangularMesh" routine specifies the rectangular grid spacing for the simulation in nanometers.

The "Oxs_UniformExchange" routine specifies the exchange stiffness constant in J/m.

The "Oxs_UZeeman:extfield0" routine sets the value for the field in Tesla. The "Hrange" field sets the beginning and then ending value of the field and how many steps into which to break the range up.

The "Oxs_EulerEvolve" routine specifies the constants in the Landau-Lifshitz-Gilbert Equation including the Landau-Lifshitz gyromagnetic ratio and the damping constant, α.

The "Oxs_TimeDriver" routine specifies many different parameters. The "basename" parameter specifies the value of the filename to be built off of by the code. The "stopping_dm_dt" parameter specifies the value of the maximum torque experienced by any one spin before the code considers the system close enough to a steady state. The "stage_count" specifies how many steps will be taken in the simulation. This can be calculated by taking the sum of the number of steps in the "Hrange" field plus one. The value next to "cobalt" specifies the saturation magnetization in A/m. The "m0" parameter sets the initial state of the system. The "Destination" and "Schedule" commands dictate where the data is to be saved.

Appendix B

Full Expresion of Demagnetization Factor of a Hemisphere in the X-Direction

Written below is the full expression for the demagnetizing factor of a hemisphere in the x-direction.

$$\langle N_x \rangle = \sum_{i=1}^{107} A_i \tag{B.1}$$

Using the shorthand:

$$r = \sqrt{x^2 + y^2}$$

$$K = \text{EllipticK}\left[\frac{4Rr}{(R+r)^2 + z^2}\right], E = \text{EllipticE}\left[\frac{4Rr}{(R+r)^2 + z^2}\right]$$

$$\Pi_1 = \text{EllipticPi}\left[\frac{2r}{r + \sqrt{r^2 + z^2}}, \frac{4Rr}{(R+r)^2 + z^2}\right]$$

$$\Pi_2 = \text{EllipticPi}\left[\frac{2r}{r - \sqrt{r^2 + z^2}}, \frac{4Rr}{(R+r)^2 + z^2}\right]$$

$$A_1 = \frac{1}{3}\pi\left(2 + \frac{6R^3x^2}{\left(r^2+z^2\right)^{5/2}} - \frac{2R^3}{\left(r^2+z^2\right)^{3/2}}\right)$$

$$A_2 = \frac{4x^2\left(R+r\right)zK}{r\left(\left(R+r\right)^2+z^2\right)^{3/2}}$$

$$A_3 = -\frac{2zK}{\sqrt{\left(R+r\right)^2+z^2}}$$

$$A_4 = -\frac{x^2\left(R+r\right)^2 z\left(R^2+3r^2+3z^2\right)K}{r^2\left(\left(R+r\right)^2+z^2\right)^{5/2}}$$

$$A_5 = \frac{x^2 z\left(R^2+3r^2+3z^2\right)K}{3r^2\left(\left(R+r\right)^2+z^2\right)^{3/2}}$$

$$A_6 = -\frac{x^2\left(R+r\right)z\left(R^2+3r^2+3z^2\right)K}{3r^3\left(\left(R+r\right)^2+z^2\right)^{3/2}}$$

$$A_7 = \frac{\left(R+r\right)z\left(R^2+3r^2+3z^2\right)K}{3r\left(\left(R+r\right)^2+z^2\right)^{3/2}}$$

$$A_8 = -\frac{z\left(R^2+3r^2+3z^2\right)\left(16R^2x^2\left(R^2-r^2+z^2\right)^2\right)\left(E-B_{22}K\right)}{24Rr^3B_{22}^2\left((r+R)^2+z^2\right)^{7/2}}$$

$$A_9 = -\frac{4Rz\left(R^2+3r^2+3z^2\right)}{r^3\left((r+R)^2+z^2\right)^{5/2}}\frac{E-B_{22}K}{24RrB_{22}} \times \left(B_1+B_{21}\right)$$

$$B_1 = \left(r^2 - x^2\right) z^4 - (r+R)^2 \left(r^4 + 4rRx^2 + R^2x^2 - r^2\left(R^2 + 3x^2\right)\right)$$

$$B_{21} = 2\left(r^2R(r+R) - \left(3r^2 + 3rR + R^2\right)x^2\right) z^2$$

$$B_{22} = \left(1 - \frac{4Rr}{(R+r)^2 + z^2}\right)$$

$$A_{10} = -\left(\frac{4x^2z\left(-r^2 + R^2 + z^2\right)}{r\left((r+R)^2 + z^2\right)^{3/2}}\right)\frac{E - B_{22}K}{2rB_{22}}$$

$$A_{11} = \left(R^2 + 3r^2 + 3z^2\right)\left(\frac{4x^2z\left(-r^2 + R^2 + z^2\right)}{r\left((r+R)^2 + z^2\right)^{3/2}}\right)\frac{E - B_{22}K}{24r^3B_{22}}$$

$$A_{12} = -\frac{z\left(R^2 + 3r^2 + 3z^2\right)}{24RrB_{22}}B_2\left(\frac{E-K}{8Rr}B_2 + \frac{B_2K}{(r+R)^2 + z^2} - \frac{(E - B_{22}K)}{8Rr}B_2\right)$$

$$B_2 = \frac{4Rx\left(-r^2 + R^2 + z^2\right)}{r\left((r+R)^2 + z^2\right)}$$

$$A_{13} = \frac{3x^2\left(R+r\right)^2 z\left(R^2 + r^2 + 2Rr + z^2\right)E}{r^2\left(\left(R+r\right)^2 + z^2\right)^{5/2}}$$

$$A_{14} = -\frac{2x\left(2x + \frac{2Rx}{r}\right)\left(R+r\right)zE}{r\left(\left(R+r\right)^2 + z^2\right)^{3/2}}$$

$$A_{15} = -\frac{x^2 z\left(R^2+r^2+2Rr+z^2\right)E}{r^2\left(\left(R+r\right)^2+z^2\right)^{3/2}}$$

$$A_{16} = \frac{x^2\left(R+r\right)z\left(R^2+r^2+2Rr+z^2\right)E}{r^3\left(\left(R+r\right)^2+z^2\right)^{3/2}}$$

$$A_{17} = -\frac{\left(R+r\right)z\left(R^2+r^2+2Rr+z^2\right)E}{r\left(\left(R+r\right)^2+z^2\right)^{3/2}}$$

$$A_{18} = \frac{\left(2-\frac{2Rx^2}{r^3}+\frac{2R}{r}\right)zE}{\sqrt{\left(R+r\right)^2+z^2}}$$

$$A_{19} = \frac{z\left(R^2+r^2+2Rr+z^2\right)}{2r^4}\frac{\left(E-K\right)}{\left(\left(r+R\right)^2+z^2\right)^{5/2}} \times \left(B_1+B_{21}\right)$$

$$A_{20} = \frac{z\left(2xr+2Rx\right)}{4Rr^2}\sqrt{\left(R+r\right)^2+z^2}B_2\left(E-K\right)$$

$$A_{21} = -\frac{xz\left(\left(R+r\right)^2+z^2\right)^{3/2}B_2\left(E-K\right)}{8Rr^3}$$

$$A_{22} = \frac{z\left(\left(R+r\right)^2+z^2\right)^{5/2}B_2^2}{64R^2r^2B_{22}}\left(\frac{1}{8Rr}\left(E-K\right)-\frac{E-B_{22}K}{\left(R+r\right)^2+z^2}\right)$$

$$A_{23} = \frac{-3R^2+r^2-2z^2+\frac{2R^3}{\sqrt{r^2+z^2}}}{3z\sqrt{\left(R+r\right)^2+z^2}}(B_3+B_{27})\Pi_1$$

$$B_3 = 2 + \frac{x^2\left(R+r\right)}{\left(r^2+z^2\right)^{3/2}} - \frac{2x^2}{r\sqrt{r^2+z^2}} - \frac{R+r}{\sqrt{r^2+z^2}}$$

$$B_{27} = \frac{x^2\sqrt{r^2+z^2}}{r^3} - \frac{\sqrt{r^2+z^2}}{r} - \frac{Rx^2}{r^3} + \frac{R}{r}$$

$$A_{24} = \frac{\left(4x - \frac{4R^3x}{\left(r^2+z^2\right)^{3/2}}\right)B_{26}\Pi_1}{3z\sqrt{\left(R+r\right)^2+z^2}}$$

$$A_{25} = -\frac{2x\left(R+r\right)\left(-3R^2+r^2-2z^2+\frac{2R^3}{\sqrt{r^2+z^2}}\right)B_{26}\Pi_1}{3rz\left(\left(R+r\right)^2+z^2\right)^{3/2}}$$

$$A_{26} = \frac{\left(2 + \frac{6R^3x^2}{\left(r^2+z^2\right)^{5/2}} - \frac{2R^3}{\left(r^2+z^2\right)^{3/2}}\right)B_{25}\Pi_1}{3z\sqrt{\left(R+r\right)^2+z^2}}$$

$$A_{27} = -\frac{2x\left(R+r\right)\left(2x - \frac{2R^3x}{\left(r^2+z^2\right)^{3/2}}\right)B_{25}\Pi_1}{3rz\left(\left(R+r\right)^2+z^2\right)^{3/2}}$$

$$B_{25} = \left(r^2 + Rr + z^2 - \left(R+r\right)\sqrt{r^2+z^2}\right)$$

$$B_{26} = \left(2x + \frac{Rx}{r} - \frac{x\left(R+r\right)}{\sqrt{r^2+z^2}} - \frac{x\sqrt{r^2+z^2}}{r}\right)$$

$$A_{28} = \frac{x^2\left(R+r\right)^2\left(-3R^2+r^2-2z^2+\frac{2R^3}{\sqrt{r^2+z^2}}\right)B_{25}\Pi_1}{r^2z\left(\left(R+r\right)^2+z^2\right)^{5/2}}$$

$$A_{29} = -\frac{x^2\left(-3R^2+r^2-2z^2+\frac{2R^3}{\sqrt{r^2+z^2}}\right)B_{25}\Pi_1}{3r^2z\left(\left(R+r\right)^2+z^2\right)^{3/2}}$$

$$A_{30} = \frac{x^2\left(R+r\right)\left(-3R^2+r^2-2z^2+\frac{2R^3}{\sqrt{r^2+z^2}}\right)B_{25}\Pi_1}{3r^3z\left(\left(R+r\right)^2+z^2\right)^{3/2}}$$

$$A_{31} = -\frac{\left(R+r\right)\left(-3R^2+r^2-2z^2+\frac{2R^3}{\sqrt{r^2+z^2}}\right)B_{25}\Pi_1}{3rz\left(\left(R+r\right)^2+z^2\right)^{3/2}}$$

$$A_{32} = B_4B_5\left(\frac{x}{r^2}-\frac{\left(\frac{x}{r}+\frac{x}{\sqrt{r^2+z^2}}\right)}{r+\sqrt{r^2+z^2}}\right)\left(\frac{2r}{r+\sqrt{r^2+z^2}}E+B_6K+B_7\Pi_1\right)$$

$$B_4 = \frac{2\left(-3R^2+r^2-2z^2+\frac{2R^3}{\sqrt{r^2+z^2}}\right)}{\left(3z\sqrt{\left(R+r\right)^2+z^2}\right)}$$

$$B_5 = \frac{\left(2x+\frac{Rx}{r}-\frac{x(R+r)}{\sqrt{r^2+z^2}}-\frac{x\sqrt{r^2+z^2}}{r}\right)}{2B_6\left(-1+\frac{2r}{r+\sqrt{r^2+z^2}}\right)}$$

$$B_6 = \frac{4Rr}{\left(R+r\right)^2+z^2}-\frac{2r}{r+\sqrt{r^2+z^2}}$$

$$B_7 = -\frac{4Rr}{\left(R+r\right)^2+z^2}+\frac{4r^2}{\left(r+\sqrt{r^2+z^2}\right)^2}$$

$$A_{33} = B_4B_{26}\frac{B_2\left(\frac{E}{-1+\frac{4Rr}{(R+r)^2+z^2}}+\Pi_1\right)}{2B_6}$$

$$A_{34} = \frac{B_9 B_8}{2B_6}\left(\frac{E + \frac{1}{2r}\left(r+\sqrt{r^2+z^2}\right)B_6 K + \frac{1}{2r}\left(r+\sqrt{r^2+z^2}\right)B_7\Pi_1}{\left(-1+\frac{2r}{r+\sqrt{r^2+z^2}}\right)}\right)$$

$$A_{106} = \frac{B_9}{2B_6}B_2\left(\frac{E}{-1+\frac{4Rr}{(R+r)^2+z^2}}+\Pi_1\right)$$

$$B_8 = -\frac{2r\left(\frac{x}{r}+\frac{x}{\sqrt{r^2+z^2}}\right)}{\left(r+\sqrt{r^2+z^2}\right)^2}+\frac{2x}{r\left(r+\sqrt{r^2+z^2}\right)}$$

$$B_9 = \frac{r^2+Rr+z^2-(R+r)\sqrt{r^2+z^2}}{3z\sqrt{(R+r)^2+z^2}}\left(4x-\frac{4R^3x}{\left(r^2+z^2\right)^{3/2}}\right)$$

$$A_{35} = \frac{B_{10}B_8(E+\frac{1}{2r}\left(r+\sqrt{r^2+z^2}\right)B_6K+\frac{1}{2r}\left(r+\sqrt{r^2+z^2}\right)B_7\Pi_1)}{2B_6\left(-1+\frac{2r}{r+\sqrt{r^2+z^2}}\right)}$$

$$B_{10} = \frac{2x\left(R+r\right)\left(-3R^2+r^2-2z^2+\frac{2R^3}{\sqrt{r^2+z^2}}\right)B_{25}}{3rz\left(\left(R+r\right)^2+z^2\right)^{3/2}}$$

$$A_{36} = B_{10}\frac{B_2\left(\frac{E}{-1+\frac{4Rr}{(R+r)^2+z^2}}+\Pi_1\right)}{2B_6}$$

$$A_{37} = B_{11}\frac{B_2(B_2-B_8)}{2B_6^2}\left(\frac{E}{-1+\frac{4Rr}{(R+r)^2+z^2}}+\Pi_1\right)$$

$$A_{38} = \frac{B_{11}}{2B_6}\frac{4R(B_1+B_{21})}{r^3\left((r+R)^2+z^2\right)^3}\left(\frac{E}{-1+\frac{4Rr}{(R+r)^2+z^2}}+\Pi_1\right)$$

$$B_{11} = \frac{-3R^2 + r^2 - 2z^2 + \frac{2R^3}{\sqrt{r^2+z^2}}}{3z\sqrt{(R+r)^2 + z^2}} B_{25}$$

$$A_{39} = -B_{11} \frac{B_8^2 (E + \frac{1}{2r}\left(r + \sqrt{r^2+z^2}\right) B_6 K + \frac{1}{2r}\left(r + \sqrt{r^2+z^2}\right) B_7 \Pi_1)}{2B_6 \left(-1 + \frac{2r}{r+\sqrt{r^2+z^2}}\right)^2}$$

$$A_{40} = -B_{11} \frac{(B_2 - B_8) B_8 (E + \frac{1}{2r}\left(r + \sqrt{r^2+z^2}\right) B_6 K + \frac{1}{2r}\left(r + \sqrt{r^2+z^2}\right) B_7 \Pi_1)}{2B_6^2 \left(-1 + \frac{2r}{r+\sqrt{r^2+z^2}}\right)}$$

$$B_{12} = \frac{2}{r^3\left(r + \sqrt{r^2+z^2}\right)} \left(\frac{r^5\left(-1+4x^2\right) + r\left(-x^2 + r^2\left(-1+4x^2\right)\right) z^2}{\left(r^2+z^2\right)^{3/2}} \right)$$

$$B_{28} = \frac{2}{r^3\left(r + \sqrt{r^2+z^2}\right)} \left(r^2 - x^2 + 2r^2 x^2 + \frac{r^2\left(-1+2r^2\right) x^2}{r^2+z^2} \right)$$

$$A_{41} = B_{11}\left(B_{12} + B_{28}\right) \frac{E + \frac{1}{2r}\left(r + \sqrt{r^2+z^2}\right) B_6 K + \frac{1}{2r}\left(r + \sqrt{r^2+z^2}\right) B_7 \Pi_1}{2B_6 \left(-1 + \frac{2r}{r+\sqrt{r^2+z^2}}\right)}$$

$$A_{42} = -B_{11} B_2 \left(\frac{B_2 E}{B_{22}^2} - \frac{\left((R+r)^2 + z^2\right) B_2 \left(E - K\right)}{8 R r B_{22}} - \frac{B_2}{2B_6} \left(\frac{E}{-1 + \frac{4Rr}{(R+r)^2+z^2}} + \Pi_1 \right) \right)$$

$$A_{43} = B_{11} \frac{-B_2}{2B_6} \frac{B_8 \left(E + \frac{1}{2r}\left(r + \sqrt{r^2+z^2}\right) B_6 K + \frac{1}{2r}\left(r + \sqrt{r^2+z^2}\right) B_7 \Pi_1\right)}{2B_6 \left(-1 + \frac{2r}{r+\sqrt{r^2+z^2}}\right)}$$

$$A_{44} = \frac{B_{11} B_8}{2B_6 \left(-1 + \frac{2r}{r+\sqrt{r^2+z^2}}\right)} \frac{1}{8Rr} \left((R+r)^2 + z^2\right) B_2 \left(E - K\right)$$

$$A_{45} = \frac{B_{11}B_8}{2B_6\left(-1+\frac{2r}{r+\sqrt{r^2+z^2}}\right)}\frac{1}{2r}\left(r+\sqrt{r^2+z^2}\right)(B_2-B_8)\,K$$

$$A_{46} = \frac{B_{11}B_8}{2B_6\left(-1+\frac{2r}{r+\sqrt{r^2+z^2}}\right)}\frac{1}{2r}\left(\frac{x}{r}+\frac{x}{\sqrt{r^2+z^2}}\right)B_6K$$

$$A_{47} = -\frac{B_{11}B_8}{2B_6\left(-1+\frac{2r}{r+\sqrt{r^2+z^2}}\right)}\frac{1}{2r^3}x\left(r+\sqrt{r^2+z^2}\right)B_6K$$

$$A_{48} = \frac{B_{11}B_8}{2B_6\left(-1+\frac{2r}{r+\sqrt{r^2+z^2}}\right)}\frac{\left((R+r)^2+z^2\right)\left(r+\sqrt{r^2+z^2}\right)B_2B_6}{16Rr^2B_{22}}\left(E-B_{22}K\right)$$

$$A_{49} = \frac{B_{11}B_8\left(r+\sqrt{r^2+z^2}\right)}{2B_6\left(-1+\frac{2r}{r+\sqrt{r^2+z^2}}\right)}\frac{1}{2r}\left(-B_2-\frac{8r^2\left(\frac{x}{r}+\frac{x}{\sqrt{r^2+z^2}}\right)}{\left(r+\sqrt{r^2+z^2}\right)^3}+\frac{8x}{\left(r+\sqrt{r^2+z^2}\right)^2}\right)\Pi_1$$

$$A_{50} = \frac{B_{11}B_8}{2B_6\left(-1+\frac{2r}{r+\sqrt{r^2+z^2}}\right)}\frac{1}{2r}\left(\frac{x}{r}+\frac{x}{\sqrt{r^2+z^2}}\right)B_7\Pi_1$$

$$A_{51} = -\frac{B_{11}B_8}{2B_6\left(-1+\frac{2r}{r+\sqrt{r^2+z^2}}\right)}\frac{1}{2r^3}x\left(r+\sqrt{r^2+z^2}\right)B_7\Pi_1$$

$$A_{52} = B_{13}\left(\frac{B_8\left(E+\frac{1}{2r}\left(r+\sqrt{r^2+z^2}\right)B_6K+\frac{1}{2r}\left(r+\sqrt{r^2+z^2}\right)B_7\Pi_1\right)}{2B_6\left(-1+\frac{2r}{r+\sqrt{r^2+z^2}}\right)}\right)$$

$$A_{107} = \frac{B_{13}}{2B_6}B_2\left(\frac{E}{-1+\frac{4Rr}{(R+r)^2+z^2}}+\Pi_1\right)$$

$$B_{13} = \frac{B_{11}B_8}{2B_6\left(-1+\frac{2r}{r+\sqrt{r^2+z^2}}\right)}\frac{1}{2r}\left(r+\sqrt{r^2+z^2}\right)B_7$$

$$A_{53} = \frac{\left(3R^2-r^2+2z^2+\frac{2R^3}{\sqrt{r^2+z^2}}\right)B_3\Pi_2}{3z\sqrt{(R+r)^2+z^2}}$$

$$A_{54} = -\frac{\left(4x+\frac{4R^3x}{(r^2+z^2)^{3/2}}\right)\left(2x+\frac{Rx}{r}+\frac{x(R+r)}{\sqrt{r^2+z^2}}+\frac{x\sqrt{r^2+z^2}}{r}\right)\Pi_2}{3z\sqrt{(R+r)^2+z^2}}$$

$$A_{55} = -\frac{2x\,(R+r)\left(3R^2-r^2+2z^2+\frac{2R^3}{\sqrt{r^2+z^2}}\right)\left(2x+\frac{Rx}{r}+\frac{x(R+r)}{\sqrt{r^2+z^2}}+\frac{x\sqrt{r^2+z^2}}{r}\right)\Pi_2}{3rz\left((R+r)^2+z^2\right)^{3/2}}$$

$$A_{56} = \frac{\left(-2+\frac{6R^3x^2}{(r^2+z^2)^{5/2}}-\frac{2R^3}{(r^2+z^2)^{3/2}}\right)\left(r^2+Rr+z^2+(R+r)\sqrt{r^2+z^2}\right)\Pi_2}{3z\sqrt{(R+r)^2+z^2}}$$

$$A_{57} = -\frac{2x\,(R+r)\left(-2x-\frac{2R^3x}{(r^2+z^2)^{3/2}}\right)\left(r^2+Rr+z^2+(R+r)\sqrt{r^2+z^2}\right)\Pi_2}{3rz\left((R+r)^2+z^2\right)^{3/2}}$$

$$A_{58} = \frac{x^2\,(R+r)^2\left(3R^2-r^2+2z^2+\frac{2R^3}{\sqrt{r^2+z^2}}\right)\left(r^2+Rr+z^2+(R+r)\sqrt{r^2+z^2}\right)\Pi_2}{r^2z\left((R+r)^2+z^2\right)^{5/2}}$$

$$A_{59} = -\frac{x^2\left(3R^2-r^2+2z^2+\frac{2R^3}{\sqrt{r^2+z^2}}\right)\left(r^2+Rr+z^2+(R+r)\sqrt{r^2+z^2}\right)\Pi_2}{3r^2z\left((R+r)^2+z^2\right)^{3/2}}$$

$$A_{60} = \frac{x^2\,(R+r)\left(3R^2-r^2+2z^2+\frac{2R^3}{\sqrt{r^2+z^2}}\right)\left(r^2+Rr+z^2+(R+r)\sqrt{r^2+z^2}\right)\Pi_2}{3r^3z\left((R+r)^2+z^2\right)^{3/2}}$$

$$A_{61} = -\frac{(R+r)\left(3R^2 - r^2 + 2z^2 + \frac{2R^3}{\sqrt{r^2+z^2}}\right)\left(r^2 + Rr + z^2 + (R+r)\sqrt{r^2+z^2}\right)\Pi_2}{3rz\left((R+r)^2 + z^2\right)^{3/2}}$$

$$A_{62} = B_{14}\frac{B_8\left(E + \frac{1}{2r}\left(r - \sqrt{r^2+z^2}\right)B_6 K + \frac{1}{2r}\left(r - \sqrt{r^2+z^2}\right)B_7\Pi_2\right)}{2B_6\left(-1 + \frac{2r}{r-\sqrt{r^2+z^2}}\right)}$$

$$B_{14} = \frac{2\left(3R^2 - r^2 + 2z^2 + \frac{2R^3}{\sqrt{r^2+z^2}}\right)\left(2x + \frac{Rx}{r} + \frac{x(R+r)}{\sqrt{r^2+z^2}} + \frac{x\sqrt{r^2+z^2}}{r}\right)}{3z\sqrt{(R+r)^2 + z^2}}$$

$$A_{63} = B_{14}\frac{B_2}{2 - B_6}\left(\frac{E}{-1 + \frac{4Rr}{(R+r)^2+z^2}} + \Pi_2\right)$$

$$A_{64} = B_{15}\frac{B_2}{2 - B_6}\left(\frac{E}{-1 + \frac{4Rr}{(R+r)^2+z^2}} + \Pi_2\right)$$

$$A_{65} = B_{15}\frac{B_8\left(r - \sqrt{r^2+z^2}\right)}{2B_6\left(-1 + \frac{2r}{r-\sqrt{r^2+z^2}}\right)}\left(\frac{E}{r - \sqrt{r^2+z^2}} + \frac{1}{2r}B_6 K + \frac{1}{2r}B_7\Pi_2\right)$$

$$B_{15} = \frac{2\left(-2x - \frac{2R^3 x}{(r^2+z^2)^{3/2}}\right)\left(r^2 + Rr + z^2 + (R+r)\sqrt{r^2+z^2}\right)}{3z\sqrt{(R+r)^2 + z^2}}$$

$$A_{66} = B_{16}\frac{B_2}{2 - B_6}\left(\frac{E}{-1 + \frac{4Rr}{(R+r)^2+z^2}} + \Pi_2\right)$$

$$B_{16} = -\frac{2x\,(R+r)\left(3R^2 - r^2 + 2z^2 + \frac{2R^3}{\sqrt{r^2+z^2}}\right)\left(r^2 + Rr + z^2 + (R+r)\sqrt{r^2+z^2}\right)}{3rz\left((R+r)^2 + z^2\right)^{3/2}}$$

$$A_{67} = B_{17}\frac{B_8(E + \frac{1}{2r}\left(r - \sqrt{r^2+z^2}\right)B_6K + \frac{1}{2r}\left(r - \sqrt{r^2+z^2}\right)B_7\Pi_2)}{2B_6\left(-1 + \frac{2r}{r-\sqrt{r^2+z^2}}\right)}$$

$$A_{68} = -B_{17}\frac{B_2(B_8 - B_2)}{2B_6^2}\left(\frac{E}{-1 + \frac{4Rr}{(R+r)^2+z^2}} + \Pi_2\right)$$

$$B_{17} = \frac{\left(3R^2 - r^2 + 2z^2 + \frac{2R^3}{\sqrt{r^2+z^2}}\right)\left(r^2 + Rr + z^2 + (R+r)\sqrt{r^2+z^2}\right)}{3z\sqrt{(R+r)^2 + z^2}}$$

$$A_{69} = B_{17}\frac{4R}{r^3\left((r+R)^2 + z^2\right)^3}\frac{B_1 + B_{21}}{2B_6}\left(\frac{E}{-1 + \frac{4Rr}{(R+r)^2+z^2}} + \Pi_2\right)$$

$$A_{70} = -B_{17}\frac{B_8^2\left(E + \frac{1}{2r}\left(r - \sqrt{r^2+z^2}\right)B_6K + \frac{1}{2r}\left(r - \sqrt{r^2+z^2}\right)B_7\Pi_2\right)}{2B_6\left(1 - \frac{2r}{r-\sqrt{r^2+z^2}}\right)^2}$$

$$A_{71} = B_{17}\frac{(B_8 - B_2)B_8\left(E + \frac{1}{2r}\left(r - \sqrt{r^2+z^2}\right)B_6K + \frac{1}{2r}\left(r - \sqrt{r^2+z^2}\right)B_7\Pi_2\right)}{2B_6^2\left(-1 + \frac{2r}{r-\sqrt{r^2+z^2}}\right)}$$

$$B_{18} = -\frac{2\left(r^5 + r^3z^2 + rx^2z^2 + r^4\sqrt{r^2+z^2} + r^2z^2\sqrt{r^2+z^2} - x^2z^2\sqrt{r^2+z^2}\right)}{r^3\left(r^2+z^2\right)^{3/2}\left(-r + \sqrt{r^2+z^2}\right)}$$

$$A_{72} = \frac{B_{18}\left(E + \frac{1}{2r}\left(r - \sqrt{r^2+z^2}\right)B_6K + \frac{1}{2r}\left(r - \sqrt{r^2+z^2}\right)B_7\Pi_2\right)}{2B_6\left(-1 + \frac{2r}{r-\sqrt{r^2+z^2}}\right)}$$

$$A_{73} = -B_{17}\frac{B_2}{2B_6}\frac{B_2E}{B_{22}^2}$$

$$A_{74} = -B_{17}\frac{B_2}{2B_6}\frac{\left((R+r)^2+z^2\right)B_2\left(E-K\right)}{8RrB_{22}}$$

$$A_{75} = B_{17}\left(\frac{B_2}{2B_6}\right)^2\left(\frac{E}{-1+\frac{4Rr}{(R+r)^2+z^2}}+\Pi_2\right)$$

$$A_{76} = B_{17}\frac{B_2}{2B_6}\frac{B_8\left(E+\frac{1}{2r}\left(r-\sqrt{r^2+z^2}\right)B_6K+\frac{1}{2r}\left(r-\sqrt{r^2+z^2}\right)B_7\Pi_2\right)}{2B_6\left(-1+\frac{2r}{r-\sqrt{r^2+z^2}}\right)}$$

$$A_{77} = B_{17}B_8\frac{1}{8Rr}\left((R+r)^2+z^2\right)B_2\left(E-K\right)$$

$$A_{78} = B_{17}B_8\frac{1}{2r}\left(r-\sqrt{r^2+z^2}\right)(B_2+\frac{2r\left(\frac{x}{r}-\frac{x}{\sqrt{r^2+z^2}}\right)}{\left(r-\sqrt{r^2+z^2}\right)^2}-\frac{2x}{r\left(r-\sqrt{r^2+z^2}\right)})K$$

$$A_{79} = B_{17}B_8\frac{1}{2r}\left(\frac{x}{r}-\frac{x}{\sqrt{r^2+z^2}}\right)B_6K$$

$$A_{80} = -B_{17}B_8\frac{1}{2r^3}x\left(r-\sqrt{r^2+z^2}\right)B_6K$$

$$A_{81} = B_{17}B_8\frac{\left((R+r)^2+z^2\right)\left(r-\sqrt{r^2+z^2}\right)B_2B_6\left(E-B_{22}K\right)}{16Rr^2B_{22}}$$

$$A_{82} = B_{17}B_8\frac{1}{2r}\left(r-\sqrt{r^2+z^2}\right)B_{19}\Pi_2$$

$$B_{19} = \frac{8Rx\left(R+r\right)}{\left(\left(R+r\right)^2+z^2\right)^2} - \frac{4Rx}{r\left(\left(R+r\right)^2+z^2\right)} - \frac{8r^2\left(\frac{x}{r}-\frac{x}{\sqrt{r^2+z^2}}\right)}{\left(r-\sqrt{r^2+z^2}\right)^3} + \frac{8x}{\left(r-\sqrt{r^2+z^2}\right)^2}$$

$$A_{83} = B_{17}B_8\frac{1}{2r}\left(\frac{x}{r}-\frac{x}{\sqrt{r^2+z^2}}\right)B_7\Pi_2$$

$$A_{84} = -B_{17}B_8\frac{1}{2r^3}x\left(r-\sqrt{r^2+z^2}\right)B_7\Pi_2$$

$$A_{85} = B_{17}B_8\frac{1}{2r}\left(r-\sqrt{r^2+z^2}\right)B_7\frac{B_2}{2B_6}\left(\frac{E}{-1+\frac{4Rr}{\left(R+r\right)^2+z^2}}+\Pi_2\right)$$

$$A_{86} = B_{23}\left(\frac{E}{\left(r-\sqrt{r^2+z^2}\right)}+\frac{1}{2r}B_6K+\frac{1}{2r}B_7\Pi_2\right)$$

$$B_{23} = \frac{B_8\left(r-\sqrt{r^2+z^2}\right)^2B_7}{2B_6\left(-1+\frac{2r}{r-\sqrt{r^2+z^2}}\right)}\frac{B_{17}}{2r}\frac{B_8}{2B_6\left(-1+\frac{2r}{r-\sqrt{r^2+z^2}}\right)}$$

$$A_{87} = B_{20}\frac{B_2(B_2-B_8)}{2-B_6^2}\left(\frac{E}{-1+\frac{4Rr}{\left(R+r\right)^2+z^2}}+\Pi_1\right)$$

$$B_{20} = \frac{\left(-3R^2+r^2-2z^2+\frac{2R^3}{\sqrt{r^2+z^2}}\right)B_{25}}{3z\sqrt{\left(R+r\right)^2+z^2}}$$

$$A_{88} = B_{20}\frac{4R}{(2-B_6)r^3\left((r+R)^2+z^2\right)^3}(B_1+B_{21})(\frac{E}{-1+\frac{4Rr}{\left(R+r\right)^2+z^2}}+\Pi_1)$$

$$A_{89} = -\frac{B_{20}B_8^2\left(r+\sqrt{r^2+z^2}\right)}{2B_6\left(-1+\frac{2r}{r+\sqrt{r^2+z^2}}\right)^2}\left(\frac{E}{\left(r+\sqrt{r^2+z^2}\right)}+\frac{1}{2r}B_6K+\frac{1}{2r}B_7\Pi_1\right)$$

$$A_{90} = \frac{B_{20}(B_8-B_2)B_8\left(r+\sqrt{r^2+z^2}\right)}{2B_6^2\left(-1+\frac{2r}{r+\sqrt{r^2+z^2}}\right)}\left(\frac{E}{\left(r+\sqrt{r^2+z^2}\right)}+\frac{1}{2r}B_6K+\frac{1}{2r}B_7\Pi_1\right)$$

$$A_{91} = \frac{B_{18}B_{20}\left(r+\sqrt{r^2+z^2}\right)}{2B_6\left(-1+\frac{2r}{r+\sqrt{r^2+z^2}}\right)}\left(\frac{E}{\left(r+\sqrt{r^2+z^2}\right)}+\frac{1}{2r}B_6K+\frac{1}{2r}B_7\Pi_1\right)$$

$$A_{92} = -\frac{B_{20}B_2^2E}{B_{22}^2}$$

$$A_{93} = -B_{20}B_2\frac{\left(\left((R+r)^2+z^2\right)B_2\left(E-K\right)\right)}{8RrB_{22}}$$

$$A_{94} = B_{20}B_2\frac{B_2}{2-B_6}\left(\frac{E}{-1+\frac{4Rr}{(R+r)^2+z^2}}+\Pi_1\right)$$

$$A_{95} = \frac{B_{20}B_2}{2-B_6}\frac{B_8\left(r+\sqrt{r^2+z^2}\right)}{2B_6\left(-1+\frac{2r}{r+\sqrt{r^2+z^2}}\right)}\left(\frac{E}{\left(r+\sqrt{r^2+z^2}\right)}+\frac{1}{2r}B_6K+\frac{1}{2r}B_7\Pi_1\right)$$

$$A_{96} = B_{20}\frac{B_8}{2B_6\left(-1+\frac{2r}{r+\sqrt{r^2+z^2}}\right)}\frac{1}{8Rr}\left((R+r)^2+z^2\right)B_2\left(E-K\right)$$

$$A_{97} = \frac{B_8B_{20}}{2B_6\left(-1+\frac{2r}{r+\sqrt{r^2+z^2}}\right)}\frac{1}{2r}\left(r+\sqrt{r^2+z^2}\right)(B_2-B_8)K$$

$$A_{98} = \frac{B_8 B_{20}}{2B_6\left(-1+\frac{2r}{r+\sqrt{r^2+z^2}}\right)}\frac{1}{2r}\left(\frac{x}{r}+\frac{x}{\sqrt{r^2+z^2}}\right)B_6 K$$

$$A_{99} = -\frac{B_8 B_{20}}{2B_6\left(-1+\frac{2r}{r+\sqrt{r^2+z^2}}\right)}\frac{1}{2r^3}x\left(r+\sqrt{r^2+z^2}\right)B_6 K$$

$$A_{100} = \frac{B_8 B_{20}\left(r+\sqrt{r^2+z^2}\right)}{2B_6\left(-1+\frac{2r}{r+\sqrt{r^2+z^2}}\right)}\frac{B_2 B_6\left((R+r)^2+z^2\right)}{16Rr^2 B_{22}}\left(E-B_{22}K\right)$$

$$A_{101} = \frac{B_8 B_{20}\left(r+\sqrt{r^2+z^2}\right)}{4rB_6\left(-1+\frac{2r}{r+\sqrt{r^2+z^2}}\right)}\left(-B_2-\frac{8r^2\left(\frac{x}{r}+\frac{x}{\sqrt{r^2+z^2}}\right)}{\left(r+\sqrt{r^2+z^2}\right)^3}+\frac{8x}{\left(r+\sqrt{r^2+z^2}\right)^2}\right)\Pi_1$$

$$A_{102} = \frac{B_8 B_{20}}{2B_6\left(-1+\frac{2r}{r+\sqrt{r^2+z^2}}\right)}\frac{1}{2r}\left(\frac{x}{r}+\frac{x}{\sqrt{r^2+z^2}}\right)B_7\Pi_1$$

$$A_{103} = -\frac{B_8 B_{20}}{2B_6\left(-1+\frac{2r}{r+\sqrt{r^2+z^2}}\right)}\frac{1}{2r^3}x\left(r+\sqrt{r^2+z^2}\right)B_7\Pi_1$$

$$A_{104} = B_{24}\frac{B_2}{2-B_6}\left(\frac{E}{-1+\frac{4Rr}{(R+r)^2+z^2}}+\Pi_1\right)$$

$$A_{105} = B_{24}B_8\left(E+\frac{1}{2r}\left(r+\sqrt{r^2+z^2}\right)B_6 K+\frac{1}{2r}\left(r+\sqrt{r^2+z^2}\right)B_7\Pi_1\right)$$

$$B_{24} = \frac{B_8 B_{20}}{2B_6\left(-1+\frac{2r}{r+\sqrt{r^2+z^2}}\right)}\frac{1}{2r}\frac{\left(r+\sqrt{r^2+z^2}\right)B_7}{2B_6\left(-1+\frac{2r}{r+\sqrt{r^2+z^2}}\right)}$$

Appendix C

The Fokker Planck of the dissipative classical system and its relation to a Quantum Hamiltonian

In what follows, we highlight features of the mapping (1; 2; 3) between classical dissipative systems and bosonic systems. We first set the preliminaries following (2). Given the initial value of $x(t)$ at time $t = t_0$, the time dependent probability distribution $\mathcal{P}(x, t; x_0, t_0)$ for the stochastic vector $x(t)$ is given by

$$\mathcal{P}(x, t; x_0, t_0) = \langle \prod_{i=1}^{N} \delta[x_i(t) - x_i] \rangle_{\eta, x_0} \tag{C.1}$$

where $\langle - \rangle_{\eta,x_0}$ denotes the average over the noise given the initial conditions at time $t = t_0$. The average of a general function $\mathcal{O}(x(t))$ is then

$$\int dx \mathcal{P}(x,t;x_0,t_0)\mathcal{O}(x) = \langle \mathcal{O}(x(t)) \rangle_{\eta,x_0}. \tag{C.2}$$

It is convenient to write $\mathcal{P}(x,t;x_0,t_0)$ in a Dirac notation as

$$\mathcal{P}(x,t;x_0,t_0) = \langle x|\hat{P}(t,t_0)|x_0\rangle. \tag{C.3}$$

Time translation invariance and the Markov property of P,

$$\begin{aligned} &\int dx'^N \langle x|\hat{P}(t,t')|x'\rangle\langle x'|\hat{P}(t',t_0)|t_0\rangle \\ &= \int dx'^N \mathcal{P}(x,t;x',t')\mathcal{P}(x',t';x_0,t_0) \\ &= \mathcal{P}(x,t;x_0,t_0) \end{aligned} \tag{C.4}$$

imply that

$$\hat{P}(t,t_0) = \mathcal{T} e^{-\int_{t_0}^{t} H_{FP}(t')dt'} \tag{C.5}$$

with an operator H_{PF} a "Fokker-Planck" Hamiltonian and $\mathcal{T}$ is the time ordered operator. We now return to our particular classical to quantum mapping The summary below closely follows this mapping as presented by Biroli et al. (3). In what follows, we set $P = \hat{P}(t,t_0)|x_0\rangle$. For the classical dissipative system of Eq. (6.3), the

probability distribution $P(\{\vec{x}\})$ evolves according to the Fokker-Planck equation

$$\frac{\partial P}{\partial t} = -H_{FP} P, \tag{C.6}$$

where the Fokker Planck operator is

$$H_{FP} = -\sum_i \frac{1}{\gamma_i} \frac{\partial}{\partial \vec{x}_i} \left[\nabla_i V_{\mathsf{N}} + T \frac{\partial}{\partial \vec{x}_i} \right]. \tag{C.7}$$

Eq. (C.7) follows from a direct differentiation of Eq. (C.1) while invoking Eq. (6.3) for the derivatives of the coordinates $x_i(t)$ in the argument of the delta functions. The operator H_{FP} is non-Hermitian and for each eigenvalue generally has different left and right eigenvectors. The Fokker-Planck equation can be mapped into a Hermitian Hamiltonian by (4)

$$H = e^{V_{\mathsf{N}}/(2T)} H_{FP} e^{-V_{\mathsf{N}}/(2T)}. \tag{C.8}$$

A direct substitution leads to the quantum many body Hamiltonian of Eq. (6.4). Note that V_{N} is, thus far, completely general. This potential energy may include one body interactions (i.e., coupling to an external source), pair interactions between particles, and three- and higher-order particle interactions.

We consider what specifically occurs when the classical potential energy in Eq. (6.3) is the sum of pair interactions,

$$V_{\mathsf{N}}(\{\vec{x}\}) = \frac{1}{2} \sum_{i \neq j} V_{ij}(\vec{x}_i - \vec{x}_j). \tag{C.9}$$

For such systems, the quantum many body Hamiltonian of Eq. (6.4) explicitly contains an effective potential which is the sum of two and three body interactions,

$$\begin{aligned}\mathcal{V}_{\mathsf{Quantum}}(\{\vec{x}\}) = \sum_i \frac{1}{\gamma_i}\left[-\frac{1}{2}\nabla_i^2 V_{\mathsf{N}} + \frac{1}{4T}(\nabla_i V_{\mathsf{N}})^2\right] \\ = -\frac{1}{2}\sum_{i\neq j}\frac{1}{\gamma_i}\nabla^2 V_{ij}(\vec{x}_i - \vec{x}_j) \\ +\frac{1}{4T_{cl}}\sum_{i;j\neq i;j'\neq i}\left[\frac{1}{\gamma_1}\vec{\nabla}_i V_{ij}(\vec{x}_i - \vec{x}_j)\right. \\ \left.\cdot\vec{\nabla}_i V_{ij'}(\vec{x}_i - \vec{x}_{j'})\right]. \qquad \text{(C.10)}\end{aligned}$$

For a given classical two body potential in d dimensions which is both translationally and rotationally invariant, $V(\vec{x}) = V(|\vec{x}|)$, the resulting quantum potential energy (3)

$$\begin{aligned}\mathcal{V}_{\mathsf{Quantum}}(\{\vec{x}\}) &= \frac{1}{2}\sum_{i\neq j} v^{pair}_{\mathsf{Quantum}}(\vec{x}_i - \vec{x}_j) \\ &\quad + \sum_{i;j\neq i;j'\neq i} v^{3-body}_{\mathsf{Quantum}}(\vec{x}_i - \vec{x}_j, \vec{x}_i - \vec{x}_{j'}); \\ v^{pair}(\vec{x}) &= -\nabla^2 V(\vec{x}) + \frac{1}{2}[\nabla V(\vec{x})]^2 \\ &= -\frac{d-1}{r}V'(r) - V''(r) + \frac{1}{2}[V'(r)]^2; \\ v^{3-body}(x, x') &= \frac{1}{4}\nabla V(x)\cdot\nabla V(\vec{x}') \\ &= \frac{1}{4}\frac{\vec{x}}{r}\cdot\frac{\vec{x}'}{r'}V'(r)V'(r'), \qquad \text{(C.11)}\end{aligned}$$

with $r = |\vec{x}|$. For a classical potential $V(r) = V_0\exp(-\lambda[(r/\sigma)^2 - 1])$ the corresponding

pair term in Eq. (C.11) is

$$v^{pair}(r) = [2\lambda d - 4\lambda^2 r^2]V(r) + 2\lambda^2 r^2[V(r)]^2. \tag{C.12}$$

In the limit $\lambda \to \infty$, the classical system corresponds to a hard sphere system with a σ the hard sphere radius and the quantum potential of Eq. (C.12) similarly exhibits a dominant hard sphere repulsion (augmented by an attractive potential at the sphere boundaries that is of range $1/\lambda$).

For general $V_{\mathsf{N}}(\{\vec{x}\})$, the Fokker-Planck operator of Eq. (C.7) has non-negative eigenvalues (1; 2). The zero eigenvalue state—i.e., the ground state—which according to Eq. (C.6) corresponds to a stationary (time independent) probability distribution P. This is the equilibrium Boltzmann distribution

$$P^{equil}(\{x\}, t) = \frac{1}{Z_N} e^{-\beta V_{\mathsf{N}}(\{x\})}, \tag{C.13}$$

with Z_N the partition function associated with $V_{\mathsf{N}}(\{\vec{x}\})$ as is readily rationalized by the following argument. For a finite size system, the linear eigenvalue equation

$$(H_{FP})_{bc} P_c = -\varepsilon_c P_c, \tag{C.14}$$

with the matrix row/column indices b and c denoting classical configurations, has a (finite size) matrix H_{FP} that has positive off-diagonal elements and negative diagonal entries. Specifically, in Eqs. (C.6,C.14), the transition matrix H_{FP} has entries that

relate the probabilities of going from state b to state c in a given (infinitesimal) time interval. If these states are different ($b \neq c$) then clearly $(H_{FP})_{bc} > 0$. The diagonal elements $(H_{FP})_{bb}$ provide the probabilities of "leaking out" of state b and going to all other states $c \neq b$. From all of this it follows that

$$(H_{FP})_{bb} = -\sum_{b' \neq b} (H_{FP})_{bb'} < 0. \tag{C.15}$$

Detailed balance, i.e., that fact that the probability of going from b to c is same as that of going from c to b asserts that

$$(H_{FP})_{bc} e^{-\beta E_b} = (H_{FP})_{cb} e^{-\beta E_c}. \tag{C.16}$$

In this classical system of Eq. (6.3), the energies of the classical states E_c are simply given by $V_{\mathsf{N}}(\{\vec{x}\})$ evaluated for the classical configurations c. With the aid of Eqs. (C.15, C.16), it is easy to see that the column vector $P_c^{equil} = Z_N^{-1} \exp(-\beta E_c)$ (i.e., the distribution of Eq. (C.13)) is a null eigenvector of Eq. (C.14). This probability eigenvector corresponds, of course, the equilibrium Boltzmann distribution. The factor of Z_N^{-1} is inserted to ensure normalization of the classical probabilities (for any eigenstate): $\sum_c P_c = 1$. Now, we can add a constant to the finite dimensional matrix

$$H_{FP} \rightarrow H_{FP} - const. \equiv H_{FP}^{'} \tag{C.17}$$

to generate a matrix $(-H_{FP}^{'})$ that has all of its elements positive $(-H_{FP}^{'})_{bc} > 0$.

Specifically, to this end, in Eq. (C.17 we can chose *const.* to be any constant larger than the sign inverted smallest off-diagonal element of $(-H_{FP})$, i.e., $const. > -\min_{b\neq c}\{H_{FP}\}_{bc}$. For such a positive matrix, we can apply the Perron-Frobenius theorem which states that the largest eigenvector of $(-H^{'}_{FP})$ is non-degenerate and that eigenvector is the only eigenvector that has all of its elements positive with all other orthogonal eigenvectors having at least one negative element. Clearly, all of the eigenvectors of H_{FP} and $H^{'}_{FP}$ are identical with the corresponding eigenvectors of both operators merely shifted uniformly by *const.*. With all of the above in tow, we see that P^{equil} corresponds to the largest eigenvector of $(-H^{'}_{FP})$ and is thus also the largest eigenvector of $(-H_{FP})$. As P^{equil} was the null eigenvector of H_{FP}, it follows that all other eigenvalues of Eq. (C.14), $\varepsilon > 0$, are positive and, according to Eq. (C.6) and explicit earlier discussions evolve with time as $\exp(-\varepsilon t) \rightarrow_{t\rightarrow\infty} 0$. Thus, physically (as it to be expected) at long times the system attains its equilibrium configuration of P^{equil}. In the corresponding zero-temperature quantum problem, the dominant classical equilibrium state with a lowest energy. We will thus label it in Appendix E by $|G\rangle$. The transformation of Eq. (C.8) relates the operators in the classical Fokker-Planck and zero temperature quantum problem to one another. The transformation for the right eigenvectors P of H_{FP}, which we explicitly denote below as $|-\rangle_{FP}$, to the eigenvectors of the quantum Hamiltonian H is trivially

$$|-\rangle_{FP} \rightarrow \exp(-V_{\mathsf{N}}/(2T)))|-\rangle_{FP} = |-\rangle_{Quantum}. \tag{C.18}$$

Similarly, the left eigenvectors ($\langle -|_{FP}$) of H_{FP} are to be multiplied by $\exp(V_{\mathsf{N}}/(2T))$) in order to pass to left eigenstates the quantum problem. (In the quantum problem defined by H, the left and right eigenstates are trivially related to each other by Hermitian conjugation.) Applying Eq. (C.18) to the null right eigenstate of the Fokker Planck Hamiltonian of Eq. (C.13), we see that the quantum eigenstate of H corresponding to this classical equilibrium state is given by

$$\Psi_0(\{\vec{x}\}) = \frac{1}{\sqrt{Z_N}} \exp(-\frac{1}{2T} V_{\mathsf{N}}(\{\vec{x}\})). \tag{C.19}$$

The prefactor in Eq. (C.19) is set by the normalization of this quantum state. When comparing Eqs. (C.13,C.19) to one another, we see that this wavefunction is related to the classical equilibrium probability eigenvector by the appealing relation $\Psi_0(\{\vec{x}\}) = \sqrt{P^{equil}(\{\vec{x}\})}$ .When $V_{\mathsf{N}}(\{\vec{x}\}))$ is symmetric under the interchange of particle coordinates, the resulting wavefunction may describe bosons. For a classical potential which is the sum of pair potentials, a substitution of Eq. (C.9) into Eq. (C.19) leads to a Jastrow type wavefunction.

Bibliography

[1] G. Parisi, *Statistical Field Theory*, (Addison Wesley, New York, 1988).

[2] J. Zinn-Justin, *Quantum Field Theory and Critical Phenomena*, (Oxford University Press, 2002).

[3] G. Biroli, C. Chamon, and F. Zamponi, Phys. Rev. B **78**, 224306 (2008).

[4] B. U. Felderhof, Reports Math. Phys. **1**, 215 (1970); B. U. Felderhof and M. Suzuki, Physica **56**, 43 (1971)

Appendix D

Simple examples of classical to quantum correspondence and some aspects

D.0.1 Free particles

For a single free quantum particle ($\mathcal{V}_{\mathsf{Quantum}} = 0$ in Eq. (6.4)) in d spatial dimensions.

In what follows we consider two cases:

Zero energy bound state

For a short range attractive potential the zero energy eigenstate outside the potential, up to volume normalization factors, given by

$$\Psi_0(\vec{x}) = \frac{A}{|\vec{x}|^{d-2}}. \tag{D.1}$$

Invoking Eq. (C.19), we see that, in this case,

$$V_{\mathsf{N}}^{\mathsf{free}}(\{\vec{x}\}) = 2T(d-2)\ln|\vec{x}|. \tag{D.2}$$

Indeed substituting Eq. (D.2) into Eq. (6.4) and recalling that, in its scalar "S-wave" (or "$\ell = 0$") representation, the Laplacian is given by $\nabla^2 = \frac{d^2}{dr^2} + \frac{d-1}{r}\frac{d}{dr}$, it is readily verified, as it must self-consistently be, that the corresponding quantum potential $\mathcal{V}_{\mathsf{Quantum}} = 0$ in the region outside the range of the interaction.

Completely free particle

The case of a system with a zero potential everywhere, the wave-function is a constant in real space. By Eq.(C.19), the classical potential energy vanishes everywhere. By Eq. (6.4), the same also occurs for the quantum potential which is everywhere zero.

D.0.2 Localization and delocalization

A general localization in the quantum problem will appear whenever a corresponding one occurs in the classical system. That is, if

$$h(R) = \frac{\int_{r>R} d^d x e^{-\beta V_{\mathsf{N}}(\{\vec{x}\})}}{\int d^d x e^{-\beta V_{\mathsf{N}}(\{\vec{x}\})}} \tag{D.3}$$

tends to zero in the limit of large R, i.e., $\lim_{R\to\infty} h(R) = 0$ then a localized state is present. From Eqs. (C.12,C.19), in a system with pair interactions, a localized ground state may appear only if

$$\lim_{r\to\infty} \frac{dv^{pair}(r)}{dr} > 0. \tag{D.4}$$

D.0.3 Scaling invariance of time and space

As is well known, for a homogeneous classical potential $V_{\mathsf{N}}(\{\vec{x}\})$ which scales as a power (say, p) of the spatial coordinates $|\vec{x}|$, the equations of motion are invariant under a simultaneous rescaling of the time coordinates. This analysis is typically done for inertial systems. When replicated for the over damped system of Eq. (6.3), we find that

$$\vec{x}_i \to a\vec{x}_i,\ t \to bt, \tag{D.5}$$

where b plays the role of λ and a plays the role of $\lambda^{1/z}$ from before, leads to an invariance of Eq. (6.3) if $b = a^{2-p}$. By contrast, in the corresponding quantum problem of the Schrödinger equation with the Hamiltonian of Eq. (6.4), a scaling such as that of Eq.(D.5) is possible only for a single case: that of a potential $V_{\mathsf{N}}(\{\vec{x}\})$ that is a logarithmic function of its arguments (or a constant). For this particular case, we find that $b = a^2$. Correspondingly, akin to subsection D.0.1, for this particular case, the time scales as $t \sim |x|^2$ as in diffusion or the free particle quantum problem.

D.0.4 Relation between the classical and quantum potentials and Eikonal approximation to the Schrödinger equation

Below we briefly review the eikonal approximation and then discuss its relation to the connection between the classical and quantum many body potentials as seen in Eqs. (6.4, C.19).

We write the wavefunction as a function of only the phase (the eikonal approximation) where, as throughout, we set $\hbar = 1$.

$$\Psi_0 = Ae^{iS} \tag{D.6}$$

and substitute this into the Schrödinger equation with the Hamiltonian in the second

line of Eq. (6.4) then we have

$$\frac{1}{2m}\sum_i(\nabla_i S)^2 + \mathcal{V}_{\mathsf{Quantum}}(\{\vec{x}\}) + \frac{\partial S}{\partial t} = \frac{i}{2m}\sum_i \nabla_i^2 S. \tag{D.7}$$

For time independent solutions, $\frac{\partial S}{\partial t} = 0$ and from Eq. (D.7) trivially becomes

$$\mathcal{V}_{\mathsf{Quantum}}(\{\vec{x}\}) = \sum_i [\frac{i}{2m}\nabla_i^2 S - \frac{1}{2m}(\nabla_i S)^2]. \tag{D.8}$$

If we now make the correspondence $iS \leftrightarrow -\beta V_{\mathsf{N}}/2$ then Eq. (D.6) becomes Eq. (C.19) and correspondingly Eq. (D.8) becomes Eq. (6.4) relating the quantum potential energy $\mathcal{V}_{\mathsf{Quantum}}$ to the classical potential energy V_{N}.

Appendix E

Derivation of the quantum to classical correspondence for general two operator correlators

The central role of this appendix is the derivation of Eqs.(E.22,6.8) (or, more precisely, the derivation of Eqs. (E.17, E.21) that lead to Eq. (E.22) and Eqs. (6.6,6.7) that lead to Eq. (6.8)). The sole assumption made in the below derivation of Eqs. (E.17, E.21, E.22) is that the classical system starts from its equilibrium state and then evolved with some general (time dependent) potential $V_{\mathsf{N}}(t)$. This will be mapped onto analytic continuations of the correlation and response functions of a quantum system that starts at time $t = 0$ in its ground state of Eq. (C.19) and then evolved with the corresponding (time dependent) Hamiltonian $H(t)$. It is important to emphasize that we make no assumptions regarding the final (and

intermediate) states. The classical (quantum) system need not stay in equilibrium (or ground state) as it evolves in time. In Eqs. (6.6,6.7,E.22) we elaborate on the consequences for a time independent Hamiltonian.

Before detailing the derivation, we we collect basic relations discussed in Appendix C with several new definitions,

$$P(\{x\},t) = \langle\{x\}|P(t)\rangle, \tag{E.1}$$

$$P_G(\{x\},t) = \langle\{x\}|G\rangle = \frac{e^{-V_{\mathsf{N}}(\{x\})/T}}{Z_N}, \tag{E.2}$$

$$H_{FP}|G\rangle = 0, \tag{E.3}$$

$$\langle +|\{x\}\rangle = 1, \tag{E.4}$$

$$H = e^{V_{\mathsf{N}}/2T} H_{FP} e^{-V_{\mathsf{N}}/2T}. \tag{E.5}$$

These will serve as a point of departure for the calculations in this appendix.

Equation (E.1) represents a general probability distribution in bra-ket notation. Equation (E.2) defines the ground state distribution as a Boltzmann distribution in bra-ket notation. Equation (E.3) defines the ground state as the eigenvector of the Fokker-Planck Hamiltonian with zero eigenvalue. Equation (E.4) defines the state $|+\rangle$ to be the uniform state such that $|+\rangle = \int d\{x\}|+\rangle$. Equation (E.5) can be used to find a relationship between H_{FP} and $H_{FP}^{\dagger}$.

As H is Hermitian,

$$H^\dagger = e^{-V_N/2T} H_{FP}^\dagger e^{V_N/2T} = H = e^{V_N/2T} H_{FP} e^{-V_N/2T}. \tag{E.6}$$

Left multiplying by $e^{V_N/2T}$ and right multiplying by $e^{-V_N/2T}$ gives the relation,

$$H_{FP}^\dagger = e^{V_N/T} H_{FP} e^{-V_N/T}. \tag{E.7}$$

Before detailing the mapping, one must first prove that the state $|+\rangle$ is a left eigenstate of the Fokker-Planck Hamiltonian with zero eigenvalue. Beginning with a simple extension of the definition of the ground state,

$$H_{FP}|G\rangle = 0 \rightarrow \langle G|H_{FP}^\dagger = 0. \tag{E.8}$$

As shown in Equation (E.7), this is equivalent to

$$\langle G|e^{V_N/T} H_{FP} e^{-V_N/T} = 0, \tag{E.9}$$

which (from Eqs.(E.2, E.4)) implies that

$$Z_N^{-1}\langle +|H_{FP}e^{-V_N/T} = 0. \tag{E.10}$$

This illustrates that the uniform state is a left eigenvalue of the Fokker-Planck Hamiltonian with zero eigenvalue (i.e., $\langle +|H_{FP} = 0$). Note that this uniform state is a left null eigenstate for all Fokker-Planck Hamiltonians.

We will now illustrate our central result of Eq. (6.8). Towards this end, we write anew the classical correlation function of Eq. (6.5),

$$G_{\mathsf{classical}}(t) = \langle \mathcal{O}_1(t)\mathcal{O}_2(0)\rangle. \tag{E.11}$$

By Bayes' theorem, the joint probability distribution, $P(\{x\},\{y\}) = P(\{x\}|\{y\})P(\{y\})$, the probability of finding coordinates $\{x\}$ at time t and coordinates $\{y\}$ at time 0 is given by product the conditional probability of finding $\{x\}$ at time t given $\{y\}$ at time 0 with the probability of attaining $\{y\}$ at time $t = 0$. As discussed in Appendix C), the ground state has a probability distribution given by a Boltzmann distribution $Z_N^{-1}e^{-\beta U_N(\{y\})}$ [see Eq. (E.2)]. The conditional probability $P(\{x\}|\{y\})$ can be expressed in terms of the matrix element of $\mathcal{T}e^{-\int_0^t H_{FP}(t')dt'}$ (where $\mathcal{T}$ is the time ordering operator) as this conditional P satisfies Eq. (C.6). This implies the form of the expectation value of Eq. (E.11),

$$\begin{aligned} G_{\mathsf{classical}}(t) &= \int d\{x\}d\{y\}\mathcal{O}_1 P(\{x\},\{y\})\mathcal{O}_2 \\ &= \int d\{x\}d\{y\}\mathcal{O}_1 P(\{x\}|\{y\})\mathcal{O}_2 P(\{y\}) \\ = \int d\{x\}d\{y\}\mathcal{O}_1\langle\{x\}|\mathcal{T}e^{-\int_0^t H_{FP}(t')dt'}|\{y\}\rangle\mathcal{O}_2&\frac{e^{-\beta V_{\mathsf{N}}(\{y\})}}{Z_N}. \end{aligned} \tag{E.12}$$

Note that in the last line of Eq. (E.12) we assume that the initial state y at time $t = 0$ is in thermal equilibrium. As stated earlier, this is the sole assumption made in this derivation. For a time dependent V_{N} (and thus a time dependent Fokker-Planck operator).

Eq. (E.4) asserts that $\int d\{x\}\langle\{x\}| = \langle +|$. Invoking this along with Eq. (E.2), we have

$$G_{\mathsf{classical}}(t) = \langle +|\mathcal{O}_1 \mathcal{T} e^{-\int_0^t H_{FP}(t')dt'} \mathcal{O}_2|G\rangle. \tag{E.13}$$

As is evident from Eq. (E.10), inserting an exponentiation of H_{FP} to the right of the state $\langle +|$ leads to a multiplication by unity. Thus Eq. (E.13) can be rewritten as

$$G_{\mathsf{classical}}(t) = \langle +|\mathcal{T} e^{\int_0^t H_{FP}(t')dt'} \mathcal{O}_1 \mathcal{T} e^{-\int_0^t H_{FP}(t')dt'} \mathcal{O}_2|G\rangle. \tag{E.14}$$

With the aid of Eq. (E.5), we can express this quantity in terms of the quantum Hamiltonian H instead of H_{FP},

$$G_{\mathsf{classical}}(t) = \langle +|e^{-V_{\mathsf{N}}/(2T)} \mathcal{T} e^{\int_0^t H(t')dt'} \mathcal{O}_1 \mathcal{T} e^{-\int_0^t H(t')dt'} e^{V_{\mathsf{N}}/(2T)} \mathcal{O}_2|G\rangle, \tag{E.15}$$

Multiplying and dividing by $\sqrt{Z_N}$,

$$G_{\mathsf{classical}}(t) = \langle +| \frac{e^{-V_{\mathsf{N}}/(2T)}}{\sqrt{Z_N}} \mathcal{T} e^{\int_0^t H(t')dt'} \mathcal{O}_1 \mathcal{T} e^{-\int_0^t H(t')dt'} \mathcal{O}_2 \sqrt{Z_N} e^{V_{\mathsf{N}}/(2T)} |G\rangle. \quad \text{(E.16)}$$

As discussed in Appendix C (in particular, Eq. (C.19)), the ground state of the quantum system is given by $|0\rangle = \sqrt{Z_N} e^{V_{\mathsf{N}}/(2T)} |G\rangle$, and invoking Eqs. (E.2,E.4), we can rewrite Eq. (E.16) as

$$G_{\mathsf{classical}}(t) = \langle 0| \mathcal{T} e^{\int_0^t H(t')dt'} \mathcal{O}_1 \mathcal{T} e^{-\int_0^t H(t')dt'} \mathcal{O}_2 |0\rangle. \quad \text{(E.17)}$$

Note that in this equation, the expectation value is written as in a quantum Dirac form. $|0\rangle$ is the ground state of the quantum system and H is the Hamiltonian of the quantum counterpart. Our results above are general. We will shortly use Eq. (E.17) in order to relate it to correlations in the quantum system.

We next comment on the particular case of a time independent H with a fixed spectrum $\{|n\rangle\}$. It is important to emphasize that unlike our general result of Eq. (E.17) above, such a situation does not encompass a multitude of glassy and other systems which are driven out of equilibrium by time dependent processes and in which the probability distribution is not given by the Boltzmann distribution. In our above derivation, we assumed that the system starts from an equilibrium state and is then acted on by a time dependent Hamiltonian which might (or might not) drive it out of equilibrium. An identical result holds if we start from a non-equilibrium state and

then drive the system at a final time t to an equilibrium state. (In this latter case, in Eq. (E.12), the role of the coordinates $\{x\}$ and $\{y\}$ is inverted: the probability distribution of the final state $P(\{x\})$ will be given by a Boltzmann distribution and, similar to before, $P(\{x\}|\{y\}) = \langle\{x\}|\mathcal{T}e^{-\int_0^t H_{FP}(t')dt'}|\{y\}$. Bayes' theorem asserts as earlier that the joint probability distribution over which the average in Eq. E.12) is performed is given by $P(\{x\},\{y\}) = P(\{x\}|\{y\})P(\{x\})$.

Next, we insert a resolution of the identity, $\sum_n |n\rangle\langle n| = \mathbb{I}$, leading to

$$G_{\mathsf{classical}}(t) = \sum_n \langle 0|\mathcal{O}_1|n\rangle\langle n|\mathcal{O}_2|0\rangle e^{-t(E_n - E_0)}. \tag{E.18}$$

Defining

$$\mathcal{O}_{12}(\omega) = 2\pi \sum_n \langle 0|\mathcal{O}_1|n\rangle\langle n|\mathcal{O}_2|0\rangle \delta(E_n - E_0 - \omega), \tag{E.19}$$

we can express Eq. (E.18) as

$$G_{\mathsf{classical}}(t) = \int_0^\infty \frac{d\omega}{2\pi}\mathcal{O}_{12}(\omega)e^{-\omega t}. \tag{E.20}$$

We recognize $\mathcal{O}_{12}(\omega)$ as the distribution function $W(\omega)$ in Eq. (6.6).

In the quantum arena, it is clear that for a system initially prepared in the ground state $|0\rangle$ and then evolved with some Hamiltonian $H(t)$, the corresponding correlation

function is given by

$$G_{\mathsf{Quantum}} = \langle 0|\mathcal{T}e^{i\int_0^t H(t')dt'}\mathcal{O}_1\mathcal{T}e^{-i\int_0^t H(t')dt'}\mathcal{O}_2|0\rangle. \tag{E.21}$$

By comparing Eq. (E.17) with Eq. (E.21), it is seen that

$$G_{\mathsf{Quantum}}(t) = G_{\mathsf{classical}}(it). \tag{E.22}$$

We next turn to the quantum response function R_{Quantum} that monitors the change in the average value of $\mathcal{O}_1$ as a result of a perturbation $\mathcal{O}_2$. Specifically, we consider the Hamiltonian

$$H_{\mathsf{tot}} = H + H^{'} \tag{E.23}$$

where H' is a small perturbation which can be expressed as $H' = -\lambda\mathcal{O}_2$. We next review standard protocol for computing the lowest order the deviation

$$\delta\langle\mathcal{O}_1(t)\rangle = \langle\mathcal{O}_1(t)\rangle_\lambda - \langle\mathcal{O}_1(t)\rangle_0 \tag{E.24}$$

which we will evaluate within the ground state $|0\rangle$. This is readily computed in the interaction picture where we evolve with the time ordered exponential $T\exp(-iH't)$,

$$\langle\mathcal{O}_1(t)\rangle_\lambda = \langle\left(1 - i\int^t dt'\ \lambda(t)\ \mathcal{O}_2(t')\right)\mathcal{O}_1(t)\left(1 + i\int^t dt'\ \lambda(t)\ \mathcal{O}_2(t')\right)\rangle. \tag{E.25}$$

Collecting terms to lowest order we have

$$\begin{aligned}\delta\langle\mathcal{O}_1(t)\rangle &\approx i\int^t dt'\ \lambda(t')\ \langle[\mathcal{O}_1(t),\mathcal{O}_2(t')]\rangle \\ &= i\int_0^\infty d\tau\ \lambda(t-\tau)\ \langle[\mathcal{O}_1(\tau),\mathcal{O}_2(0)]\rangle \\ &\equiv \int_{-\infty}^\infty d\tau\ \lambda(t-\tau)\ R_Q(\tau) \end{aligned} \tag{E.26}$$

As $\mathcal{O}_1(t) = \mathcal{T}e^{-i\int_0^t H(t')dt'}\mathcal{O}_1\mathcal{T}e^{i\int_0^t H(t')dt'}$, from the last line of Eq. (E.26),

$$R_{\mathsf{Quantum}} = i\Theta(t)\langle 0|\left[\mathcal{T}e^{i\int_0^t H(t')dt'}\mathcal{O}_1\mathcal{T}e^{-i\int_0^t H(t')dt'},\mathcal{O}_2\right]|0\rangle. \tag{E.27}$$

Comparing Eqs. (E.17, E.27), we see that

$$\begin{aligned}R_{\mathsf{Quantum}} &= i\Theta(t)(G_{\mathsf{classical}}(it) - G^*_{\mathsf{classical}}(it)) \\ &= -2\Theta(t)\Im G_{\mathsf{classical}}(it). \end{aligned} \tag{E.28}$$

Our results above are general[1]. We next comment on the particular case of a time independent H with a fixed spectrum $\{|n\rangle\}$. Expanding the expectation value and splitting it into two separate expectation values, and inserting a resolution of the identity $\sum_n |n\rangle\langle n|$,

[1]Eq. E.28 and Eq. 6.8 are generally equivalent (i.e., also for time dependent Hamiltonians) as can be shown by writing the step function and the imaginary part of the correlation function as their Fourier counterparts and using the Kramers-Kronig relations. This is included for pedagogical purposes.

$$R_{\mathsf{Quantum}} = i\Theta(t)\sum_n \Big(\langle 0|e^{iHt}\mathcal{O}_1|n\rangle\langle n|e^{-iHt}\mathcal{O}_2|0\rangle - \langle 0|\mathcal{O}_2 e^{iHt}|n\rangle\langle n|\mathcal{O}_1 e^{-Ht}|0\rangle\Big) \tag{E.29}$$

Allowing H to operate on the states and pulling out the exponentials,

$$R_{\mathsf{Quantum}} = i\Theta(t)\sum_n \langle 0|\mathcal{O}_1|n\rangle\langle n|\mathcal{O}_2|0\rangle \sin(t(E_n - E_0)). \tag{E.30}$$

Using the definition of $\mathcal{O}_{12}(\omega)$ in Eq. (E.19), this is equal to:

$$-2\Theta(t)\int_0^\infty \frac{d\omega}{2\pi}\mathcal{O}_{12}(\omega)\sin(\omega t). \tag{E.31}$$

Taking the imaginary part of the Fourier Transform of this function, one is left with

$$R''_{\mathsf{Quantum}}(\omega) = \frac{1}{2}\mathrm{sgn}(\omega)\mathcal{O}_{12}(|\omega|). \tag{E.32}$$

Using the fluctuation-dissipation theorem, we can relate the quantum correlation function to the imaginary part of the quantum response function by $S_Q(q,\omega) =$

$\frac{1}{2}\mathrm{sgn}(\omega)R''_{\mathsf{Quantum}}(q,\omega) = \frac{1}{2}\mathcal{O}_{12}(|\omega|)$. Thus,

$$R_{\mathsf{Quantum}} = \int_{-\infty}^{\infty} \frac{d\omega}{2\pi} S_Q(q,\omega) e^{-i\omega t}. \tag{E.33}$$

Only the even part survives, and

$$R_{\mathsf{Quantum}} = \int_{0}^{\infty} \frac{d\omega}{2\pi} \mathcal{O}_{12}(\omega)\cos(\omega t). \tag{E.34}$$

This constitutes the derivation of Eq. (6.7) with the distribution function $W(\omega)$ given by $\mathcal{O}_{12}(\omega)$.

Taken together Eqs.(E.20, E.34) lead to Eq. (6.8).

Appendix F

Arbitrary Number of Time-Ordered Operators

A derivation similar to that in Appendix E can be done for a correlation function of an arbitrary number of operators. In the classical case, the correlation function takes the form of

$$G_{cl} = \langle \mathcal{O}_1(t_1)\mathcal{O}_2(t_2)...\mathcal{O}_n(t_n)\rangle, \tag{F.1}$$

where $\mathcal{O}_i$ are arbitrary operators and $t_1 < t_2 < ... < t_n$.

Similar to Appendix E, by Bayes' theorem this correlation function is given by

$$\int d\{x_1\}d\{x_2\}...d\{x_n\}\mathcal{O}_n\langle\{x_n\}|\mathcal{T}e^{-\int_{t_{n-1}}^{t_n}H_{FP}(t')dt'}|\{x_{n-1}\}\rangle$$
$$\mathcal{O}_{n-1}...\langle\{x_2\}|\mathcal{T}e^{-\int_{t_1}^{t_2}H_{FP}(t')dt'}|\{x_1\}\rangle\mathcal{O}_1\frac{e^{-\beta U_N(\{x_1\})}}{Z_N}. \tag{F.2}$$

By similar identity matrix integrations as before, this can be simplified into the form of

$$\langle+|\mathcal{T}e^{-\int_{t_n}^{t_1}H_{FP}(t')dt'}\mathcal{O}_n\mathcal{T}e^{-\int_{t_{n-1}}^{t_n}H_{FP}(t')dt'}\mathcal{O}_{n-1}...\mathcal{T}e^{-\int_{t_1}^{t_2}H_{FP}(t')dt'}\mathcal{O}_1|G\rangle. \tag{F.3}$$

Transforming to the quantum Hamiltonian and quantum ground state yields

$$\langle 0|\mathcal{T}e^{-\int_{t_n}^{t_1}H(t')dt'}\mathcal{O}_n\mathcal{T}e^{-\int_{t_{n-1}}^{t_n}H(t')dt'}\mathcal{O}_{n-1}...\mathcal{T}e^{-\int_{t_1}^{t_2}H(t')dt'}\mathcal{O}_1|0\rangle. \tag{F.4}$$

The results up to this point are completely general. If we were to assume a time independent Hamiltonian, though, the analysis of previous examples can be followed by inserting a series of identity matrices

$$\sum_{n,m,...l}\langle 0|\mathcal{O}_n|n\rangle\langle n|\mathcal{O}_{n-1}|m\rangle...\langle l|\mathcal{O}_1|0\rangle$$
$$\times e^{-(t_1-t_n)E_0}e^{-(t_n-t_{n-1})E_n}...e^{-(t_2-t_1)E_l}. \tag{F.5}$$

Defining a function of the form,

$$\mathcal{O}_{1...n} = \sum_{n,m,...l} \langle 0|\mathcal{O}_n|n\rangle\langle n|\mathcal{O}_{n-1}|m\rangle ...\langle l|\mathcal{O}_1|0\rangle$$
$$(2\pi)^n \delta(E_0 - E_n - \omega_n)\delta(E_n - E_m - \omega_{n-1})...\delta(E_l - E_0 - \omega_1), \tag{F.6}$$

one can write the classical correlation function in the form,

$$G_{cl} = \sum_{n,m,...,l} \int \frac{d\omega_1}{2\pi} \int \frac{d\omega_2}{2\pi} ... \int \frac{d\omega_n}{2\pi} \mathcal{O}_{1...n} e^{\omega_1 t_1} e^{\omega_2 t_2} ... e^{\omega_n t_n}. \tag{F.7}$$

For the quantum correlation function case, one starts with the linear quantum response function will be set by

$$\langle 0|[\mathcal{T} e^{it_n H} \mathcal{O}_n \mathcal{T} e^{-it_n H}, [\mathcal{T} e^{it_{n-1} H} \mathcal{O}_{n-1} \mathcal{T} e^{-it_{n-1} H},$$
$$...[\mathcal{T} e^{it_2 H} \mathcal{O}_2 \mathcal{T} e^{-it_2 H}, \mathcal{T} e^{it_1 H} \mathcal{O}_1 \mathcal{T} e^{-it_1 H}]]]|0\rangle. \tag{F.8}$$

The series of commutators will give the operators in various orders. The process for any given order is the same. We now consider so examining a specific order of operators that will appear,

$$G_{Quantum} = \langle 0|\mathcal{T}e^{it_nH}\mathcal{O}_n\mathcal{T}e^{-it_nH}\mathcal{T}e^{it_{n-1}H}\mathcal{O}_{n-1}\mathcal{T}e^{-it_{n-1}H}...\mathcal{T}e^{it_1H}\mathcal{O}_1\mathcal{T}e^{-it_1H}|0\rangle. \quad \text{(F.9)}$$

The results up to this point are completely general. If we were to assume a time independent Hamiltonian, though, the analysis of previous examples can be followed by inserting complete sets of states leads to

$$\sum_{n,m,...,l} \langle 0|\mathcal{O}_n|n\rangle\langle n|\mathcal{O}_{n-1}|m\rangle...\langle l|\mathcal{O}_1|0\rangle e^{i(t_1-t_n)E_0}e^{i(t_n-t_{n-1})E_n}...e^{i(t_2-t_1)E_l}. \quad \text{(F.10)}$$

Using Eq. (F.6), this can be written as,

$$G_{Quantum} = \sum_{n,m,...,l}\int\frac{d\omega_1}{2\pi}\int\frac{d\omega_2}{2\pi}...\int\frac{d\omega_n}{2\pi}\mathcal{O}_{1...n}e^{i\omega_1t_1}e^{i\omega_2t_2}...e^{i\omega_nt_n}. \quad \text{(F.11)}$$

Combining this with the other orders of operators from the commutator will ultimately give rise to exponentials that will be negative conjugates of the the ones in Equation (F.11) which will effectively change the exponentials to sine functions. The rest of the derivation is the same as Appendix E. Comparing Eqs. (F.7, F.11), we arrive at our result concerning arbitrary order (n) correlation functions for interacting many body systems. In order to go from the classical to the quantum system, we replace the times $\{t_a\}_{a=1}^n$ by $\{it_a\}_{a=1}^n$ to go from the classical to the many body

quantum problem.